

The Brewer-Dobson circulation : interannual variability and climate change

Citation for published version (APA):

Haklander, A. J. (2008). *The Brewer-Dobson circulation : interannual variability and climate change*. [Phd Thesis 1 (Research TU/e / Graduation TU/e), Applied Physics and Science Education]. Technische Universiteit Eindhoven. <https://doi.org/10.6100/IR637579>

DOI:

[10.6100/IR637579](https://doi.org/10.6100/IR637579)

Document status and date:

Published: 01/01/2008

Document Version:

Publisher's PDF, also known as Version of Record (includes final page, issue and volume numbers)

Please check the document version of this publication:

- A submitted manuscript is the version of the article upon submission and before peer-review. There can be important differences between the submitted version and the official published version of record. People interested in the research are advised to contact the author for the final version of the publication, or visit the DOI to the publisher's website.
- The final author version and the galley proof are versions of the publication after peer review.
- The final published version features the final layout of the paper including the volume, issue and page numbers.

[Link to publication](#)

General rights

Copyright and moral rights for the publications made accessible in the public portal are retained by the authors and/or other copyright owners and it is a condition of accessing publications that users recognise and abide by the legal requirements associated with these rights.

- Users may download and print one copy of any publication from the public portal for the purpose of private study or research.
- You may not further distribute the material or use it for any profit-making activity or commercial gain
- You may freely distribute the URL identifying the publication in the public portal.

If the publication is distributed under the terms of Article 25fa of the Dutch Copyright Act, indicated by the "Taverne" license above, please follow below link for the End User Agreement:

www.tue.nl/taverne

Take down policy

If you believe that this document breaches copyright please contact us at:

openaccess@tue.nl

providing details and we will investigate your claim.

The Brewer-Dobson circulation: interannual variability and climate change

PROEFSCHRIFT

ter verkrijging van de graad van doctor aan de
Technische Universiteit Eindhoven, op gezag van de
Rector Magnificus, prof.dr.ir. C.J. van Duijn, voor een
commissie aangewezen door het College voor
Promoties in het openbaar te verdedigen
op dinsdag 23 september 2008 om 16.00 uur

door

Alwin Johannes Haklander

geboren te Oldebroek

Dit proefschrift is goedgekeurd door de promotoren:

prof.dr. H.M. Kelder

en

prof.dr.ir. G.J.F. van Heijst

Copromotor:

dr. P.C. Siegmund

Druk: Universiteitsdrukkerij Technische Universiteit Eindhoven

Haklander, A.J.

The Brewer-Dobson circulation: interannual variability and climate change /
by Alwin Haklander. — Eindhoven: Technische Universiteit Eindhoven,
2008. Proefschrift.

ISBN 978-90-386-1384-0

NUR 912

A catalogue record is available from the Eindhoven University of
Technology Library.

De wind waait naar het zuiden,
dan draait hij naar het noorden.

Hij draait en waait en draait,
en al draaiend waait de wind weer terug.

Prediker 1:6

This PhD study contains the following peer-reviewed publications, in slightly revised form.

Haklander, A. J., P. C. Siegmund, and H. M. Kelder: Analysis of the frequency-dependent response to wave forcing in the extratropics, *Atmos. Chem. Phys.*, 6, 4477–4481, 2006.

Haklander, A. J., P. C. Siegmund, and H. M. Kelder: Interannual variability of the stratospheric wave driving during northern winter, *Atmos. Chem. Phys.*, 7, 2575–2584, 2007.

Haklander, A. J., P. C. Siegmund, M. Sigmond, and H. M. Kelder: How does the northern-winter wave driving of the Brewer-Dobson circulation increase in an enhanced-CO₂ climate simulation?, *Geophys. Res. Lett.*, 35, L07702, doi:10.1029/2007GL033054, 2008.

Cover:

Color composition of Meteosat Spinning Enhanced Visible and Infrared Imager (SEVIRI) water vapor channels 5 (5.35 - 7.15 μm) and 6 (6.85 - 7.85 μm), showing wave-like patterns in the upper troposphere on various length scales on 15 January 2006 at 1200 UTC. Credits grayscale WV imagery: EUMETSAT, NERC Satellite Receiving Station, University of Dundee, UK; <http://www.sat.dundee.ac.uk>.

Contents

SUMMARY	1
SAMENVATTING	3
1 INTRODUCTION.....	9
1.1 The BDC, what it is and what it does.....	9
1.2 Basic physical principles	13
1.2.1 Newton’s second law in rotational form	13
1.2.2 First law of thermodynamics	15
1.2.3 Eulerian and Transformed Eulerian mean	16
1.2.4 Downward control principle	20
1.3 Wave driving of the BDC.....	22
1.3.1 Rossby waves.....	22
1.3.2 Rossby-wave propagation in the meridional plane.....	25
1.3.3 Wave dissipation and westward angular momentum deposition	26
1.4 Overview of this thesis.....	28
2 ANALYSIS OF THE FREQUENCY-DEPENDENT RESPONSE TO WAVE FORCING IN THE EXTRATROPICS	33
2.1 Introduction	34
2.2 Frequency-dependent TEM model	35
2.3 Data and method.....	36
2.4 Results.....	38
2.5 Discussion and conclusions	42
3 INTERANNUAL VARIABILITY OF THE STRATOSPHERIC WAVE DRIVING DURING NORTHERN WINTER.....	45
3.1 Introduction	46
3.2 Data and method.....	48
3.2.1 Data	48
3.2.2 Linear regression analysis	49
3.2.3 Decompositions of the heat flux	49
3.3 Results.....	52
3.3.1 Timeseries of H_{100}	52

3.3.2 Wave contributions to interannual variability of H_{100}	53
3.3.3 Vertical coupling.....	54
3.3.4 Correlation patterns in the meridional plane.....	58
3.3.5 An alternative analysis of the interannual variability of H_{100}	62
3.4 Summary and discussion.....	63
4 HOW DOES THE NORTHERN-WINTER WAVE DRIVING OF THE BREWER-DOBSON CIRCULATION INCREASE IN AN ENHANCED-CO₂ CLIMATE SIMULATION?	67
4.1 Introduction	68
4.2 Climate simulations and methods	69
4.3 Results.....	71
4.4 Conclusions	77
5 DISCUSSION AND OUTLOOK.....	79
5.1 Discussion	79
5.2 Outlook.....	82
REFERENCES.....	85
NAWOORD.....	95
CURRICULUM VITAE.....	97

The Brewer-Dobson circulation: interannual variability and climate change

Summary

A quasi-geostrophic theoretical model for the frequency-dependent response of the zonal-mean flow to planetary-wave forcing at Northern Hemisphere (NH) midlatitudes was applied to 4D-Var ECMWF data for six extended winter seasons. Linear regression analyses yielded height-dependent estimates for the thermal damping time, and for a scaling parameter which includes the aspect ratio of the meridional to the vertical length scale of the response. The estimated thermal damping time is ~2 days in the troposphere, 7-10 days in the stratosphere, and 2-4 days in the lower mesosphere. The results indicated that the theoretical model is applicable to midlatitude wintertime conditions.

In the low-frequency limit, the response to the wave driving is given by the Brewer-Dobson circulation (BDC), which has been the focus of our further research. ERA-40 reanalysis data for the period 1979-2002 were used to examine several factors that significantly affect the interannual variability of the wave driving. The individual zonal wave-1 and wave-2 contributions to the wave driving at 100 hPa exhibit a significant coupling with the troposphere, predominantly their stationary components. The stationary wave-1 contribution to the total wave driving significantly depends on the latitude of the stationary wave-1 source in the troposphere. The results suggest that this dependence is associated with the varying ability of stationary wave-1 activity to enter the tropospheric waveguide at mid-latitudes. The wave driving anomalies were separated into three parts: one part due to anomalies in the zonal correlation coefficient between the eddy temperature and eddy meridional wind, another part due to anomalies in the zonal eddy temperature amplitude, and a third part due to anomalies in the zonal eddy meridional wind amplitude. It was found that year-to-year variability in the zonal correlation coefficient between the eddy temperature and the eddy meridional wind is the dominant factor in explaining the year-to-year variability of the poleward eddy heat flux.

Using the ECHAM middle-atmosphere climate model, it was found that the midwinter NH wave driving exhibits a highly significant increase (12%) if CO₂ concentrations are doubled. The magnitude and large statistical significance of the increase due to stationary waves only was found to be comparable to that of the total increase. However, dividing the response into the different wavenumber components yielded a more subtle picture, with a decrease in transient wave-1 to less than 50% of the 1×CO₂ value and an increase in transient wave-5 to almost the double value. Although transient wave-5 is usually thought not to contribute substantially to the wave driving of the stratosphere, its increase constitutes about 1/6 of the total increase of the wave driving in a 2×CO₂ climate.

Samenvatting

Inleiding

Ons dagelijkse weer speelt zich af in de troposfeer, de onderste laag van de atmosfeer. Wolken en neerslag komen boven deze goed gemengde laag vrijwel niet voor. Boven de polen is de troposfeer ongeveer 7 km dik, maar boven de evenaar ruim tweemaal zo dik. De luchtlaag direct boven de troposfeer, de stratosfeer, is zeer droog en daardoor nagenoeg wolkenvrij. Deze hogere luchtlaag is de afgelopen decennia wat dichterbij de mensen gekomen. Niet alleen omdat steeds meer mensen de onderste lagen van de stratosfeer per vliegtuig doorkruisen, maar ook vanwege de ozonlaagproblematiek die vanaf de jaren '80 van de vorige eeuw uitgebreid door de media onder de aandacht werd gebracht. Stratosferisch ozon is van groot belang voor het leven op aarde, doordat ozonmoleculen schadelijke, hoog-energetische UV straling van de zon absorberen en daardoor tegenhouden.

Sinds begin jaren '80 vormt zich in de stratosfeer, waarin zich de ozonlaag bevindt, jaarlijks een ozongat boven Antarctica. Dit gat ontstaat meestal in september en is een gevolg van de katalytische chemische afbraak van ozon, hoofdzakelijk onder invloed van chloorfluorkoolstoffen (CFK's). Deze CFK's zijn vanaf de jaren '50 van de vorige eeuw door de mens in de atmosfeer gebracht en de uitstoot ervan is sinds het Montreal Protocol, waarvan vorig jaar het 20-jarige jubileum werd gevierd, drastisch beperkt. De jaarlijkse, katalytische afbraak van ozon boven de Zuidpool zal echter nog vele decennia doorgaan, aangezien de ozonafbrekende stoffen niet meteen uit de stratosfeer verwijderd zijn. CFK's worden bovenin de stratosfeer (grotendeels boven de 25 km hoogte) afgebroken door dezelfde hoog-energetische zonnestraling als die waartegen de ozonlaag ons beschermt. Het is echter zo dat meer dan 90% van de atmosferische massa zich beneden dit niveau bevindt. De totale hoeveelheid CFK's die in de atmosfeer is beland zal dus maar mondjesmaat op grote hoogte worden afgebroken. Het afbraakproces wordt enigszins gefaciliteerd door een circulatie in de stratosfeer, die de CFK's langzaam maar zeker rondpompt: in de tropen omhoog van de troposfeer naar

de stratosfeer, in de extratropen poolwaarts en op hogere breedten weer terug naar de troposfeer. Deze zogeheten Brewer-Dobson circulatie (BDC) zorgde er ook voor dat de CFK's al vrij snel na de productie en uitstoot ervan in de stratosfeer konden belanden. Doordat ozon zich vooral bij intens ultraviolet zonlicht bovenin de tropische stratosfeer vormt, voorziet de BDC de extratropen (waar ozon zich langer kan handhaven) op efficiënte wijze van ozon. Bovendien pompt de circulatie ozonarme lucht omhoog waarin weer nieuwe ozon gevormd wordt. Hierdoor wordt de BDC ook wel gezien als een fotochemische motor.

De BDC vormt het hoofdonderwerp van dit proefschrift. Ze valt in feite te beschrijven als een 'golfgedreven' circulatie. Het principe is, dat de atmosferische golven die de BDC aandrijven een westwaartse kracht uitoefenen zodra ze op grote hoogte breken. Vanwege de snelle draaiing van de aarde om zijn as, leidt deze kracht tot een zeer langzame, poolwaartse luchtbeweging in de stratosfeer. Die lucht moet ergens heen en ergens vandaan komen, waardoor er neerwaartse bewegingen ontstaan in de extratropen en opwaartse bewegingen in de tropen.

Net als in de oceaan, komen er in de atmosfeer allerlei soorten golven voor, op vele ruimtelijke schalen. De BDC wordt voornamelijk aangedreven door de golven met de grootste ruimtelijke schaal: Rossby- (of planetaire) golven genoemd. Deze golven komen in allerlei meteorologische velden tot uitdrukking, zoals in de temperatuur, de wind (slingeringen in de stroming) en de luchtdruk. De ruimtelijke schaal van de golven wordt uitgedrukt in een golfgetal: het zonale golfgetal beschrijft het aantal schommelingen op een breedtecirkel. Een Rossbygolf met zonaal golfgetal 1 zou je bijvoorbeeld in het temperatuurveld kunnen herkennen als een warm gebied aan de ene zijde van de aardbol en een koud gebied op dezelfde breedtegraad aan de andere zijde. Bij zonaal golfgetal 2 wisselen twee warme en twee koude gebieden elkaar af op een breedtecirkel, enzovoort. Op deze manier zijn alle meteorologische velden te beschouwen als het gemiddelde over de gehele breedtecirkel (zoals de achtergrondstroming vaak wordt gedefinieerd) plus de verschillende golfcomponenten die daarop gesuperponeerd zijn.

Een belangrijke eigenschap van Rossbygolven is, dat ze alleen westwaarts kunnen bewegen t.o.v. de achtergrondstroming die ze meevoert. Rossbygolven die door een

stationaire bron worden opgewekt, zoals door land-zee contrasten en topografie, zullen zelf ook stationair zijn. Voor deze golven zijn westenwinden dus een voorwaarde: alleen bij een westelijke achtergrondstroming kunnen ze immers westwaarts bewegen t.o.v. de heersende wind en tóch stationair zijn t.o.v. het aardoppervlak. Doordat de winden in het zomerhalfjaar overwegend oostelijk zijn in de stratosfeer, kunnen Rossbygolven die in de troposfeer worden opgewekt in dat jaargetijde nauwelijks tot in de stratosfeer doordringen. Het gevolg is dat de BDC iedere lente stilvalt en in de herfst weer opstart. Een andere eigenschap van Rossbygolven is, dat hun relatieve westwaartse beweging sneller verloopt naarmate hun golfgetal kleiner is. Wat de stationaire Rossbygolven betreft kunnen hierdoor alleen de langste golven (bijv. zonaal golfgetal 1 en 2) bij sterke westenwinden bestaan, doordat alleen deze golven nog snel genoeg westwaarts bewegen t.o.v. de heersende wind om nog stationair te zijn. In de extratropen overheersen sterke westenwinden nabij de tropopauze, waar de troposfeer overgaat in de stratosfeer. Deze krachtige westenwinden werken dus als een filter voor Rossbygolven vanuit de troposfeer, waarbij alleen de langere Rossbygolven worden doorgelaten en de BDC kunnen aandrijven.

Dit proefschrift

In dit proefschrift komen meerdere onderzoeksvragen m.b.t. de BDC aan de orde, specifiek voor het Noordelijk Halfrond, waar de aandrijving door Rossbygolven sterker is dan op het Zuidelijk Halfrond. Samengevat is onderzocht hoe de aandrijving van de BDC afhangt van de tijdschaal van de golfforcering, door welk type golven de jaar-op-jaar variaties worden bepaald, en hoe we kunnen begrijpen waardoor de aandrijving van de BDC kan toenemen door de toenemende broeikasgasconcentraties. Dit laatste kan namelijk steeds duidelijker uit experimenten met klimaatmodellen geconcludeerd worden.

In hoofdstuk 2 wordt gekeken naar hoe de aandrijving van de BDC afhangt van de tijdschaal waarop deze aandrijving plaatsvindt. Volgens een eenvoudig theoretisch model van de wisselwerking tussen golven en de achtergrondstroming, hangen de details hiervan af van twee andere zaken. Ten eerste hangen ze af van de tijdschaal waarop

schommelingen in de temperatuur worden gedempt, met name door langgolvlige warmtestraling. Hoe korter deze tijdschaal is, hoe meer de temperatuurschommelingen worden gedempt en hoe efficiënter de BDC wordt aangedreven op wat kortere tijdschalen. Ten tweede hangen de details van de respons van de BDC op de golfforcering af van de verhouding tussen de horizontale (noord-zuid) en verticale lengteschalen van deze respons. Deze schaalverhouding wordt de aspect ratio genoemd. De hoogteafhankelijkheid van zowel de thermische dempingstijdschaal als de aspect ratio van de respons is geschat door het model te vergelijken met de waarnemingen. Als waarnemingen zijn de meteorologische velden van de temperatuur en de wind gedurende zes verlengde winterseizoenen gebruikt, zoals geassimileerd door het ECMWF weermodel. Golven met een ruimtelijke schaal van enkele tientallen kilometers en minder zijn hierbij niet meegenomen, vanwege de beperkte resolutie van het model. Toepassing van het vereenvoudigde model op de waarnemingen leidt tot een schatting van de thermische dempingstijdschalen die goed overeenkomt met de waarden uit de literatuur.

In hoofdstuk 3 worden jaar-op-jaar variaties in de aandrijving van de BDC onder de loep genomen. Hierbij is gebruik gemaakt van geobserveerde meteorologische velden tijdens de winters van 1979 t/m 2002 volgens de gegevens van het ERA-40 (ECMWF Reanalysis) project. Een belangrijke meteorologische grootte die de sterkte van de golfaandrijving van de BDC beschrijft, is het poolwaartse warmtetransport door golven in de lagere stratosfeer (op ongeveer 16 km hoogte) op gematigde breedten. De gevoeligheid van deze poolwaartse warmteflux voor verschillende typen golven is onderzocht, door hem te ontleden in de bijdragen van de verschillende zonale golfgetallen. Ook werden de stationaire golven hierbij onderscheiden van de lopende golven. Uit deze analyse bleek dat de ultralange golven, waarvan er maar 1 of 2 op een breedtecirkel passen, de jaar-op-jaar variabiliteit van de golfaandrijving voor ongeveer 85% bepalen, waarbij stationaire golven de variabiliteit domineren. Door de warmteflux onderin de stratosfeer te vergelijken met die op andere niveaus, is bovendien onderzocht in hoeverre de totale golfaandrijving onderin de stratosfeer afhangt van de totale golfactiviteit in de troposfeer. Het filtereffect vanwege de sterke westenwinden bovenin de troposfeer blijkt dan erg belangrijk, aangezien jaar-op-jaar variaties in de totale warmteflux onderin de stratosfeer al geen significante koppeling vertonen met de totale

warmteflux bovenin de troposfeer. Deze koppeling wordt alleen gevonden voor golfgetal 1 en 2, waarbij het ook nog eens alleen om de stationaire golven gaat. Voor stationaire golven die een breedtecirkel omspannen blijkt het van belang op welke breedten deze golven zich in de troposfeer bevinden. De stationaire golven met golfgetal 1 nabij 50°N blijken hierbij aanzienlijk beter in staat om de onderste stratosfeer te bereiken dan die nabij de 30°N.

Voor de resultaten die in hoofdstuk 4 aan bod komen is het MA-ECHAM4 klimaatmodel gebruikt. Er zijn twee experimenten uitgevoerd: een controle experiment waarbij de CO₂ concentraties constant op het niveau van 1990 werden gehouden en een 2×CO₂ experiment met de verdubbelde concentraties. De poolwaartse warmteflux onderin de stratosfeer, zoals eerder besproken een belangrijke maat voor de golfaandrijving van de BDC, neemt met 12% toe ten gevolge van de verdubbeling van CO₂, hoofdzakelijk vanwege de toenemende activiteit van stationaire golven. De aanzienlijke afname van de warmteflux in de troposfeer, die samenhangt met lopende (niet-stationaire) golven, blijkt van ondergeschikt belang. Vooral stationaire golven met golfgetal 1 blijken de toename te bepalen; ook in de troposfeer neemt de bijdrage aan de warmteflux door deze golven toe. De toename van de poolwaartse warmteflux vanwege de CO₂ verdubbeling hangt samen met een toename in de temperatuurverschillen tussen noord en zuid op ongeveer 16 km hoogte. Dit contrast neemt toe doordat de troposfeer opwarmt en de stratosfeer afkoelt ten gevolge van het versterkte broeikas-effect. Het 16-km niveau bevindt zich in de tropen nog in de opwarmende troposfeer, maar in de extratropen in de afkoelende stratosfeer. Onze resultaten tonen aan dat het scherpere noord-zuid temperatuurcontrast in een 2×CO₂ klimaatsimulatie leidt tot grotere temperatuurverschillen langs een breedtecirkel, samenhangend met variaties in noord-zuid luchtbewegingen. De toename in de temperatuurverschillen langs een breedtegraad is zelfs eveneens ongeveer 12%. Aangezien de poolwaartse warmteflux evenredig is met de temperatuurvariaties langs een breedtecirkel, bieden onze resultaten een plausibele verklaring voor de toename van de golfaandrijving van de BDC door een verdubbeling van de CO₂ concentraties.

1

Introduction

The subjects considered in this thesis are related to the so-called Brewer-Dobson circulation (BDC). This introduction first describes in section 1.1 what the BDC is, and how it affects the temperature and chemical composition of the atmosphere. Second, in section 1.2 the main characteristics of the BDC are explained from basic physical principles, such as Newton's second law and the first law of thermodynamics. Third, the mechanism that drives the BDC is described in more detail in section 1.3. At the end of this introduction, section 1.4 summarizes the primary questions addressed in this thesis.

1.1 The BDC, what it is and what it does

The BDC is a slow, hemispheric-scale meridional overturning circulation in the stratosphere which is confined to the winter season, with air moving poleward and downward in the extratropics, and upward in the tropics. Figure 1.1 shows the orientation of the BDC during northern winter (for southern winter, the figure could be mirrored by approximation, with the stratospheric transport being directed from the equator to the South Pole). In the Northern Hemisphere, which is the focus of this thesis, the BDC is stronger than in the Southern Hemisphere.

The basic physical principle behind the BDC will be discussed in section 1.2, but for now it is mentioned that the 'engine' behind the circulation is the forcing of poleward flow, mainly in the extratropical stratosphere. With poleward flow in the extratropical stratosphere, the large-scale vertical motions in the BDC are just a consequence of mass conservation. These vertical motions have important consequences for the meridional temperature distribution in the stratosphere. In fact, the tropical tropopause is the coldest

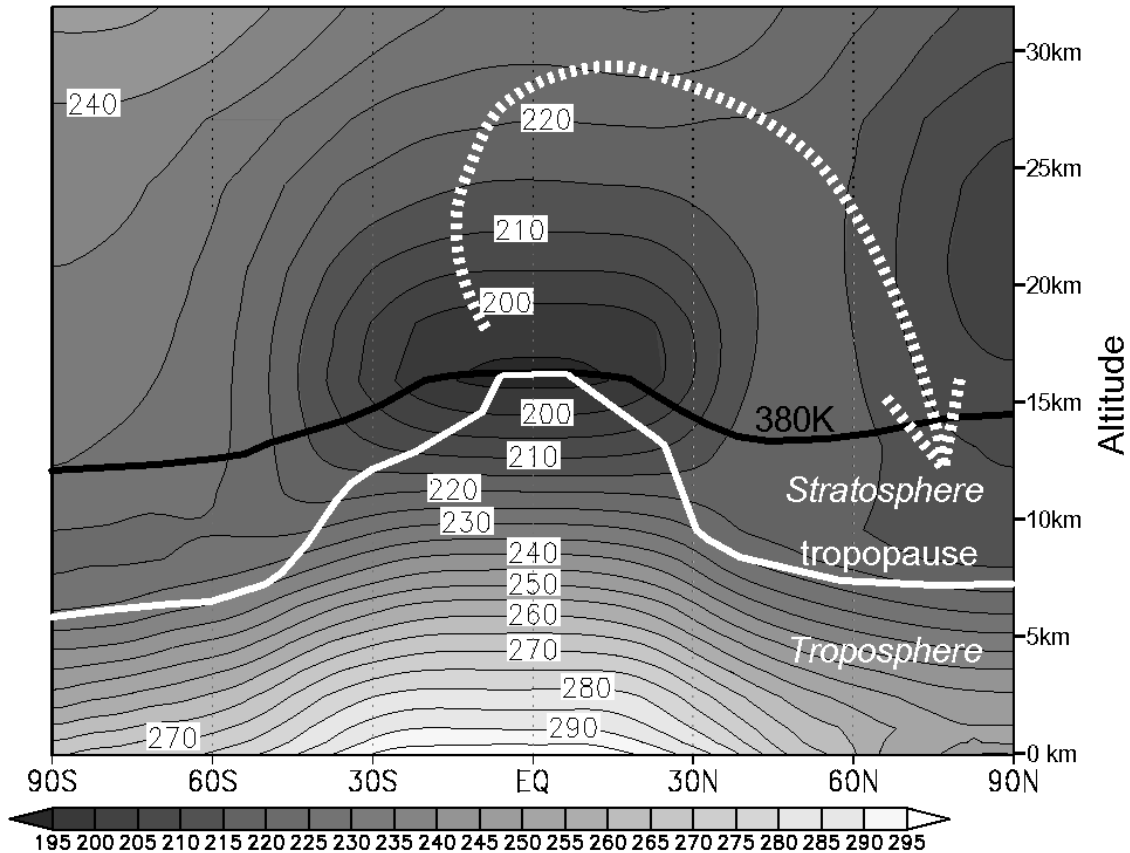


Figure 1.1: Meridional cross section of the longterm (1968-1996) January-February average of the zonal-mean temperature [K], using NCEP/NCAR Reanalysis data. The heavy black line shows the height of the 380K potential temperature surface; the heavy white line roughly denotes the height of the tropopause level (drawn after Holton et al. 1995). The dotted, white arrow roughly denotes the orientation of the BDC during northern winter.

region in the troposphere and stratosphere (see Figure 1.1). This is because the upwelling air in the tropics cools adiabatically due to expansion, which pulls the tropical lower-stratospheric temperatures well below the local radiative equilibrium temperature. The observed zonal-mean temperature pattern led Brewer (1949) to the conclusion that extratropical stratospheric air must have passed through the tropical tropopause layer (TTL), in order to account for the observed low water vapor mixing ratios in the extratropical stratosphere. For only in the TTL, the atmospheric temperatures are sufficiently low to cause the observed dehydration through the process of ‘freeze drying’. As was mentioned before and will be explained later, the BDC is strongest during northern winter. Therefore, the strength of the upwelling in the tropics, and thus the

tropical ‘cold-point’ temperature, exhibits an annual cycle, with the strongest upwelling during northern winter. Through the freeze-drying process, this translates to an annual cycle in lower-stratospheric water vapor mixing ratios. As the air is slowly pumped further upward in the lower stratosphere at a rate of about 10 km/yr, the imprint of the annual cycle in tropical upwelling on the water-vapor mixing ratios remains visible after more than a year. Mote et al. (1996) coined this signal the ‘tropical tape recorder’, with the upwelling air being analogous to an upward moving magnetic tape.

In the polar region, the downwelling air is compressed and adiabatically heated, bringing temperatures several tens of degrees above the local radiative equilibrium temperature. Now, radiative heating (and cooling) always acts to damp any temperature departure from radiative equilibrium. As a consequence, the tropical upwelling air is diabatically heated, and the extratropical downwelling air is diabatically cooled. This chain of events obviously does not portray the BDC as a diabatically forced circulation such as the tropospheric Hadley cell in the (sub)tropics. It is important to note that the diabatic heating and cooling in the BDC are slaved to the adiabatic cooling and heating due to the upwelling and downwelling, which in turn are a consequence of forced poleward flow. Although the term ‘diabatic circulation’ is sometimes still found as a synonym for the BDC in the literature, it does not do justice to the cause and the effect of the BDC.

The BDC is not only dynamically important, but it also affects the chemistry of the atmosphere, due to the meridional and vertical transport of chemical species. The tropical upper stratosphere is the main source region for stratospheric ozone, due to the abundance of highly-energetic photons needed for the photolysis of oxygen. The ozone absorbs most of the incoming solar ultraviolet (UV) radiation, which yields the radiative heating that causes a highly stable stratification in the stratosphere. The absorption of solar UV radiation is very important for the biosphere, for which the highly-energetic photons from the sun are damaging. The ozone-rich air is transported by the BDC from its primary source region in the tropics to the extratropics (e.g., Nikulin and Karpechko 2005). The BDC leads to the net chemical production of ozone in the winter hemisphere, because the ozone becomes longer lived at higher latitudes, with new ozone being produced photochemically in the upwelling air in the tropics. The BDC thus provides a

photochemical engine, increasing the overall ozone abundance during the winter season (Fusco and Salby 1999).

Another important role of the BDC is, that it speeds up the removal of ozone-depleting substances (ODSs), such as the man-made chlorofluorocarbons (CFCs) from the atmosphere. The photochemical destruction of ODSs mainly takes place in the upper stratosphere, which contains less than 10% of the total atmospheric mass. Since the mean stratospheric residence time of air is ~ 5 years (Andrews et al. 2001), it takes more than ~ 50 years to process the ODSs that are present in the troposphere. The rate at which the BDC ‘pumps’ tropospheric air into the stratosphere is therefore important, since it mainly determines the timescale at which the ODSs are processed and removed (Holton 1995).

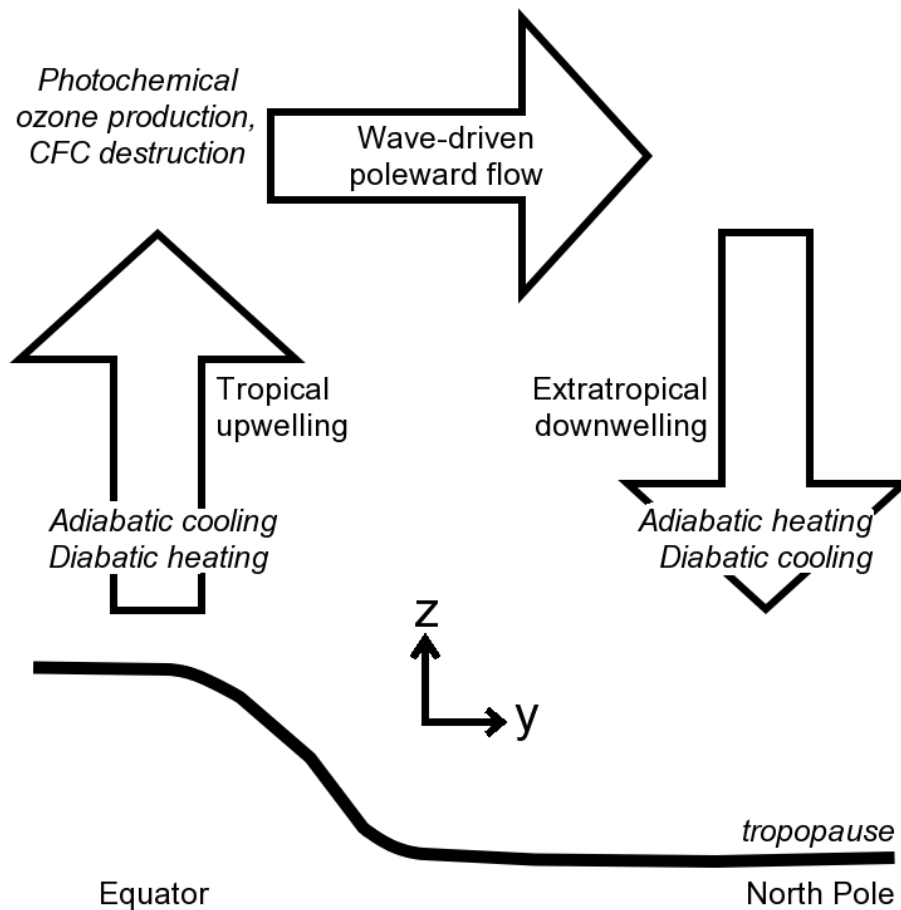


Figure 1.2: Schematic picture of the Northern Hemisphere cell of the Brewer-Dobson circulation in the stratosphere during northern winter.

1.2 Basic physical principles

1.2.1 Newton's second law in rotational form

The basic dynamical principle behind the BDC is that, averaged over time, a westward force causes poleward flow in the stratosphere (in both hemispheres). The source of this westward force will be discussed in section 1.3. To understand how such a time-averaged westward force yields poleward flow, we first use Newton's second law for a unit mass,

$$\hat{\mathbf{F}} = \frac{d\mathbf{v}}{dt}. \quad (1.1)$$

Here, $\hat{\mathbf{F}}$ is the net force per unit mass, \mathbf{v} is the momentum per unit mass, and d/dt is the material time derivative. Equation (1.1) simply states that acceleration equals total force applied per unit mass. If the net force is zero, then momentum is conserved.

This law can be expanded into its rotational form. For a unit mass located a vector distance \mathbf{r} from a given origin,

$$\mathbf{N} = \frac{d\mathbf{L}}{dt}, \quad (1.2)$$

where $\mathbf{N} \equiv \mathbf{r} \times \hat{\mathbf{F}}$ is the torque per unit mass, and $\mathbf{L} \equiv \mathbf{r} \times \mathbf{v}$ is the angular momentum per unit mass. Now, zonal air motion is the sum of the eastward wind component u relative to the surface, and the eastward tangential velocity around the Earth's axis, $\Omega(a+z)\cos\phi$, where a is the Earth's mean radius (~ 6371 km), z is geometric height, ϕ is latitude, and Ω is the Earth's angular velocity ($\sim 7.292 \times 10^{-5}$ rad s^{-1}). The tangential velocity due to the Earth's rotation increases from zero at the poles to ~ 465 m s^{-1} at the equator. For strictly zonal motion, the magnitude of \mathbf{L} equals

$$M \equiv ((a+z)\cos\phi)(u + \Omega(a+z)\cos\phi). \quad (1.3)$$

The quantity M is often referred to as the absolute angular momentum per unit mass, which can be regarded as the sum of the relative angular momentum $M_r \equiv ((a+z)\cos\phi)u$, and the planetary angular momentum $M_\Omega \equiv ((a+z)\cos\phi)^2\Omega$, see e.g. Peixoto and Oort (1992). The torque due to the zonal force \hat{F}_λ is $((a+z)\cos\phi)\hat{F}_\lambda$. Therefore, it follows from Equation (1.2) that

$$((a+z)\cos\phi)\hat{F}_\lambda = \frac{dM}{dt}. \quad (1.4)$$

By noting that the northward (meridional) wind component $v = (a+z)d\phi/dt$, and the upward (vertical) wind component $w = dz/dt$, it follows directly from Equations (1.3) and (1.4) that

$$\hat{F}_\lambda = \frac{du}{dt} + \left(2\Omega + \frac{u}{(a+z)\cos\phi} \right) (-v\sin\phi + w\cos\phi). \quad (1.5)$$

The terms proportional to Ω describe the Coriolis effect, which is the zonal deflection of meridional (and vertical) motions due to the Earth's rotation. The last bracketed term on the r.h.s. of Equation (1.5) is just the time rate of change in the distance from the Earth's rotation axis. The often neglected terms that are proportional to $u((a+z)\cos\phi)^{-1}$ are due to the Earth's curvature, and would also appear in a non-rotating spherical coordinate system.

Generally, \hat{F}_λ is dominated by the zonal pressure gradient force. Large-scale motions, for which the zonal wind acceleration plays a relatively small role, tend to show an approximate balance between this pressure gradient force and the $-2\Omega v\sin\phi$ term, which is called geostrophic balance. The geostrophic wind is defined as the velocity that is required for this balance.

As mentioned before, the basic principle behind the BDC is a westward zonal force, causing a decrease in M (Equation (1.4)). With Ω being very close to constant, Equation (1.3) shows that M can decrease by a reduction of u , or by a reduction of the

distance from the Earth's rotation axis $(a + z)\cos\phi$. Now, the BDC is a zonally averaged meridional circulation on a seasonal or longer timescale. For these long timescales, the net westward acceleration must become very small. Therefore, if a westward torque is systematically exerted on a relatively long timescale, this will be balanced by motion towards the earth's rotation axis, i.e., poleward (or downward) motion.

1.2.2 First law of thermodynamics

We have previously discussed that a systematic westward force drives the poleward branch of the BDC. Due to mass conservation, the air that moves poleward pushes the air it replaces downward, as it is replaced itself by upwelling air in the tropics. In the stratosphere, the upwelling and downwelling in the BDC is suppressed by a very stable thermal stratification. In general, the atmosphere is in hydrostatic balance, which means that the air pressure at a given location equals the weight of the atmospheric column per unit area above that location. The resulting upward pressure-gradient force is in equilibrium with the downward gravitational force.

Due to the downward pressure gradient, an ascending air parcel will thus 'feel' a decrease in environmental pressure, which causes it to expand and do work. Without diabatic heat sources, such as radiative heating, the energy that is required for the parcel's expansion is extracted solely from its internal energy reservoir, which is proportional to its absolute temperature T . This adiabatic cooling due to expansion occurs at a rate of $g/c_p \approx 9.8 \times 10^{-3} \text{ K m}^{-1}$ ascent, where $g \approx 9.81 \text{ J kg}^{-1} \text{ m}^{-1}$ is the increase of gravitational potential energy with height per unit mass, and $c_p \approx 1004 \text{ J K}^{-1} \text{ kg}^{-1}$ is the specific heat of dry air per unit mass at constant pressure. The opposite effect occurs during adiabatic descent, which causes heating (at the same rate) due to compression of the air parcel. These adiabatic temperature effects are incorporated in the definition of the potential temperature

$$\theta \equiv T(p_s / p)^{R/c_p} \quad (1.6),$$

where $R \approx 287 \text{ J K}^{-1} \text{ kg}^{-1}$ is the gas constant for dry air, p_s is a reference pressure (usually taken to be 1000 hPa) and p is pressure. For adiabatic motion, θ is a conserved quantity. This definition allows for a very straightforward description of the thermodynamic energy equation,

$$\frac{d\theta}{dt} = \left(\frac{p_s}{p} \right)^{R/c_p} \frac{J}{c_p}, \quad (1.7)$$

where J is the diabatic heating rate per unit mass. The potential temperature can thus only increase/decrease due to diabatic heating/cooling.

If an air parcel with potential temperature θ_p is surrounded by air with potential temperature θ , the upward buoyancy force on the air parcel per unit mass can be shown to be equal to $g(\theta_p - \theta)/\theta$. Therefore, the more θ increases with height, the larger the restoring buoyancy force due to the static stability of the air, and the more strongly vertical motions will be suppressed. Since θ generally increases monotonically with height in the atmosphere, it can be used as an independent vertical coordinate. Adiabatic motion then becomes two-dimensional, with air remaining on its original isentropic θ -surface. ‘Vertical’ motions in an isentropic coordinate system are always associated with diabatic heating or cooling. We will see in the next section that Equation (1.7) has important implications for the interpretation of zonal-mean descriptions of the flow.

1.2.3 Eulerian and Transformed Eulerian mean

In the previous sections, the mathematical description has been Lagrangian, i.e., confined to individual air parcels. In this section, the BDC will be described as a mass-conserving, quasi-Lagrangian or ‘residual’ zonal-mean circulation. This is a good approximation of the zonal-mean mass flow, but it is generally not the same as the true Lagrangian-mean flow, which is generally divergent due to flow oscillations that change in time (e.g., Andrews 1987).

As will be discussed in the following sections, it is the interaction between large-scale waves and the background flow that provides the westward force driving the

poleward mass flow in the upper branch of the BDC. It makes sense to describe the background flow as a two-dimensional, zonally-averaged field. A zonal-mean description is a natural one, because neither the planetary angular momentum M_Ω (see section 1.2.1) nor the daily solar influx at the top of the atmosphere depends on longitude. Much of the variability in the atmosphere is thus captured by the zonal-mean fields. To describe the wave-like zonal asymmetries of any atmospheric field variable, such as temperature, it is common to describe the total field as the superposition of the zonal-mean field and the ‘eddy’ field, which just describes the local departure from the zonally-averaged field (e.g., Peixoto and Oort 1992). Large-scale waves, or ‘eddies’, are not only generated by stationary forcings, such as flow over orography and zonally-asymmetric diabatic heating (see section 1.3.1), but also by transient dynamical processes, such as flow instabilities (Haynes 2005).

In the extratropics, large-scale horizontal motions are nearly in hydrostatic and geostrophic equilibrium. This is also the case for the large-scale waves which interact with the mean flow and which are the main driver of the BDC. Therefore, the quasigeostrophic approximation is applicable for our purposes. One of the main simplifications of this approximation is, that horizontal advection of temperature and momentum only occurs due to the geostrophic wind. If pressure is taken as the independent vertical coordinate, the zonally-averaged, quasigeostrophic form of Equation (1.5) becomes

$$\frac{\partial[\bar{u}]}{\partial t} - f[\bar{v}] = -\frac{1}{a \cos^2 \phi} \frac{\partial[\bar{u}^* v^*] \cos^2 \phi}{\partial \phi} + [\hat{F}_\lambda], \quad (1.8)$$

where $f \equiv 2\Omega \sin \phi$ is the Coriolis parameter. The square brackets now denote the (Eulerian) zonal averages, and the asterisks denote the eddy fields, i.e., the local deviation from the zonal average. Note that the Coriolis term is merely a consequence of angular momentum conservation in the absence of a zonal torque, as described by Equations (1.4) and (1.5). The contribution by the zonal pressure-gradient force has disappeared in the $[\hat{F}_\lambda]$ term, since the zonal-mean of a zonal gradient vanishes per definition. It now represents the smaller-scale dissipative processes, e.g. surface friction, and is usually a

small term compared to the other terms. Equation (1.7) can also be written in its zonally-averaged, quasigeostrophic form, as

$$\frac{\partial[\theta]}{\partial t} + [\omega] \frac{d\theta_s}{dp} = \left(\frac{p_s}{p}\right)^{R/c_p} \frac{[J]}{c_p} - \frac{1}{a \cos \phi} \frac{\partial[v^* \theta^*] \cos \phi}{\partial \phi}, \quad (1.9)$$

where $\omega \equiv dp/dt$ denotes the pressure velocity, and $\theta_s(p)$ is the background potential temperature field, which only depends on the pressure. Now, we know from Equation (1.7) that potential temperature is conserved following adiabatic motion. Time-invariant, zonally-averaged vertical mass transport should therefore be determined by zonal-mean diabatic heating and the zonal-mean vertical potential temperature gradient. However, Equation (1.9) illustrates that $[\omega]$ cannot represent the steady Lagrangian zonal-mean vertical mass transport, since the latter could then also be adiabatically determined by the eddy heat flux. Dunkerton (1978) acknowledged this discrepancy and demonstrated that the eddy term actually describes the effect of a vertical Stokes' drift, which should be added to $[\omega]$ to obtain the quasi-Lagrangian mean vertical velocity. Andrews and McIntyre (1976) had already proposed to write Equation (1.9) in a Transformed Eulerian Mean (TEM) form,

$$\frac{\partial[\theta]}{\partial t} + \tilde{\omega} \frac{d\theta_s}{dp} = \left(\frac{p_s}{p}\right)^{R/c_p} \frac{[J]}{c_p}, \quad (1.10)$$

$$\text{where } \tilde{\omega} \equiv [\omega] + \frac{1}{a \cos \phi} \frac{\partial}{\partial \phi} \left(\frac{[v^* \theta^*] \cos \phi}{d\theta_s / dp} \right). \quad (1.11)$$

We can now regard $\tilde{\omega}$ as a quasi-Lagrangian zonal-mean pressure velocity, for which we can also define a quasi-Lagrangian zonal-mean *meridional* velocity. (Instead of 'quasi-Lagrangian', the term 'residual' is often used.) This residual-mean meridional velocity \tilde{v} should of course satisfy the condition of mass conservation, which yields the definition

$$\tilde{v} \equiv [v] - \frac{\partial}{\partial p} \left(\frac{[v^* \theta^*]}{d\theta_s / dp} \right). \quad (1.12)$$

The TEM version of the zonal-mean zonal momentum Equation (1.8) then takes on the following elegant form:

$$\frac{\partial [u]}{\partial t} - f\tilde{v} = \frac{1}{a \cos \phi} \nabla \cdot \mathbf{F} + [\hat{F}_\lambda], \quad (1.13a)$$

$$\text{where } \mathbf{F} = (F_\phi, F_p) \equiv a \cos \phi \left(-[u^* v^*], f \frac{[v^* \theta^*]}{d\theta_s / dp} \right). \quad (1.13b)$$

Here, the Eliassen-Palm flux (EP flux) \mathbf{F} is introduced as a two-dimensional vector in the meridional plane. The wave forcing on the zonal-mean flow is described by the divergence of the EP flux. The physical interpretation of \mathbf{F} is that of a wave-induced zonal-mean flux of westward (negative) angular momentum.

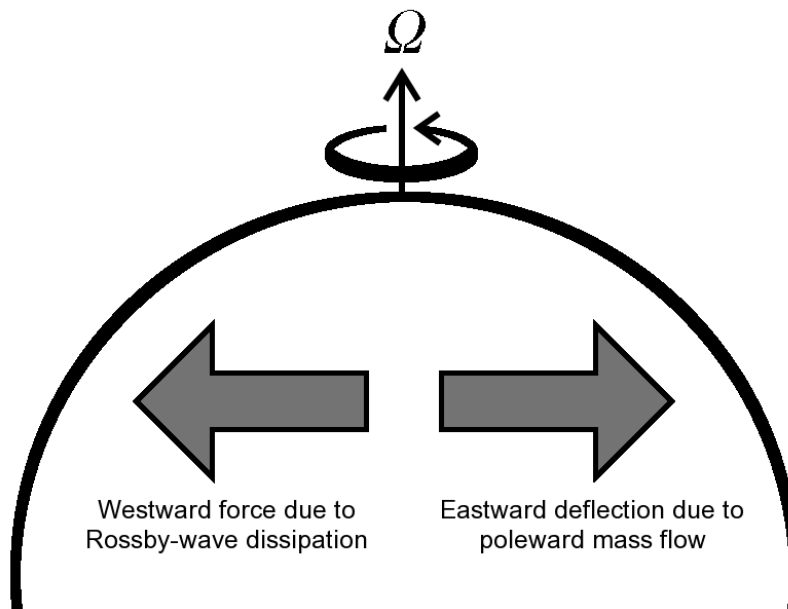


Figure 1.3: Time-averaged stratospheric balance between the westward wave drag and the eastward acceleration due to the Coriolis effect on the poleward residual meridional wind.

Where \mathbf{F} converges, a zonal-mean westward torque is exerted due to the deposition of the westward angular momentum. This is what happens in the upper, poleward branch of the BDC, predominantly due to breaking Rossby waves, which will be discussed later. With $[\hat{F}_\lambda]$ being small, the steady solution of Equation (1.13a) thus implies that the convergence of the EP flux is balanced by poleward flow (in both hemispheres), with $f\tilde{v} > 0$. This force balance is schematically illustrated in Figure 1.3.

1.2.4 Downward control principle

Haynes *et al.* (1991) postulated the so-called downward control principle, which states that the steady extratropical mass flow across an isentropic surface is determined by the steady angular momentum deposition *above* that surface. However, the net angular momentum deposition above a certain level is, in turn, controlled by the vertical component of the EP flux through that level. If we denote the area-weighted polar-cap average north of a reference latitude ϕ_r by $\langle \dots \rangle_{\phi_r}$, we can directly derive from Equation (1.11) that

$$\langle \tilde{\omega} \rangle_{\phi_r} \equiv \langle \omega \rangle_{\phi_r} + \frac{\cos \phi_r}{a(\sin \phi_r - 1)} \left\{ \frac{[v^* \theta^*]}{d\theta_s / dp} \right\}_{\phi_r}, \quad (1.14)$$

where the quantity between braces is evaluated at the reference latitude ϕ_r . If ϕ_r is chosen in such a way that the first r.h.s. term in Equation (1.14) is very small, the polar-cap residual-mean pressure velocity is thus proportional to the poleward eddy heat flux at ϕ_r . The strength of the downwelling north of ϕ_r will then be proportional to the poleward eddy heat flux $[v^* T^*]$ at ϕ_r . Newman *et al.* (2001) derived the same result from the downward control principle. For the lower stratosphere, they also found that at a latitude of 60°N, $\langle \omega \rangle_{\phi_r}$ is negligible. This is why the poleward eddy heat flux at mid- to subpolar latitudes in the lower stratosphere is a very useful diagnostic to quantify the wave driving of the BDC. Usually, $[v^* T^*]$ is averaged at 100 hPa over a broad latitude band around 60°N, e.g., between 40°-80°N. Since the first r.h.s. term in Equation (1.14)

is small on average in this region, the lower-stratospheric downwelling poleward of 60°N should be highly correlated with this wave diagnostic. The downwelling air warms due to adiabatic compression, which forces the air temperature above the radiative equilibrium temperature. On timescales longer than the radiative thermal damping timescale, the temperature profile will adjust in such a way that the dynamical heating by $\tilde{\omega}$ is balanced by diabatic cooling, which can also be derived from Equation (1.10). Figure 1.4 shows that the poleward eddy heat flux during midwinter can indeed explain a large fraction of

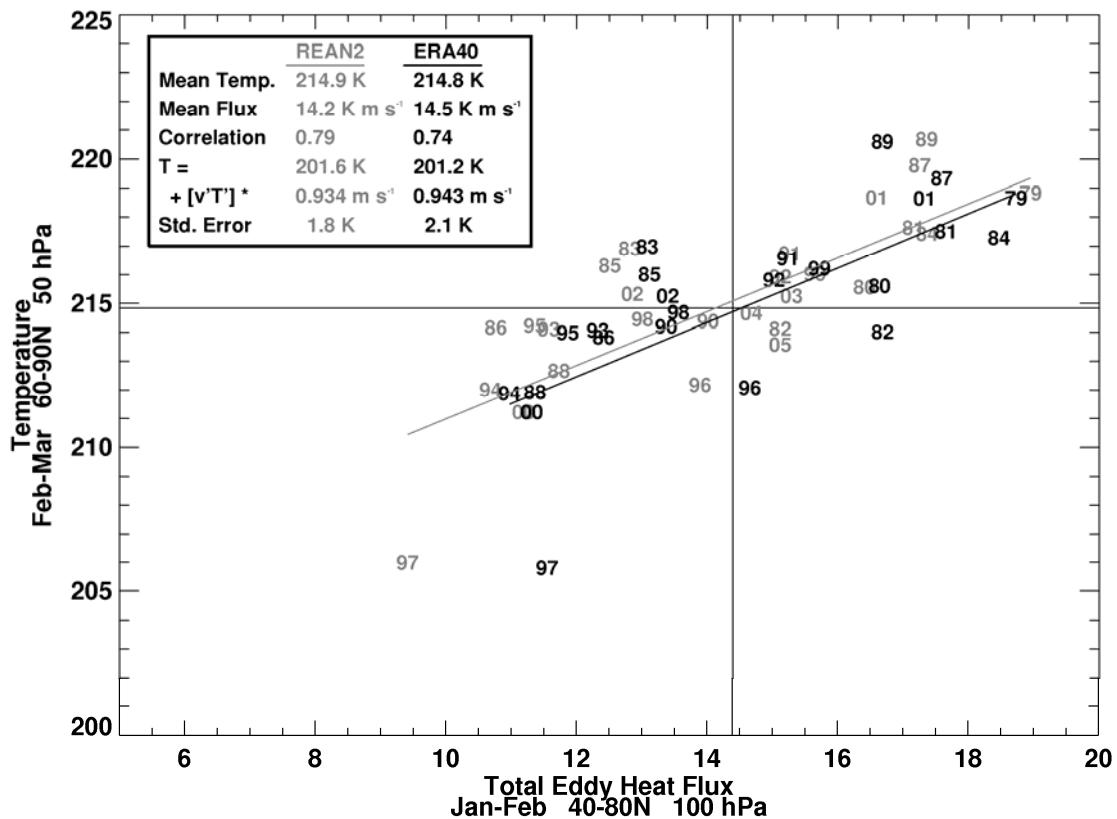


Figure 1.4: Temperature T (K) at 50 hPa, averaged for 60° - 90°N and February/March, plotted against the total poleward eddy heat flux $[v^*T^*]$ (K m s^{-1}) at 100 hPa, averaged for 40° - 80°N and for January/February. The individual years are as indicated. The plot is based on the NCEP/NCAR reanalysis 2 data (gray) and the ECMWF ERA40 data (black) for the period of 1979-2005. (source: Dr. Paul A. Newman, National Aeronautics and Space Administration, USA)

the interannual late-winter, early-spring temperature variability that is observed in the northern high-latitude lower stratosphere. Equation (1.13a) shows how the deposition of westward angular momentum drives the quasi-Lagrangian mean meridional circulation, averaged over longer timescales for which the zonal-mean zonal wind tendency becomes small. In the next chapter, we will discuss the type of waves that predominantly carry the westward angular momentum, Rossby or planetary waves, in greater detail.

1.3 Wave driving of the BDC

1.3.1 Rossby waves

In the Northern Hemisphere, Rossby or ‘planetary’ waves account for most of the wave driving of the BDC (e.g., Shepherd 2003). Rossby waves are large-scale longitudinal undulations in the flow along a latitude circle. Whereas for gravity waves the restoring mechanism is the vertical buoyancy force, for Rossby waves it is the meridional gradient in isentropic potential vorticity (IPV). IPV can be defined as

$$\text{IPV} = -g(f + \zeta) \frac{\partial \theta}{\partial p}, \quad (1.15)$$

where ζ is the vertical component of the relative vorticity on an isentropic surface,

$$\zeta \equiv \frac{1}{(a+z)\cos\phi} \left\{ \frac{\partial v}{\partial \lambda} - \frac{\partial(u\cos\phi)}{\partial \phi} \right\}_{\theta}. \quad (1.16)$$

The quantity between braces is evaluated at constant θ , which is indicated by the subscript. For frictionless, adiabatic flow, IPV is a conserved quantity, as is θ . This poses an important horizontal constraint on large-scale motions. The basic Rossby-wave propagation mechanism can readily be understood from the conservation of IPV. First, we discuss the barotropic case, for which the pressure difference between two isentropic surfaces is constant. Since g can also be regarded as a constant, conservation of IPV then

boils down to conservation of absolute vorticity, which is the bracketed term in Equation (1.15). Due to the increase of f with latitude, a northward/southward displacement will then always be associated with a decrease/increase in the relative vorticity ζ . This is depicted in Figure 1.5. From Equation (1.15), we can also see that the restoring mechanism becomes stronger in the case of a strong meridional IPV gradient. This is because a large increase of IPV with latitude implies that the anticyclonic/cyclonic circulation of an air sample that is displaced northward/southward will be stronger, relative to the circulation of the surrounding air. If the static stability, i.e. $-\partial\theta/\partial p$,

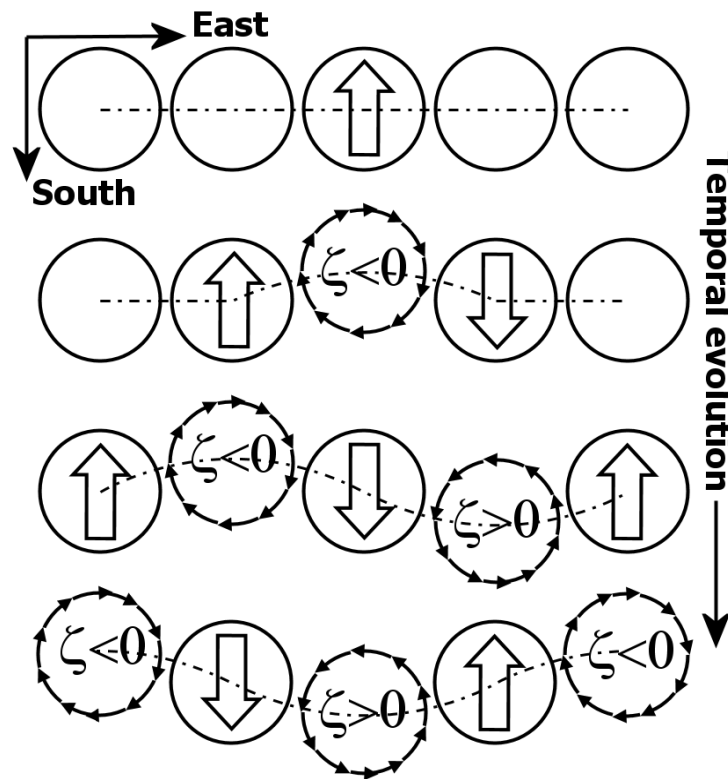


Figure 1.5: Illustration of westward barotropic Rossby-wave propagation relative to the zonal-mean flow, viewed from above (in the Northern Hemisphere). The small, solid arrows indicate the direction of the relative circulation; the big, hollow arrows indicate the local tendency of the meridional velocity. Initially, the relative vorticity ζ is zero everywhere, and the middle cylinder is pushed northward by a given forcing. Due to the increasing planetary vorticity f , ζ becomes negative. The induced relative circulation pushes the cylinder to the right southward and the cylinder to the left northward. The Rossby-wave pattern thus propagates westward. Note that a uniform zonal background flow would only advect the whole pattern, so that Rossby-wave propagation is always westward relative to the zonal-mean flow.

varies on an isentropic surface, IPV conservation is not equivalent to absolute vorticity conservation, due to ‘squeezing’ and ‘stretching’ of absolute vorticity. Figure 1.6 illustrates this effect for isentropic flow across an infinitely long north-south oriented mountain ridge. The isentropic surfaces will tend to be packed together vertically above the ridge, because the isentropic surfaces tend to follow the orography in order to satisfy the kinematic boundary condition, which does not allow for a velocity component perpendicular to the lower boundary at the boundary itself. At upper levels, the upward bulging of the isentropic surfaces begins somewhat further upstream and ends further downstream, due to the dynamic pressure forces that are associated with the interaction between the mountain ridge and the flow.

The changes in relative vorticity that are induced by the topography create meridional air displacements that generate a quasi-stationary Rossby-wave pattern downstream of the topography, according to the Rossby-wave propagation mechanism in

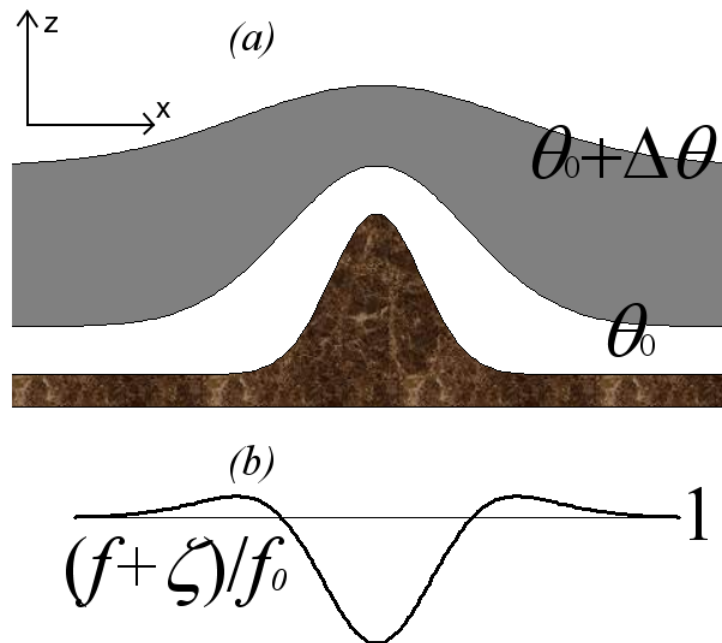


Figure 1.6: Schematic illustration of IPV conservation in zonal flow over a surface topography: (a) the stretching/squeezing of the air column between the two isentropic surfaces yields an increase/decrease in the absolute vorticity $f+\zeta$, for which (b) shows the relative variation with x , where f_0 is the Coriolis parameter at the initial latitude and the initial relative vorticity is assumed to be zero.

Figure 1.5. Note that stationary Rossby waves can only be generated in an eastward flow, since they always propagate westward relative to the mean flow.

Stretching and squeezing of absolute vorticity is not only forced by flow across topography, such as the Tibetan plateau and the Rockies. Also thermal land-sea contrasts and the divergent upper-tropospheric wind patterns due to large-scale convection form important Rossby-wave sources (e.g., Held et al. 2002).

1.3.2 Rossby-wave propagation in the meridional plane

The westward phase propagation of Rossby waves w.r.t. the mean flow decreases for waves with higher zonal wavenumbers, i.e., with a larger number of waves spanning a latitude circle. Longer waves thus travel westward faster w.r.t. the zonal-mean wind. It was already noted that stationary Rossby waves, which dominate the Rossby-wave spectrum in the stratosphere, can only exist in an eastward zonal-mean flow, since they can never propagate westward w.r.t. to an already westward mean flow and still be stationary. Furthermore, the stronger the eastward zonal-mean wind, the longer the waves will have to be to still be stationary. If eastward flow is too strong, even the longest Rossby waves, i.e. those spanning an entire latitude circle, become impossible (Charney and Drazin 1961). In the summer hemisphere, the zonal-mean flow is westward, inhibiting the vertical propagation of stationary Rossby waves into the stratosphere. The westward flow is a result of stronger solar heating in the stratosphere at the summer pole than at the equator, by which the stratospheric meridional temperature gradient reverses sign, and the thermal wind turns westward. In the winter hemisphere, the flow is eastward, and Rossby waves are able to propagate upward. However, the ultralong Rossby waves (wavenumbers 1-3) dominate the wave spectrum due to the ‘low-pass filter’ effect of the eastward upper-tropospheric jet. The wave driving of the stratosphere therefore not only depends on the generation of wave activity in the troposphere, but also on how the vertical and meridional propagation of the wave activity is affected by the zonal-mean zonal wind field (e.g., Matsuno 1970).

1.3.3 Wave dissipation and westward angular momentum deposition

We have previously discussed that the penetration of Rossby waves into the stratosphere depends on their zonal wavenumber, their phase speed, and the zonal-mean zonal wind distribution. The wave driving of the BDC is therefore predominantly determined by the Rossby-wave spectrum that is generated, and on the pathways of these waves in the meridional plane. The EP flux \mathbf{F} that is carried by Rossby waves can be shown to be proportional to the group velocity, at which the wave energy is propagated, for those waves. Therefore, the EP flux can be used to trace the Rossby-wave energy in the meridional plane, by a method called “ray tracing” (e.g., Karoly and Hoskins 1982). The waves that are able to reach the lower stratosphere drive the BDC, according to the aforementioned downward control principle, through the process of wave dissipation. We will next discuss how this wave dissipation yields the westward force that drives the BDC. Assuming small wave amplitudes and using quasigeostrophic scaling, Andrews *et al.* (1987) demonstrated that both components of the EP flux \mathbf{F} can be regarded as the zonal-mean zonal “form drag” per unit area along a material surface, e.g., an isentropic surface. This is the same kind of form drag that is found in flow across a bottom topography, where dynamic high pressure perturbations are found on the upwind slopes and low pressure perturbations are found on the downwind slopes, yielding a net ‘orographic drag’ on the flow. For zonal flow, this orographic drag is associated with the exchange of angular momentum between the earth’s (material) surface and the atmosphere. For the vertical component of \mathbf{F} , the zonal surface force is exerted by the air above a material surface on that below, if this material surface is vertically distorted by adiabatic waves. The surface drag force per unit area translates into a zonal-mean volume force, once it has a non-zero divergence, which is illustrated in Figure 1.7 and is mathematically described by Equation (1.13a). A similar ‘wave drag’ interpretation holds for meridional distortions of a material surface which are dissipated in the meridional direction.

But what does Rossby-wave breaking look like, and what triggers it? McIntyre and Palmer (1983, 1984) have used the rapid, irreversible deformation of material

contours, e.g., IPV¹ contours on an isentropic surface, as the defining property of Rossby-wave breaking. This kind of irreversible contour deformation can be triggered when non-linear processes begin to dominate the evolution of the flow. Particularly, waves tend to break when they propagate into a region where their intrinsic zonal phase speed, i.e., the phase speed relative to the mean flow, becomes zero (e.g. Andrews et al. 1987). This is where the zonal advection by the wave becomes comparable in magnitude to the zonal advection by the mean flow, enabling the irreversible, sideways (isentropic) overturning of IPV contours. For stationary waves, these conditions are met at the ‘zero wind surface’, but more generally, regions where the intrinsic phase speed of a Rossby wave

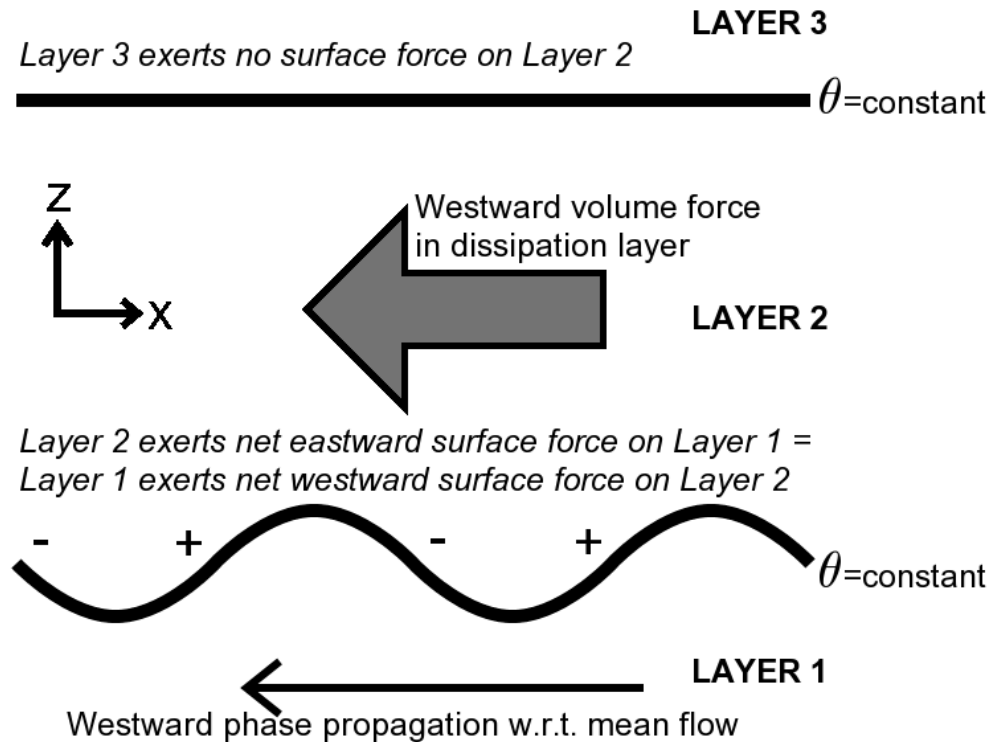


Figure 1.7: Schematic picture of the westward volume force that is exerted by dissipating Rossby waves on a layer between two isentropic, material surfaces (Layer 2). The plus and minus signs on the lower isentropic surface indicate zonal pressure perturbations. Without wave dissipation, the net volume force on Layer 2 would be zero because of the canceling eastward surface force at the top of Layer 2, exerted by Layer 3. With complete wave dissipation in Layer 2, a net westward volume force is exerted on Layer 2.

¹ The definition of IPV was given in Equation (1.15).

becomes zero are called ‘critical layers’. The westward angular momentum deposition by breaking Rossby waves manifests itself as a meridional ‘stirring’ of IPV by the breaking waves. Figure 1.8 illustrates how this IPV stirring constitutes a westward force if the meridional IPV gradient is positive, which is true in the extratropics. In the steady-state solution, this westward force does not produce a westward acceleration, but is completely balanced by the eastward Coriolis deflection of the poleward mass flow in the BDC (see Figure 1.3). If upward propagating Rossby waves do not encounter a critical surface, wave dissipation will eventually occur due to non-linearity, as they grow in amplitude with decreasing density.

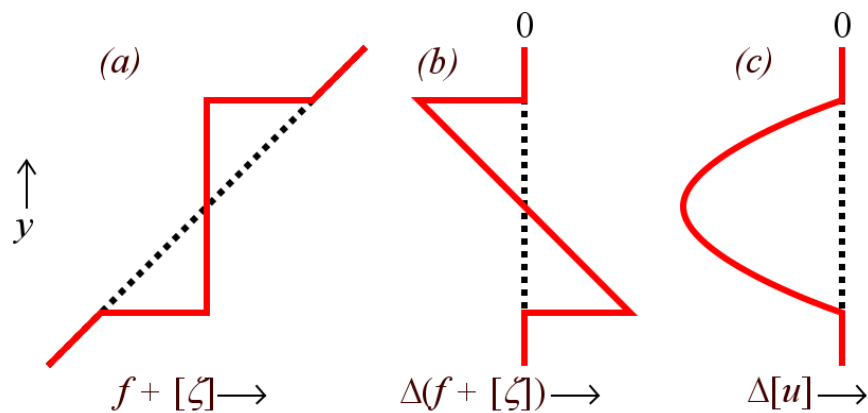


Figure 1.8: Idealized illustration of the westward angular momentum deposition due to meridional IPV stirring on an isentropic surface in breaking Rossby waves. If static stability is assumed constant, IPV is proportional to absolute vorticity. In (a), the black, dotted line shows the initial zonal-mean meridional distribution of absolute vorticity, which increases with y ; the red, solid line shows the profile after the stirring. In (b), the red, solid line shows the change in zonal-mean absolute vorticity after the mixing, and in (c), the corresponding change in the zonal-mean zonal wind (see Equation (1.16)) is shown. After a figure by P.H. Haynes.

1.4 Overview of this thesis

To summarize, the BDC is a slow, hemispheric-scale meridional overturning circulation in the stratosphere with air moving poleward and downward in the extratropics, and upward in the tropics. It determines the rate at which ODSs are destroyed and leads to the

net production of ozone. The BDC is mainly a response to breaking Rossby waves during the winter season. Rossby waves of tropospheric origin dominate the wave driving of the BDC, and the upward propagation from the troposphere depends on their zonal wavenumber and on the zonal-mean zonal wind distribution. Therefore, the strength of the BDC can be modified by changes in the amplitude spectrum of the Rossby waves, as well as in the location where the waves are generated. Also, changes in the zonal-mean zonal wind pattern could alter the wave driving of the BDC.

This thesis discusses the wave-mean flow interaction and the variability of the BDC for the NH, where most of the wave driving of the stratosphere can be attributed to resolved, planetary waves in the extratropics.

The following questions will be addressed:

1. How do observations compare to a quasigeostrophic model for the frequency-dependent response of the zonal-mean flow to extratropical wave forcing?
2. To what extent is the interannual variability of the total poleward eddy heat flux at 100 hPa determined by the flux at lower levels?
3. To which type of waves can most of the interannual variability of the lower-stratospheric wave forcing be attributed?
4. Is the interannual variability of the wave driving primarily controlled by the waves' amplitude or by the structure of the waves which determines the efficiency of the poleward eddy heat transport?
5. What causes the strengthening of the northern-winter wave driving of the BDC in an enhanced-CO₂ climate simulation?

The first question deals with the zonal-mean angular momentum budget in Equation (1.13a). How the angular momentum deposition by large-scale planetary waves is distributed between both l.h.s. terms of Equation (1.13a), i.e., the relative and planetary angular momentum reservoirs, depends on the timescale of the forcing. However, the details of this frequency dependence are a function of the thermal damping timescale, as

well as the ratio between the meridional and vertical extent of the induced meridional circulation.

The observed midlatitude response of the zonal-mean flow to wave forcing on different timescales and different vertical levels was compared with a quasigeostrophic model for this response. Here, ‘observed’ implies according to ECMWF 4D-Var analysis data for six extended winter seasons from November to April 1999/2000 to 2004/2005. Fourier analysis was used to obtain power spectra of the terms in Equation (1.13a). Based on the theoretical prediction, height-dependent estimates for both the thermal-damping time and the aspect ratio are derived. **Chapter 2** is devoted to this analysis, which has been published in *Atmospheric Chemistry and Physics (ACP)* as Haklander et al. (2006).

Chapter 3 is a slightly modified version of a second *ACP* paper that has been published as Haklander et al. (2007). Questions 2, 3 and 4 have been addressed in this paper. Hereto, 24 years of ERA-40 Reanalysis data were used to study the year-to-year variability of the wave driving of the NH-winter BDC. As was discussed in section 1.7, the main proxy that was used to quantify the wave driving of the BDC was the 100-hPa poleward eddy heat flux averaged over January-February and 40°-80°N. The second question was addressed by correlating the heat flux at 100 hPa with that at other levels. Regarding the third question, a zonal Fourier decomposition was performed. Linear regression analysis was employed for the attribution of the observed interannual variability in the heat flux to the various zonal wavenumbers in the spectrum. Also, a distinction was made between the contribution by stationary and transient waves. To address the fourth question, year-to-year variations in the wave driving were described as the product of wave amplitude and heat-flux ‘efficiency’, which depends on the zonal correlation between the meridional wind and temperature fields.

Chapter 4 deals with question 5, focusing on how CO₂ doubling can strengthen the wave driving of the BDC. Results from a doubled CO₂ experiment by the middle-atmosphere ECHAM4 model were compared to the results from a control experiment. The increased wave driving due to CO₂ doubling was investigated in terms of the various wave components that contribute to the total heat flux at 100 hPa. Additionally, changes in the EP flux were investigated as a function of latitude and height. Finally, it was examined whether the simulated increase of the wave driving was primarily due to an

increase in wave amplitude or by a higher efficiency of the poleward eddy heat transport. Chapter 4 has been published as Haklander et al. (2008) in *Geophysical Research Letters*, and is the third paper of this thesis. Finally, a summary and outlook is provided in **Chapter 5**.

2

Analysis of the frequency-dependent response to wave forcing in the extratropics[†]

Abstract

A quasigeostrophic model for the frequency-dependent response of the zonal-mean flow to planetary-wave forcing at Northern Hemisphere (NH) midlatitudes is applied to 4D-Var ECMWF analysis data for six extended winter seasons. The theoretical response is a non-linear function of the frequency of the forcing, the thermal damping time α^{-1} , and a scaling parameter μ which includes the aspect ratio of the meridional to the vertical length scale of the response. Regression of the calculated response from the analyses onto the theoretical response yields height-dependent estimates for both α^{-1} and μ . The thermal damping time estimated from this dynamical model is about 2 days in the troposphere, 7-10 days in the stratosphere, and 2-4 days in the lower mesosphere. For the stratosphere and lower mesosphere, the estimates lie within the range of existing radiative damping time estimates, but for the troposphere they are significantly smaller. The results indicate that the quasigeostrophic model is applicable to midlatitude wintertime conditions.

[†]This Chapter is a slightly revised version of: Haklander, A. J., P. C. Siegmund, and H. M. Kelder: Analysis of the frequency-dependent response to wave forcing in the extratropics, *Atmos. Chem. Phys.*, 6, 4477–4481, 2006.

2.1 Introduction

In NH midlatitude winter, planetary waves strongly interact with the zonal-mean flow. This interaction occurs at a broad range of timescales. For instance, the intense growth of a sudden stratospheric warming (SSW) event can occur in just a few days, its mature stage typically lasts a few weeks, and the total SSW cycle from preconditioning to recovery of the polar vortex can last a few months (e.g. Limpasuvan et al. 2004). Randel et al. (2002) found that the power spectrum of equatorial upwelling shows a broad maximum at periods between 10-40 days, and they argued that this is associated with episodes of planetary-wave activity at midlatitudes. The midlatitude zonal forcing by planetary waves also exhibits an annual cycle (e.g. Rosenlof 1995). During winter, westerly stratospheric winds allow the vertical propagation of planetary waves emanating from the troposphere, whereas the summertime easterlies block the planetary waves. The angular momentum that is deposited by the waves is distributed between the relative and planetary reservoirs of angular momentum (e.g. Peixoto and Oort 1992). This is expressed by the quasigeostrophic transformed Eulerian mean (TEM) zonal momentum equation,

$$\frac{\partial [u]}{\partial t} - f\tilde{v} = [M], \quad (2.1)$$

where the square brackets denote zonal averages, $[u]$ is the zonal-mean zonal wind, f is the Coriolis parameter, \tilde{v} is the meridional component of the residual circulation, and $[M]$ is $a \cos \phi$ times the wave-induced angular momentum deposition per unit mass (e.g. Holton et al. 1995). The tendency of the relative angular momentum is described by $\partial [u] / \partial t$, that of the planetary angular momentum by $-f\tilde{v}$. Garcia (1987) derived an expression for the frequency dependence of the $\partial [u] / \partial t$ response to a given zonal wave forcing $[M]$. According to this expression, the wave-induced angular momentum deposition at high frequencies is distributed about equally between the relative and angular momentum reservoirs. It was found that, away from the high-frequency limit, the

rates of frictional dissipation and thermal relaxation toward radiative equilibrium determine the frequency dependence of the response. The timescale of thermal damping is important, since for non-zero $\partial[u]/\partial t$ it determines how efficiently the meridional circulation is able to restore thermal-wind equilibrium through the adiabatic adjustment of the meridional temperature gradient. In the low-frequency limit, which defines the Brewer-Dobson circulation, the thermal response to the wave forcing is fully damped by thermal relaxation, implying that the angular momentum of the waves is deposited into the planetary reservoir only. Although Garcia's model provides valuable insights into the frequency dependence of the balance in Equation (2.1), it has not been tested with real atmospheric data. In this study, we apply this model to wind and temperature analyses from the ECMWF model. Since the stratospheric diabatic heating during summer is no longer slaved to the wave forcing, we base our analysis on NH winter (November to April) data only. For each of the three terms in Equation (2.1), power spectra estimates are computed, using six winters of 12-hourly analysis data. Estimates for the vertical profiles of the thermal damping time and the high-frequency limit of the response are obtained, using a least-squares method to fit the theoretical frequency dependence of the response of $\partial[u]/\partial t$ to $[M]$ onto the analyzed data. It should be emphasized that we are estimating the 'effective' thermal damping time, which in the troposphere is significantly shorter than the radiative damping time (e.g. Wu et al. 2000). The thermal damping times derived in the present study are assumed to represent all thermal dissipative processes, such as turbulent heat transfer and convection.

2.2 Frequency-dependent TEM model

In the TEM model used by Garcia (1987), infrared cooling is parameterized by Newtonian cooling with thermal damping rate α , and gravity-wave drag is parameterized by Rayleigh friction with coefficient K_R . The forcing is assumed to be entirely due to the Eliassen-Palm (EP) flux divergence of planetary waves, and thereby the forcing due to shortwave radiative heating is neglected. To study the frequency dependence of the zonal-mean flow response, a harmonic wave forcing at angular frequency ω is assumed, i.e., $[M] = \text{Re}([M]_{\omega} e^{i\omega t})$. The zonal-mean zonal wind field can then be written as

$[u] = \text{Re}([u]_{\omega} e^{i\omega t})$. Garcia (1987) derived that the complex amplitude $i\omega[u]_{\omega}$ of the zonal-mean zonal wind tendency Fourier component with angular frequency ω can be approximated as

$$i\omega[u]_{\omega} \approx \mu \frac{(1 + \mu) + (\alpha / \omega)i}{(1 + \mu)^2 + (\alpha / \omega)^2} [M]_{\omega}, \quad (2.2)$$

where μ is a real, non-dimensional scaling parameter defined as $\mu \equiv L_z^2 N^2 / (L_y f)^2$, which is typically $O(1)$ in the extra-tropics. N^2 denotes the square of the buoyancy frequency, and L_y and L_z denote the meridional and vertical scales of the response. Equation (2.2) is identical to the expression found by Garcia (Equation (14), 1987), but with K_R set to zero. Rayleigh friction introduces a non-physical momentum sink (e.g. Shepherd and Shaw 2004), and it is difficult to argue that a linear drag such as Rayleigh friction is at all relevant in the stratosphere (Haynes 2005). For these reasons, we have not adopted this parameterization in the present study. To compare the magnitudes of the Fourier components, we multiply both sides of Equation (2.2) with their complex conjugate. Subsequently taking the square root of both sides yields the response function r ,

$$\frac{|\partial[u]_{\omega} / \partial t|}{|[M]_{\omega}|} \sim r(\alpha, \mu, \omega), \text{ with } r(\alpha, \mu, \omega) \equiv \frac{\mu}{\sqrt{(1 + \mu)^2 + (\alpha / \omega)^2}}. \quad (2.3)$$

In the high-frequency limit Equation (2.3) converges to $(1 + \mu^{-1})^{-1}$, and in the stationary limit it converges to zero. Garcia (1987) set $\mu = 1$, but we allow μ to be a function of height.

2.3 Data and method

For this study, we have used 12-hourly operational ECMWF four-dimensional variational (4D-Var) analysis data for six NH winters (November to April) from

1999/2000 to 2004/2005. The wind and temperature fields were retrieved for a latitude-longitude grid of $1^\circ \times 1^\circ$ at 35 pressure levels: 1000, 925, 850, 700, 500, 400, 300, 250, 200, 150, 100, 70, 66.6, 54.6, 44.3, 35.8, 28.9, 23.3, 18.8, 15.2, 12.3, 9.9, 8.0, 6.4, 5.2, 4.2, 3.4, 2.7, 2.1, 1.6, 1.2, 0.8, 0.5, 0.3, and 0.1 hPa.

From above the planetary boundary layer to the upper stratosphere, the mechanical acceleration term $[M]$ in Equation (2.1) is principally due to planetary-wave forcing. In the TEM framework, this forcing is well approximated by the divergence of the EP flux,

$$[M] \approx \frac{1}{a \cos \phi} \left[\frac{1}{a \cos \phi} \frac{\partial(F^\phi \cos \phi)}{\partial \phi} + \frac{\partial F^p}{\partial p} \right], \quad (2.4)$$

where p denotes pressure, and F^ϕ and F^p denote the two components of the EP flux vector \mathbf{F} (e.g. Peixoto and Oort 1992). We performed our analysis at 60°N , since planetary-wave forcing is known to reach a maximum there (Christiansen 2001), which increases the validity of our assumption that $[M]$ is well-represented by Equation (2.4).

For each of the six November to April seasons, we have calculated the Fourier transforms of $\partial[u]/\partial t$, $f\tilde{v}$, and $[M]$ separately. The six independent power spectra estimates were subsequently averaged at each frequency. By taking the square root of the ratio between the power estimates for $\partial[u]/\partial t$ and $[M]$, an estimate was obtained for the frequency-dependent response of $\partial[u]/\partial t$ to the wave forcing $[M]$. Subsequently, we performed a least-squares fit of the theoretical response function r , defined in Equation (2.3), to the ratios from the analyzed data. Here Equation (2.3) is written as $r^{-2} \equiv a + b\omega^{-2}$, with $a \equiv (1 + \mu^{-1})^2$ and $b \equiv \alpha^2 \mu^{-2}$. Estimating a and b then implies performing a linear least-squares regression analysis with r^{-2} and ω^{-2} as known dependent (y) and independent (x) variables, respectively. With this spectral analysis, estimates for both α^{-1} and $(1 + \mu^{-1})^{-1}$ were obtained at all 35 pressure levels, where $\alpha^{-1} \equiv (\sqrt{a} - 1)/\sqrt{b}$ and $(1 + \mu^{-1})^{-1} \equiv 1/\sqrt{a}$. The goodness of fit is expressed by R^2 , which is the square of the correlation coefficient of r^{-2} and ω^{-2} .

ERA-40 is produced by the European Centre for Medium-Range Weather Forecasts (ECMWF). The meteorological fields were retrieved for a lat-lon grid of $2.5^\circ \times 2.5^\circ$ between 0° - 90° N, at 23 pressure levels between 1000 and 1 hPa.

2.4 Results

Figure 2.1 shows the power spectrum estimates for the middle stratosphere at 9.9 hPa. This example is qualitatively representative for the stratosphere, with generally decreasing power for the forcing term $[M]$ and the Coriolis term $f\tilde{v}$ as the frequency increases. At timescales of 10-40 days, a broad maximum is found in the power spectra

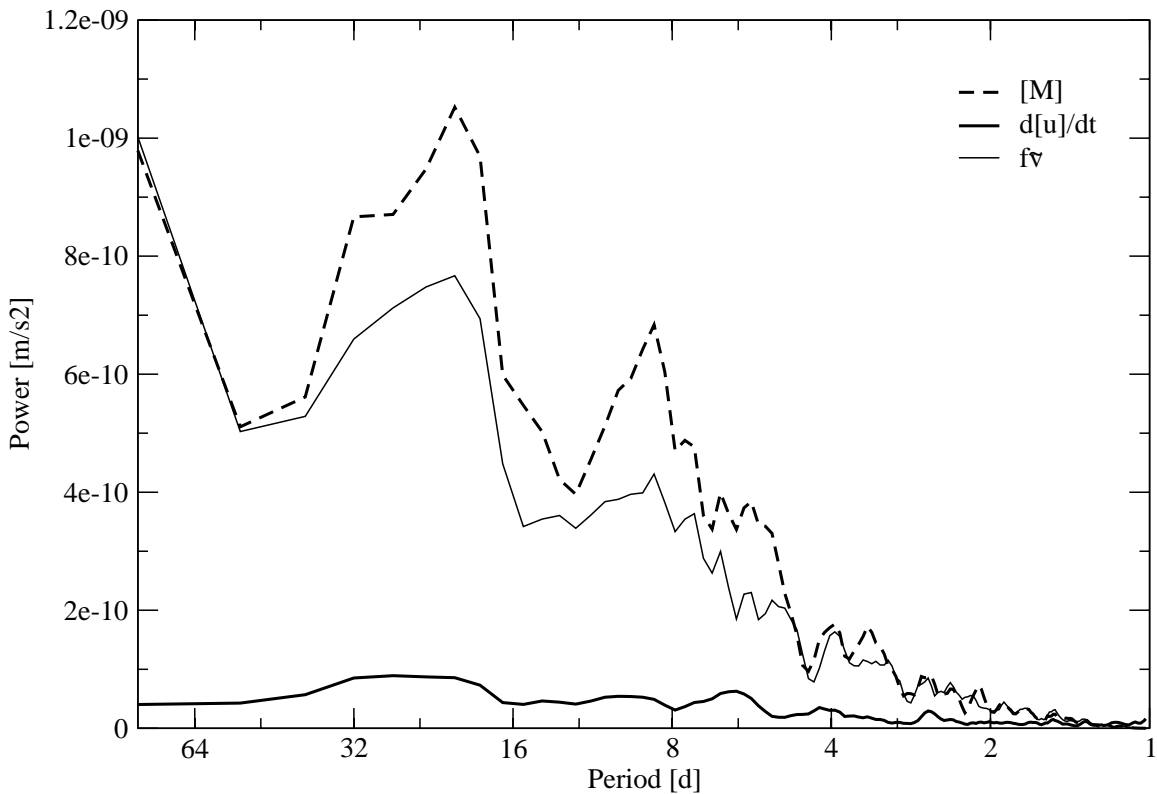


Figure 2.1: Power spectrum estimates for the Nov-Apr season at 60° N for $\partial[u]/\partial t$ (thick solid line), $f\tilde{v}$ (thin solid line), and $[M]$ (dashed line) at the 9.9 hPa level. The spectral estimates have been smoothed using five-point averages.

Randel et al. (2002). At all frequencies, the estimate of $|\partial[u]_{\omega} / \partial t|^2 = \omega^2 |[u]_{\omega}|^2$ is clearly smaller than that of the forcing, roughly following the maxima and minima of the spectral power estimates for $f\tilde{v}$ and $[M]$, as expected from Equation (2.3). The symbols in Figure 2.2 show the (non-smoothed) frequency dependence of the estimated ratios $|\partial\bar{u}_{\omega} / \partial t| / |\bar{M}_{\omega}|$ at 0.1 hPa, 9.9 hPa, and 1000 hPa. At all three levels, the ratio increases with increasing frequency, as expected from Equation (2.3). The theoretical least-squares fits are based on the ratios at 45 angular frequencies, from $2*(2\pi) \text{ yr}^{-1}$ to $90*(2\pi) \text{ yr}^{-1}$, with steps of $2*(2\pi) \text{ yr}^{-1}$. Higher frequencies, i.e., timescales shorter than about 4 days, are not included, since inconsistencies between subsequent analyses lead to non-physical variability at high frequencies. The dashed lines in Figures 2.3a and 2.3b show the computed vertical profiles of, respectively, the thermal damping time α^{-1} and the high-frequency limit $(1 + \mu^{-1})^{-1}$ of the response. The regression estimate of the thermal damping time is about 2 days in the troposphere (below 250 hPa), increasing to 7-10 days in the stratosphere and decreasing to 2-4 days in the lower mesosphere (above 1 hPa). The standard errors of these results are typically 4 days in the troposphere, 30 days in the stratosphere, and 10 days in the lower mesosphere. The standard errors become larger for longer thermal damping times, since the regression is then sensitive to the ratios at low frequencies, where the spectral resolution is relatively low. The sensitivity of R^2 (dotted line in Figure 2.3b) to the thermal damping time estimate is clearly seen when comparing it with Figure 2.3a. The solid lines in Figures 2.3a and 2.3b show the profiles that only include points with $R^2 > 0.1$. The estimated stratospheric α^{-1} profile then becomes much smoother, whereas the $(1 + \mu^{-1})^{-1}$ estimate is less sensitive. We first compare our estimates of α^{-1} from the frequency-dependent TEM model with those calculated by Newman and Rosenfield (1997, Figure 3; hereafter NR97), who used a radiative transfer model to derive thermal damping times as a function of latitude, height, and season. The damping times found in our study are generally shorter than their estimates for November to April at 60°N, but in the upper stratosphere, the agreement is quite good, especially considering the large stratospheric standard errors. In the lower stratosphere and

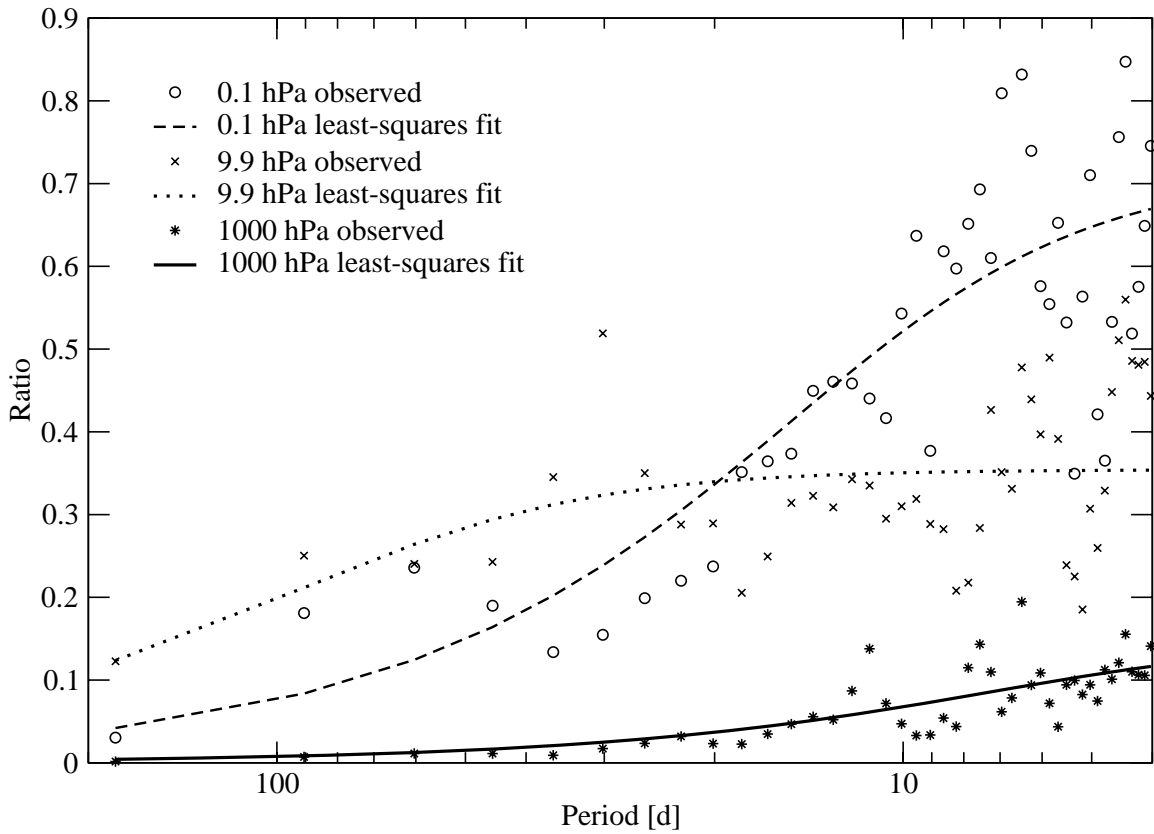


Figure 2.2: Estimates (symbols) for the Nov-Apr season at 60°N for the ratio $|\partial[u]_\omega / \partial t| / |[M]_\omega|$ at 0.1 hPa, 9.9 hPa, and 1000 hPa. Each line represents the least-squares fit of the theoretical response function to the observed ratios.

troposphere however, our α^{-1} estimates are much smaller than those of NR97, who calculated wintertime damping times of 35-40 days at 100 hPa. Held and Suarez (1994) proposed a profile which for 60°N yields an α^{-1} of 26 days at 1000 hPa, linearly increasing to 40 days at 700 hPa and above. With our tropospheric α^{-1} estimates of about 2 days and a standard error of about 5 days, the differences can be called significant. Concerning tropospheric thermal damping times, little consensus exists in the literature. This was also acknowledged by Burde (1999), who stated that α^{-1} is typically set to be the order of several days in the troposphere. Prinn (1977) pointed out that, especially at low levels, thermal damping times will often be significantly overestimated if calculations do not include the effect of the conducting and radiating surface. Applying his analytical expression for α^{-1} , tropospheric temperature perturbations with a vertical

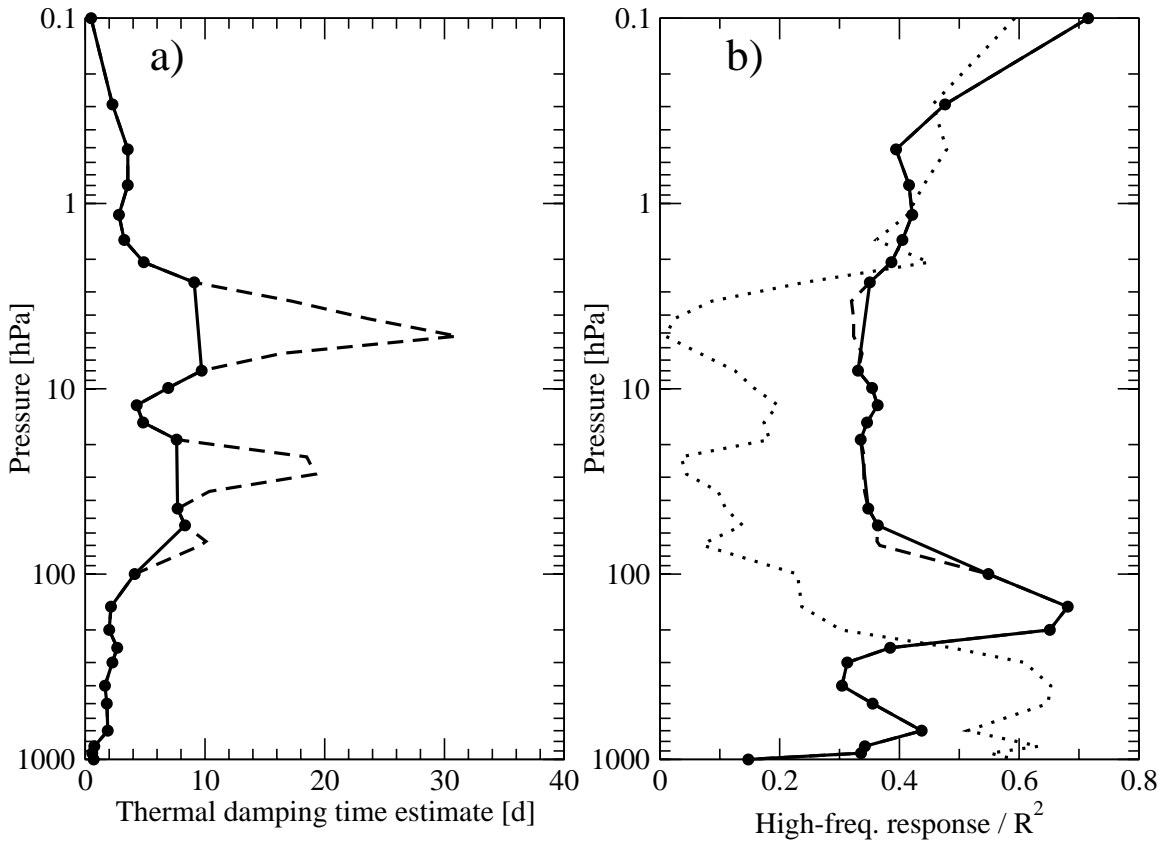


Figure 2.3: Estimates for the November-April season at 60°N for a) the thermal damping time α^{-1} and b) the high-frequency limit of the response $(1 + \mu^{-1})^{-1}$, as a function of pressure. The dashed lines show the estimates at all levels, the solid lines only show the estimates at the levels where R^2 , the fraction of the variance of $|\partial[u]_{\omega} / \partial t| / |[M]_{\omega}|$ that is accounted for by the least-squares regression, exceeds 10%. The dotted line in b) shows R^2 for the least-squares theoretical fit.

wavelength of about 3 km ($n^{-1} = 0.5$ km) at an average temperature $T_0 = 263$ K are thermally damped (mainly by water vapor) with α^{-1} as short as 0.7 to 2.0 days. Therefore, the tropospheric thermal damping times found in this study lie just within the range of existing radiative timescale estimates. However, for the troposphere, it is difficult to justify a direct comparison between our estimates for the effective thermal damping times and the radiative damping times derived in other studies. The effective thermal damping time is likely (much) shorter where thermal dissipation by turbulence and convection plays a role (Wu et al. 2000). This may explain why the effective

damping times we find are on the (very) short end of the existing range of radiative damping time estimates, especially at low levels.

The high-frequency limit of the response (Figure 2.3b) is generally quite constant with height and has a standard error of approximately 0.2. In the stratosphere, at high frequencies, the ratio between $|\partial[u]_{\omega}/\partial t|$ and $|[M]_{\omega}|$ generally converges to 0.33-0.37. Alternatively, μ converges to 0.5-0.6, which is indeed $O(1)$ as stated by Garcia (1987). The $(1 + \mu^{-1})^{-1}$ profile has a remarkable maximum near 150 hPa. This suggests that in the lowermost stratosphere, the variability of $\partial[u]/\partial t$ is less dominated by angular momentum deposition by planetary waves, and more by conservation of absolute angular momentum. Power spectrum estimates at 150 hPa (not shown) indicate that the variability of $[M]$ is indeed small compared to that of both $\partial[u]/\partial t$ and $f\bar{v}$. The rapid decrease of the $(1 + \mu^{-1})^{-1}$ estimate at the lowest levels is explained by the damping effect of surface drag on $\partial[u]/\partial t$, which is not included in our calculation of $[M]$.

2.5 Discussion and conclusions

In this paper, we have applied the frequency-dependent TEM model of Garcia (1987) to wind and temperature analyses from the ECMWF model. Six November-April seasons of 4D-Var analysis data at 35 levels were used to derive power spectra for the planetary-wave forcing (EP flux divergence), the zonal-mean zonal wind tendency, and the Coriolis acceleration associated with the residual meridional wind. We have used 4D-Var data, since 3D-Var analyses are known to yield a less realistic age of air in the stratosphere, which is mainly determined by the strength of the wave forcing (e.g. Scheele et al. 2005). We find that the theoretical response curve fits reasonably well onto the response derived from ECMWF analyses, with best agreement in the troposphere as well as in the upper stratosphere and lower mesosphere. Based on least-squares fits, estimates were obtained for the vertical profile of the effective thermal damping time and the high-frequency limit of the response. The analysis was performed at 60°N, where the resolved planetary-wave forcing $[M]$ reaches a maximum. The forcing, given by Equation (2.4), does not incorporate the zonal momentum deposition due to breaking

gravity waves, which is known to play an important role in the mesosphere. In addition, the forcing might be contaminated by physical inconsistencies in the data due to the assimilation process. To reduce the impact of these inconsistencies, timescales shorter than about 4 days were omitted from the analysis.

In this study, the scaling parameter μ is assumed to be a function of height only. However, Holton et al. (1995) argued from a scaling analysis of the vertical mass flux equation, that μ should have a particular frequency dependence, to allow for a non-zero vertical mass flux outside the forcing area. Based on their arguments, we obtain $\mu \approx \sqrt{1 + \alpha^2 / \omega^2} \max(1, L_z / H)$, where $H \approx 7$ km is the mean scale height. This yields an aspect ratio of $L_y / L_z \leq N / f$ for all frequencies, whereas we find an aspect ratio that is in general about 35% larger than N / f . Only in the lower stratosphere, where the forcing $[[M]_{\omega}]$ is relatively weak, we find $L_y / L_z \leq N / f$. Our results therefore suggest that the aspect ratio scaling argument of Holton et al. (1995) is not applicable well inside the forcing region. For instance, the net meridional response may actually consist of multiple shallow meridional cells. This would yield a larger aspect ratio inside the forcing region, and a lower “effective” aspect ratio outside the forcing area, which still satisfies the condition $(L_y / L_z)_{\text{eff}} \leq N / f$. Furthermore, substituting μ in Equation (2.2) leads to non-physical behavior at low frequencies, since the stationary limit $\omega \rightarrow 0$ yields a non-zero response between $\frac{1}{2}\sqrt{2}$ and 1. Therefore, we have not applied these scaling arguments to μ , although we have allowed it to vary with height instead of assuming a constant aspect ratio of N / f , as was assumed by Garcia (1987).

Although the agreement between our estimates of the thermal damping time and those of NR97 is quite good at higher levels, we found significantly shorter thermal damping times in the lower stratosphere and troposphere, where thermally dissipative processes other than radiative damping are important. This likely explains why our results lie on the very short end of the broad range of tropospheric radiative damping times found in the literature. Overall, the results suggest that Garcia’s model for the frequency-dependent response of the zonal-mean flow to wave forcing is applicable to NH midlatitude wintertime conditions.

3

Interannual variability of the stratospheric wave driving during northern winter[‡]

Abstract

The strength of the stratospheric wave driving during northern winter is often quantified by the January-February mean poleward eddy heat flux at 100 hPa, averaged over 40°-80°N (or a similar area and period). Despite the dynamical and chemical relevance of the wave driving, the causes for its variability are still not well understood. In this study, 24 years of ERA-40 reanalysis data are used to examine several factors that significantly affect the interannual variability of the wave driving. The total poleward heat flux at 100 hPa is poorly correlated with that in the troposphere, suggesting a decoupling between 100 hPa and the troposphere. However, the individual zonal wave-1 and wave-2 contributions to the wave driving at 100 hPa do exhibit a significant coupling with the troposphere, predominantly due to their stationary components. The stationary wave-1 contribution to the total wave driving significantly depends on the latitude of the stationary wave-1 source in the troposphere. The results suggest that this dependence is associated with the varying ability of stationary wave-1 activity to enter the tropospheric waveguide at mid-latitudes. Alternatively, another approach is taken, in which the wave driving anomalies are separated into three parts: one part due to anomalies in the zonal correlation coefficient between the eddy temperature and eddy meridional wind, another part due to anomalies in the zonal eddy temperature amplitude, and a third part due to anomalies in the zonal eddy meridional wind amplitude. It is found that year-to-year variability in the zonal correlation coefficient between the eddy temperature and the eddy meridional wind is the most dominant factor in explaining the year-to-year variability of the poleward eddy heat flux.

[‡] This Chapter is a slightly revised version of: Haklander, A. J., P. C. Siegmund, and H. M. Kelder: Interannual variability of the stratospheric wave driving during northern winter, *Atmos. Chem. Phys.*, 7, 2575–2584, 2007.

3.1 Introduction

According to the downward-control principle, the stratospheric residual meridional circulation at any level is controlled by the vertically-integrated zonal force due to breaking Rossby and gravity waves above that level (Haynes et al. 1991). The breaking waves deposit westward angular momentum into the relative and planetary angular momentum ‘reservoirs’, causing a westward acceleration and a poleward displacement of the air (e.g., Andrews et al. 1987). In the low-frequency limit, the westward acceleration is zero and the meridional circulation is referred to as the Brewer-Dobson circulation (e.g., Shepherd 2000). The term ‘downward control’ can, however, be somewhat misleading, since it is predominantly the wave activity emanating from below that determines the amount of angular momentum deposited aloft.

The net zonal-mean upward flux of wave activity is represented by the upward component F_z of the Eliassen-Palm (EP) flux, which for quasigeostrophic flow is proportional to the zonal-mean poleward eddy heat flux $[\overline{v'T^*}]$, where the square brackets denote the zonal average and the asterisk denotes the deviation thereof (e.g. Andrews et al. 1987; Newman and Nash 2000). In the lower stratosphere, $[\overline{v'T^*}]$ (and therefore F_z) exhibits a strong, positive correlation with the tendency of total ozone at mid- and high latitudes during northern winter (e.g., Fusco and Salby 1999; Randel et al. 2002). Also, during late northern winter the midlatitude eddy heat flux in the lower stratosphere is highly and positively correlated with the temperature in early March at high latitudes, and consequently with the strength of the polar vortex (e.g., Newman et al. 2001; Polvani and Waugh 2004). Both observations can be explained by the wave-induced poleward transport of ozone-rich air from the tropical source and the subsequent adiabatic compression at higher latitudes.

This fundamental link between the poleward eddy heat flux and the dynamics and chemistry of the stratosphere is now well understood and also quantitatively employed as a diagnostic to validate coupled chemistry-climate models (CCMs) (Austin et al. 2003; Eyring et al. 2005). Austin et al. used the $[\overline{v'T^*}]$ field at 100 hPa averaged for January-February over 40°-80°N, hereafter referred to as H_{100} , as a measure of the net upward flux of midwinter wave activity in the lower stratosphere. They evaluated several CCMs

with respect to H_{100} , the polar stratospheric temperatures in early spring, and the (almost linear) relationship between both diagnostics. Since almost all of the planetary wave activity crosses the 100-hPa level between 40°-80°N (Hu and Tung 2003), H_{100} indeed provides a good measure of the net total wave activity propagating into the stratosphere. Several studies have been performed to analyze trends in H_{100} (or a similar diagnostic) over the last decades, and to predict future trends. Hu and Tung (2003) found a significant downward trend over 1979-2002 for $[v^*T^*]$ at 100 hPa, averaged over 50°-90°N and January to March. Austin et al. (2003) compared future H_{100} trends in a number of enhanced-CO₂ climate simulations, and found for most models a slightly negative trend over the next few decades, although at best of marginal statistical significance. One of the models showed a highly significant positive trend. For a doubled CO₂ climate, Sigmond et al. (2004) computed a significant increase of the Northern Hemisphere (NH) stratospheric residual circulation during winter, corresponding to an increase of the poleward eddy heat flux. These examples illustrate that future predictions of H_{100} are very uncertain. However, in a recent multi-model study by Butchart et al. (2006), increasing greenhouse gas concentrations were found to yield an overall strengthening of the Brewer-Dobson circulation and the associated wave driving, with the strongest trend in NH winter. Butchart et al. conclude that it remains an important future task to identify the causes of the increase in wave driving. Thus, despite the fact that it is widely acknowledged that the stratospheric wave driving has a large impact on the dynamics and chemistry of the stratosphere, the causes for its trends and variability are still not well understood.

In the present study, H_{100} is used as a measure of the net total midwinter wave activity that propagates from the troposphere into the stratosphere, following Austin et al. (2003), and Eyring et al. (2005). Our analysis puts the emphasis on the *interannual variability* of H_{100} , in order to obtain a better understanding of the causes of this observed variability, at both the interannual and the decadal timescale. Year-to-year variations in H_{100} can be attributed to many factors. The strength of the tropospheric wave source is an obvious factor, but also the shape of the source spectrum determines

the amount of wave activity that reaches 100 hPa, as is described by the Charney-Drazin criterion (Charney and Drazin 1961). This criterion states that stationary planetary waves can only propagate upward in a westerly zonal-mean flow that is not too strong. Only the longest waves can propagate through stronger westerlies, which implies that during winter only the longest waves can propagate into the stratosphere. The background zonal-mean flow determines the properties of this low-pass filter, and therefore also affects the interannual variability of H_{100} . The main goal of the present study is to investigate to what extent the year-to-year variability in H_{100} is affected by several factors. The factors that are examined include the strength of the total upward wave activity flux in the troposphere, the shape of the wave activity spectrum, the latitude and height of the wave source, and the refractive properties of the background flow. It is also examined whether the zonal correlation coefficient between the meridional wind and the temperature has a significant effect on the interannual variability of H_{100} . Our analysis is based on ERA-40 reanalysis data for the period of 1979-2002. In section 3.3, estimated values are often presented along with an error bar. These represent the associated standard deviations.

The structure of the paper is as follows. Section 3.2 gives a description of the data sources and discusses various ways of decomposing the poleward eddy heat flux. The main results are given in section 3.3, and a summary and discussion of the results is presented in section 3.4.

3.2 Data and method

3.2.1 Data

We use 6-hourly temperature and horizontal wind fields for 24 years (1979-2002) of ERA-40 reanalysis data (Simmons and Gibson 2000). Although the ERA-40 dataset starts in 1957, we have only included the satellite era, from 1979 onwards, in our analysis. For this period, the global observation data coverage is considered to be good (Uppala et al. 2005).

3.2.2 Linear regression analysis

The total poleward eddy heat flux can be decomposed into the sum of several components, such as the stationary and transient wave components. The impact of each component on the interannual variability of the total heat flux can be evaluated by performing a linear regression analysis. This can be understood as follows. It can easily be shown that if $y \equiv \sum x_i$, then the variance of y equals the sum of the covariances between y and the x_i , i.e., $\text{var}(y) = \sum \text{cov}(x_i, y)$. Thus, $\text{cov}(x_i, y)$ can be interpreted as the contribution of x_i to $\text{var}(y)$. If we define $b_i \equiv \text{cov}(x_i, y) \text{var}^{-1}(y)$, where $\sum b_i = 1$, then b_i is the regression coefficient for the linear least-squares fit given by $\tilde{x}_i = a_i + b_i y$. It should be noted that the correlation coefficient r_i between y and x_i can be large, while the associated value of b_i is small. For this reason, it is useful to consider both b_i and r_i . In the present study, y represents the total heat flux and the x_i represent the various components of the total heat flux (see section 3.2.3). Hereafter the phrase ‘a linear regression of v_1 with v_2 is performed’ implies that v_1 is the independent and v_2 is the dependent variable.

3.2.3 Decompositions of the heat flux

The total poleward eddy heat flux, averaged over space and time, can be decomposed by separating the eddy meridional wind and eddy temperature into a stationary and a transient part. If we denote the temporal average over January and February by an overbar, the deviation thereof by a prime, and the cosine-latitude weighted spatial average between 40°-80°N by angle brackets, we can write H at a certain pressure level as

$$H \equiv \overline{\langle v^* T^* \rangle} = \overline{\langle \bar{v}^* \bar{T}^* \rangle} + \overline{\langle v'^* T'^* \rangle}, \quad (3.1)$$

where H at 100 hPa was previously denoted by H_{100} . The asterisk denotes the deviation from the zonal mean. The r.h.s. terms of Equation (3.1) thus describe the contribution to H by the stationary and transient eddies, respectively.

In addition to the temporal decomposition in Equation (3.1), a spatial decomposition can be made by discriminating between the individual zonal wavenumber components of the heat flux. The zonal wave component of the total eddy heat flux is calculated as the product of the wave components of v and T , v_s and T_s (e.g., Newman and Nash 2000). This yields

$$H = \sum_{s \geq 1} \langle \overline{v_s T_s} \rangle, \quad (3.2)$$

where the subscript s denotes the zonal wave- s component. Combining Equations (3.1) and (3.2) yields

$$H = \sum_{s \geq 1} \langle \bar{v}_s \bar{T}_s \rangle + \sum_{s \geq 1} \langle \overline{v_s' T_s'} \rangle. \quad (3.3)$$

The impact of these individual stationary and transient wave components on the interannual variability of the total heat flux will be evaluated by a linear regression analysis in the next section.

A different way of decomposing the total eddy heat flux, is by noting that $[v^* T^*]$ can be expressed as

$$[v^* T^*] = r_{v,T} \sigma_v \sigma_T, \quad (3.4a)$$

where $r_{v,T}$ is the zonal correlation coefficient, and σ_v and σ_T are the zonal standard deviations of v and T . If v or T would consist of only one wave component, then their wave amplitudes would be given by $\sqrt{2}\sigma_v$ and $\sqrt{2}\sigma_T$, respectively, and $r_{v,T}$ would be equal to $\cos \Delta\varphi$, where $\Delta\varphi$ is the phase difference between the v and the T wave

patterns. Therefore, $r_{v,T}$ might be considered as the cosine of the ‘effective phase difference’ between v and T for the total spectrum of waves, with $\sqrt{2}\sigma_v$ and $\sqrt{2}\sigma_T$ representing the effective v and T amplitudes, respectively. The larger $r_{v,T}$, the smaller the effective phase difference between the v and T fields, and the more efficiently heat is transported poleward by the waves. To investigate both the qualitative and the quantitative effects of year-to-year variations in $r_{v,T}$, σ_v , and σ_T on the interannual variability of H_{100} , we use the following approach (e.g., Siegmund 1995). First, we rewrite the average of Equation (3.4a) over 40°-80°N and January-February as follows:

$$H \equiv \overline{r_{v,T} \sigma_v \sigma_T} \approx \overline{r_{v,T}} \overline{\sigma_v} \overline{\sigma_T} + \tilde{E} \equiv \tilde{H} + \tilde{E}, \quad (3.4b)$$

where \tilde{E} denotes the error that is introduced by neglecting the zonal and temporal cross-correlations between $r_{v,T}$, σ_v , and σ_T . The validity of the approximation $H_{100} \approx \tilde{H}_{100}$ will be discussed in section 3.4. Dropping the angular brackets and the overbars, denoting the 24-year mean by a superscript m and the deviation thereof by a Δ , $\Delta\tilde{H}$ can be linearized as:

$$\Delta\tilde{H} \equiv \Delta\hat{H} + \Delta\hat{E} \equiv \sigma_v^m \sigma_T^m \Delta r_{v,T} + \sigma_T^m r_{v,T}^m \Delta\sigma_v + \sigma_v^m r_{v,T}^m \Delta\sigma_T + \Delta\hat{E}, \quad (3.4c)$$

where $\Delta\hat{E}$ denotes the error that arises from the linearization. If Equations (3.4b) and (3.4c) are combined, we obtain

$$\Delta H \equiv \sigma_v^m \sigma_T^m \Delta r_{v,T} + \sigma_T^m r_{v,T}^m \Delta\sigma_v + \sigma_v^m r_{v,T}^m \Delta\sigma_T + \Delta\hat{E} + \Delta\tilde{E}. \quad (3.4d)$$

Equation (3.4d) will be used to analyze the contribution to the interannual variability of H_{100} by the interannual variabilities of $r_{v,T}$, σ_v , and σ_T .

3.3 Results

3.3.1 Timeseries of H_{100}

The 24-year timeseries of H_{100} (1979-2002) is displayed as the thick solid line with filled circles in Figure 3.1. During this 24-year period, H_{100} ranged between 11.2 and 19.2 K m s^{-1} , and the average value of H_{100} was $15.1 \pm 0.5 \text{ K m s}^{-1}$. There is a slightly negative trend in H_{100} , but the trend is not statistically significant (93.2% confidence level). Hu and Tung (2003) did find a highly significant downward trend over 1979-2002 in the vertical EP-flux component north of 50°N for the January-March

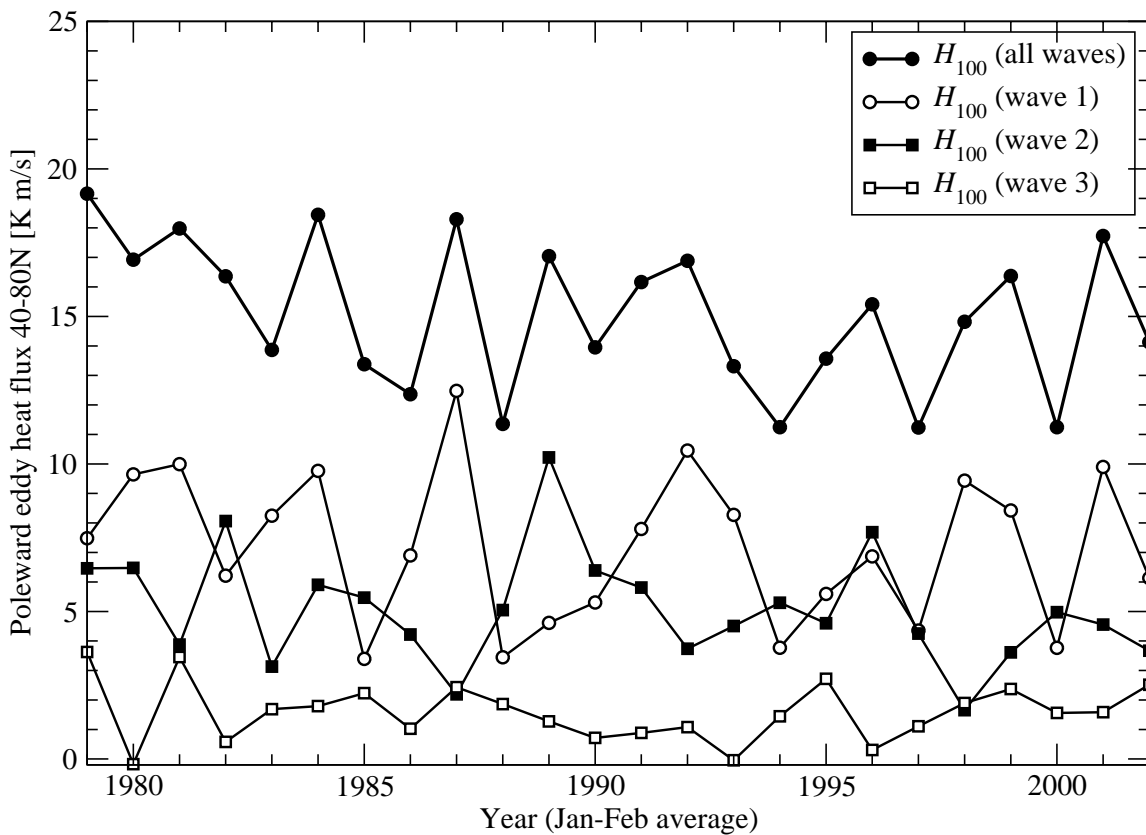


Figure 3.1: Poleward eddy heat flux at 100 hPa, averaged over $40^\circ\text{-}80^\circ\text{N}$ and January-February, for the years 1979-2002. The sum of all wave contributions H_{100} is shown, as well as the separate wavenumber 1-3 components of H_{100} .

January-February period. If we regard H_{100} as the sum of its zonal wave- s components as expressed by Equation (3.2), we find that the $s = 1-3$ components of H_{100} account for more than 90% of H_{100} . The first three wave components of H_{100} are also shown in Figure 3.1. Both the variance and the 24-year average decrease with increasing wavenumber. For the majority of the years, variations in H_{100} seem to be dominated by the wave-1 variations, indicated by the line with open circles in Figure 3.1. A relatively constant factor is that the wave-1 and wave-2 variations tend to be opposite. The correlation coefficient for the wave-1 and wave-2 components is $r = -0.42$, which is significant at a 95.8% confidence level. The separate $s = 1, 2,$ and 3 components of H_{100} all exhibit a slightly negative trend over 1979-2002, but the statistical significance of these trends is well below the 95% confidence level.

Table 3.1: Linear regression coefficients \pm their standard error, and correlation coefficients for the linear regression of H_{100} with its total, stationary and transient $s = 1-5$ components. The linear regression is performed over 1979-2002.

s	Regr. coeff. (b_i)			Corr. coeff. (r_i)		
	Tot $\pm \sigma$	Stat $\pm \sigma$	Tran $\pm \sigma$	Tot	Stat	Tran
1	0.74 \pm 0.15	0.56 \pm 0.23	0.18 \pm 0.14	0.73	0.47	0.26
2	0.12 \pm 0.16	0.06 \pm 0.16	0.06 \pm 0.08	0.16	0.08	0.15
3	0.09 \pm 0.08	0.02 \pm 0.08	0.08 \pm 0.05	0.24	0.05	0.30
4	0.00 \pm 0.03	-0.02 \pm 0.02	0.02 \pm 0.03	0.01	-0.19	0.13
5	0.00 \pm 0.02	0.00 \pm 0.00	-0.01 \pm 0.02	-0.04	0.23	-0.09
all	1	0.63 \pm 0.16	0.37 \pm 0.16	1	0.65	0.46

3.3.2 Wave contributions to interannual variability of H_{100}

To further examine the interannual variability of H_{100} , we decompose H_{100} into its stationary and transient wave components, as expressed by Equation (3.3). Taking H_{100} as the independent variable, the linear regression coefficient b_i for the regression of H_{100} with its stationary or transient wave component represents the relative contribution

by that wave component to the total variance of H_{100} , as discussed in section 3.2. Table 3.1 shows the regression coefficients and the corresponding correlation coefficients for the total (stationary plus transient), stationary, and transient wave 1-5 components of H_{100} . Using a Student's t -test, we find for a sample size of 24, that the correlation coefficient r_i is significantly different from zero at a $> 95\%$, 99% , or 99.9% confidence level if $|r_i| > 0.40$, 0.52 or 0.63 , respectively. The sum of the regression coefficients for the total wave 1-5 contribution to H_{100} is 0.95 ± 0.05 , with a corresponding correlation coefficient $r_i = 0.996$ (not shown). Therefore, wavenumbers 6 and higher can be neglected in the analysis of the interannual variability of H_{100} . In fact, almost all of the interannual variability of H_{100} is due to $s = 1-3$, with a combined regression coefficient of $b_i = 0.96 \pm 0.06$ and $r_i = 0.98$. Only retaining $s = 1,2$ yields $b_i = 0.86 \pm 0.11$ and $r_i = 0.88$. We can thus state that about 85% of the interannual variability of H_{100} can be attributed to its $s = 1,2$ components. When analyzing the interannual variability of H_{100} , it is sufficient to only consider wavenumbers $s = 1-3$, or perhaps even $s = 1,2$. The bottom row of Table 3.1 shows that the interannual variability of H_{100} is dominated by the stationary waves, with $b_i = 0.63 \pm 0.16$ and $r_i = 0.65$. However, the correlation coefficient of H_{100} with its transient component is also significant at the 97.6% confidence level.

3.3.3 Vertical coupling

As described in the introduction, H_{100} is proportional to the total net wave activity flux emanating from below between 40°N and 80°N at the 100-hPa level. Most of the planetary wave activity that constitutes H_{100} has propagated upward from its tropospheric source, and therefore, it is expected that H_{100} has a significant positive correlation coefficient with the poleward eddy heat flux at levels below (and above) 100 hPa. To verify this, we examine the amount of vertical coupling between 100 hPa and other levels. We do this by calculating the vertical profile of the correlation coefficient of H_{100} with $\langle \overline{v^*T^*} \rangle_{NH}$, which we define as the 20° - 90°N average of $[\overline{v^*T^*}]$, at levels from 1000 hPa to 1 hPa. Note that the area from 20° - 90°N is almost twice the area from

40°-80°N. We compute the correlation coefficient with $\langle \overline{v^*T^*} \rangle_{NH}$, since the wave activity flux contributing to H_{100} may have partially originated from, or may propagate into, latitudes outside the 40°-80°N band. The correlation coefficient profile is shown in Figure 3.2. At 100 hPa, H_{100} is highly correlated with $\langle \overline{v^*T^*} \rangle_{NH}$ ($r = 0.95$), suggesting that the 100-hPa wave activity outside the 40°-80°N area is relatively small. This is confirmed by the fact that H_{100} accounts for about 90% of $\langle \overline{v^*T^*} \rangle_{NH}$ at 100 hPa in the 1979-2002 period. Therefore, to simplify the interpretation of our results, we neglect the 100-hPa upward wave activity flux at latitudes outside the 40°-80°N window. In Figure 3.2, we see that the level of maximum correlation coefficient between H_{100} and

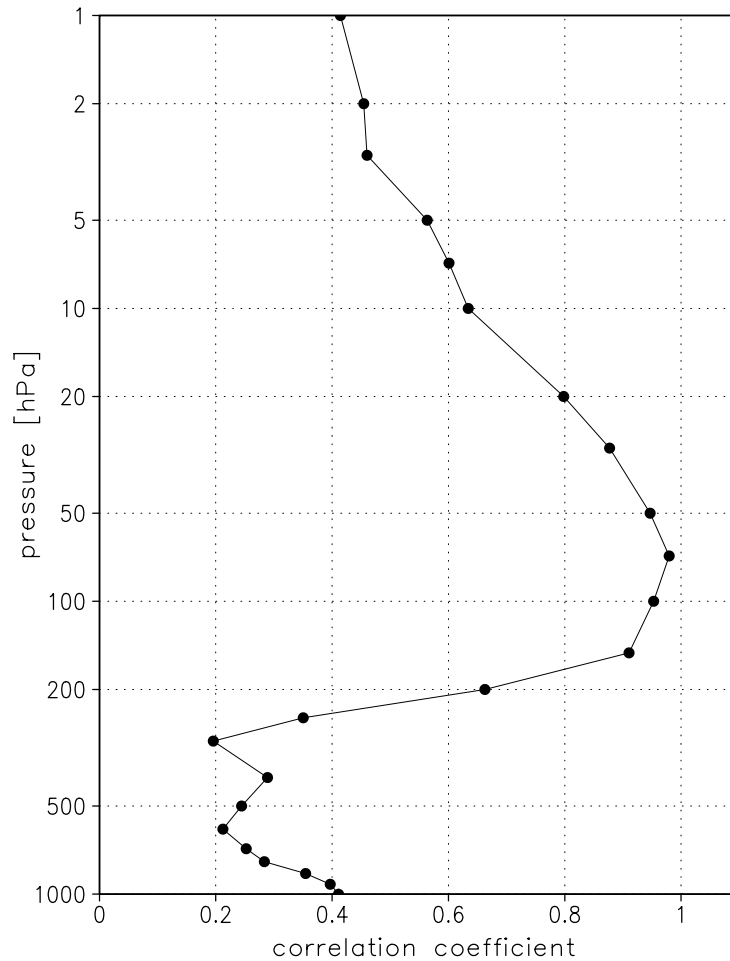


Figure 3.2: Correlation coefficients of H_{100} with $\langle \overline{v^*T^*} \rangle_{NH}$. Correlation coefficients are calculated over the years 1979-2002.

$\langle \overline{v^*T^*} \rangle_{NH}$ is found at 70 hPa rather than 100 hPa. Above 70 hPa, the correlation coefficient gradually decreases to marginally significant values near the stratopause ~ 1 hPa. Below 100 hPa, the correlation coefficient falls off quite rapidly, and is not significant ($|r| < 0.40$) below 200 hPa. Thus, there exists a decoupling between variations in the total upward flux of wave activity in the troposphere (below 200 hPa) and variations at 100 hPa. Assuming that the wave sources are predominantly located in the troposphere, this decoupling can be understood as follows. Suppose an amount of wave activity propagates upward in the NH at some tropospheric pressure level p during January-February. A fraction α_p of this wave activity is absorbed below 100 hPa, where α_p lies between 0 and 1. Assuming that no wave activity crosses the equator, the remaining fraction of the wave activity ($1 - \alpha_p$) thus reaches the 100-hPa level and contributes to H_{100} . If α_p is less than one and independent of time, then the correlation coefficient between H_{100} and the wave activity flux at pressure level p will be one. On the other hand, if α_p has a large interannual variability, the correlation coefficient will be small.

For a plane and conservative planetary wave, the zonal wavenumber s and the frequency remain constant along its path (or ‘ray’) in the meridional plane (e.g., Karoly and Hoskins 1982). Therefore, it makes sense to repeat the previous analysis for each individual zonal wave component. To examine the amount of vertical coupling as a function of zonal wavenumber (stationary plus transient), we compute the correlation coefficients of the wave- s component of H_{100} with the (same) wave- s component of $\langle \overline{v^*T^*} \rangle_{NH}$ at other levels. We perform this analysis for the individual wavenumbers 1 to 5 and 6+, separately. The results are shown in Figure 3.3a. The $s = 1$ component of $\langle \overline{v^*T^*} \rangle_{NH}$ is significantly correlated with the $s = 1$ component of H_{100} at 500 hPa, and at all levels above 400 hPa. The $s = 2$ component of $\langle \overline{v^*T^*} \rangle_{NH}$ exhibits a significant correlation with the $s = 2$ component of H_{100} throughout the troposphere and the stratosphere. Note that the wave-2 correlation coefficient reaches a minimum in the mid-troposphere but that the correlation coefficients for $s = 2$ are statistically significant at all

levels below 1 hPa. For waves with $s > 2$, the correlation coefficients generally only exceed the 95% significance level between 250 hPa and 50 hPa. Thus, the lack of correlation we saw in Figure 3.2 between the total upward flux of wave activity in the troposphere and that at 100 hPa is also observed for the $s > 2$ flux components, but not (entirely) for $s = 1,2$. This result implies that a significant part of the interannual variability in the $s = 1,2$ components of H_{100} is due to year-to-year variations in the strength of the $s = 1,2$ wave source in the troposphere. There is no significant correlation for the $s > 2$ flux components, since the refractive index for those waves exhibits a vertical layer of negative values in the lower stratosphere (Figure 3.5b). Therefore, meridional refraction and reflection of the $s > 2$ waves is taking place below 100 hPa, so that H_{100} is dominated by waves 1 and 2.

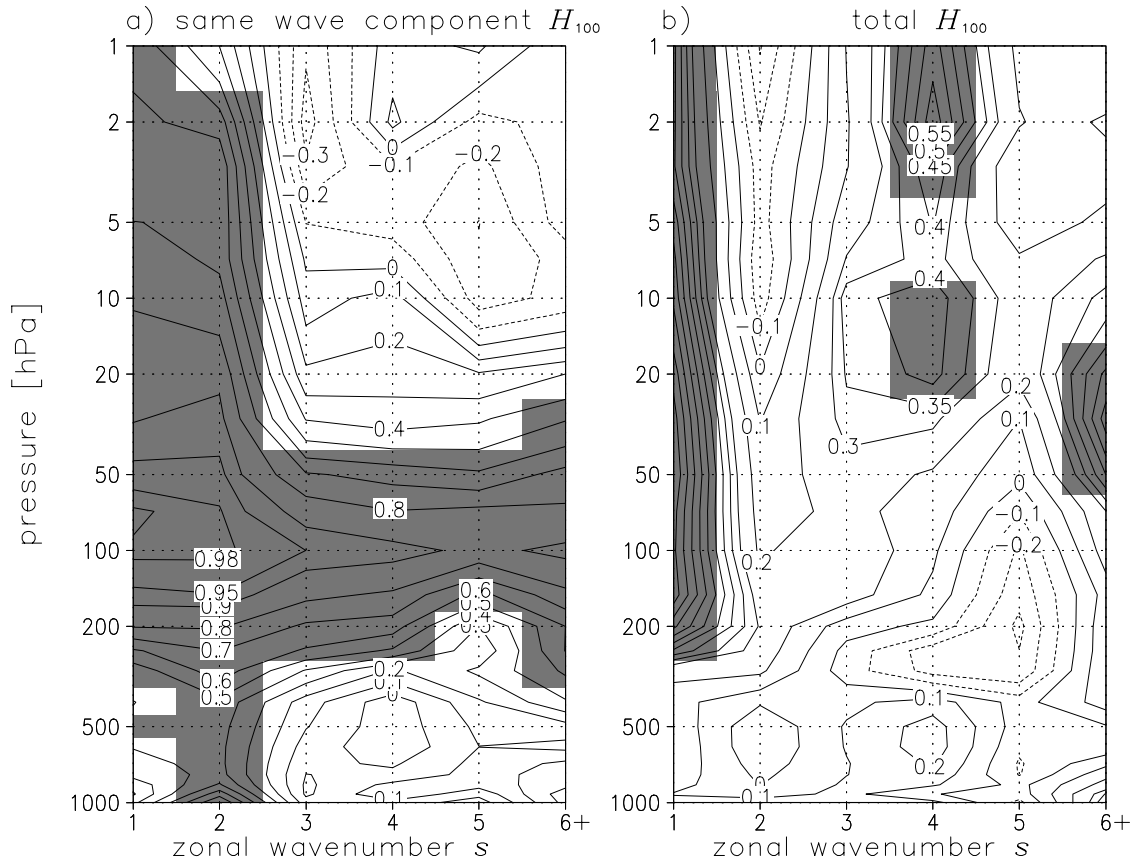


Figure 3.3: Correlation coefficients of **a)** the zonal wave- s component of H_{100} , and **b)** H_{100} , with the zonal wave- s component of $\overline{\langle v^*T^* \rangle_{NH}}$. Correlation coefficients are calculated over 1979-2002, and the areas with > 95% confidence levels are shaded.

We have just shown that the separate $s = 1,2$ components of H_{100} , to which about 85% of the interannual variability of H_{100} can be attributed, are significantly correlated with the separate $s = 1,2$ components of $\langle \overline{v^*T^*} \rangle_{NH}$ at some level in the lower or mid-troposphere. But to what extent can the interannual variability of the *total* H_{100} be attributed to year-to-year variations in the separate $s = 1$ and $s = 2$ components (or higher) of $\langle \overline{v^*T^*} \rangle_{NH}$ in the troposphere? To answer this question, we examine the correlation coefficient of H_{100} (i.e., the sum of all wave components) with the separate wave components of $\langle \overline{v^*T^*} \rangle_{NH}$. The results are shown in Figure 3.3b, where the wavenumber of the pressure-dependent $\langle \overline{v^*T^*} \rangle_{NH}$ component is given along the horizontal axis. At levels below 200 hPa, the $s = 1,2$ components of $\langle \overline{v^*T^*} \rangle_{NH}$ are not significantly correlated with H_{100} . In fact, none of the wave components is. However, in the upper stratosphere, the $s = 4$ component of $\langle \overline{v^*T^*} \rangle_{NH}$ exhibits a remarkably strong correlation with H_{100} . It is interesting to compare Figures 3.3a and 3.3b. We observe in Figure 3.3a that the wave-4 component of $\langle \overline{v^*T^*} \rangle_{NH}$ in the upper stratosphere is not at all correlated with the wave-4 component of H_{100} . However, Figure 3.3b shows that the correlation coefficient with the *total* H_{100} is highly significant for the wave-4 component of $\langle \overline{v^*T^*} \rangle_{NH}$ in the upper stratosphere ($r = 0.58$ at 2 hPa, 99.7% confidence level). The results suggest that wavenumber 4 is a preferred mode for the breaking of very long planetary waves in the upper stratosphere.

3.3.4 Correlation patterns in the meridional plane

Thusfar, we have only considered averages over 40° - 80° N and averages over the Northern Hemisphere north of 20° N. In the previous subsection we mentioned that α_p also depends on the latitude at which the waves propagate upward. Therefore, we next examine where the *zonal-mean* upward wave-activity flux, which is proportional to $[\overline{v^*T^*}]$, is significantly correlated with H_{100} . The latitude- and pressure-dependent

correlation coefficient of H_{100} with $\overline{[v^*T^]}$ is shown in Figure 3.4a. The highest correlation coefficient is found at 100 hPa and 62.5°N ($r = 0.87$). The decoupling between the total upward wave-activity flux at 100 hPa and that in the troposphere (Figure 3.2) is also visible in Figure 3.4a: H_{100} is not significantly correlated with $\overline{[v^*T^]}$ in the lower and middle troposphere. We previously saw that the $s = 1,2$ components of H_{100} significantly correlate with the same wave- s components of $\langle \overline{v^*T^} \rangle_{NH}$ at some level in the mid- and lower troposphere.

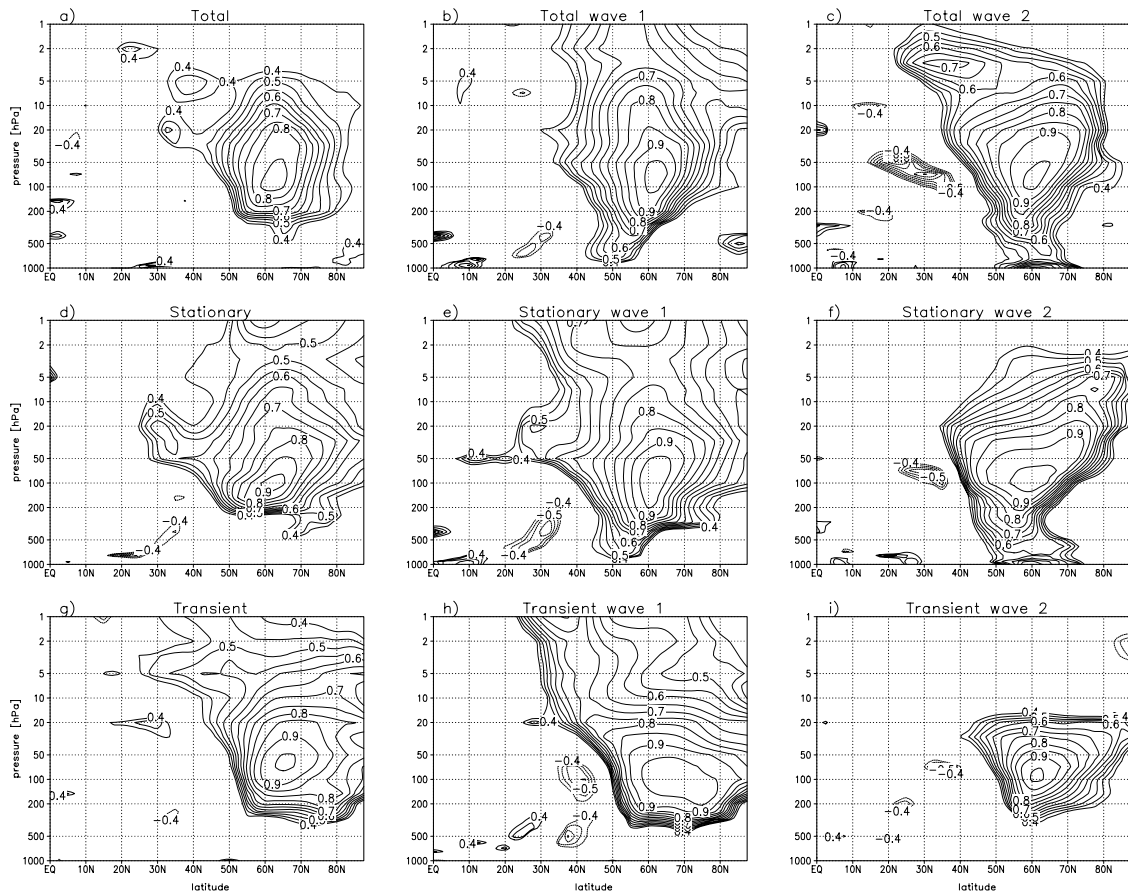


Figure 3.4: Correlation coefficient of (a) H_{100} , (b,c) the $s = 1,2$ component of H_{100} , (d) the stationary component of H_{100} , (e,f) the stationary $s = 1,2$ component of H_{100} , (g) the transient component of H_{100} , (h,i) the transient $s = 1,2$ component of H_{100} ; with the same latitude- and pressure-dependent wave component of the zonal-mean eddy heat flux averaged over January-February. Correlation coefficients are calculated over 1979-2002, and only the areas with $> 95\%$ confidence levels are shown.

Figure 3.4b shows that the wave-1 component of H_{100} is significantly correlated with the wave-1 component of $[\overline{v^*T^*}]$ in the troposphere, between about 40°N and 60°N. Note that the meridionally confined correlation coefficient maximum in the troposphere tilts poleward with height. A possible explanation for this correlation coefficient maximum would be the presence of a waveguide, through which the wave-1 activity is ducted to 100 hPa (e.g., Karoly and Hoskins 1982). Since a waveguide can be identified as a ridge in the refractive index field, we verify this by computing the climatological January-February pattern of the refractive index squared for $s = 1$, which is shown in Figure 3.5a. The wave-1 correlation coefficient maximum is roughly denoted by the dashed line. We see that the refractive index indeed has a ridge in the mid-latitude middle and upper troposphere, which suggests that the tropospheric correlation coefficient maximum in Figure 3.4b may be regarded as the signature of this tropospheric wave guide. To illustrate how the upper troposphere and lower stratosphere act as a low-pass filter for planetary wave activity from below, we show the refractive index field for $s = 3$ in Figure 3.5b. A mid-latitude vertical layer with negative values in the lower stratosphere emerges, of which the vertical extent increases with increasing wavenumber (not shown). For wavenumber 2 (Figure 3.4c), a connection with the (lower) troposphere is found that is similar to that of wavenumber 1. A marked difference between Figures 3.4c and 3.4b is, that the area of maximum correlation coefficients in the troposphere is found at higher latitudes (50-70°N) in Figure 3.4c. (The distinct and very high maximum of $r = 0.82$ at 1000 hPa may not be very meaningful due to the extrapolation below ground.) This correlation coefficient maximum cannot be linked to an $s = 2$ waveguide, since the refractive index field in this region is highly variable due to the presence of a zero-wind critical line, which is not sensitive to the zonal wave number of the refractive index. For wavenumber 2, the latitude of maximum correlation coefficients shifts equatorward with height above 100 hPa. For the wave-3 contribution to the heat flux, the link with the troposphere is absent and the area with significant correlation coefficients is much more confined (not shown). A further decomposition into stationary and transient wave components (Figures 3.4d-i) reveals that the link with the (lower) troposphere is only statistically significant for the *stationary* part of the wave-1 and wave-2 contributions.

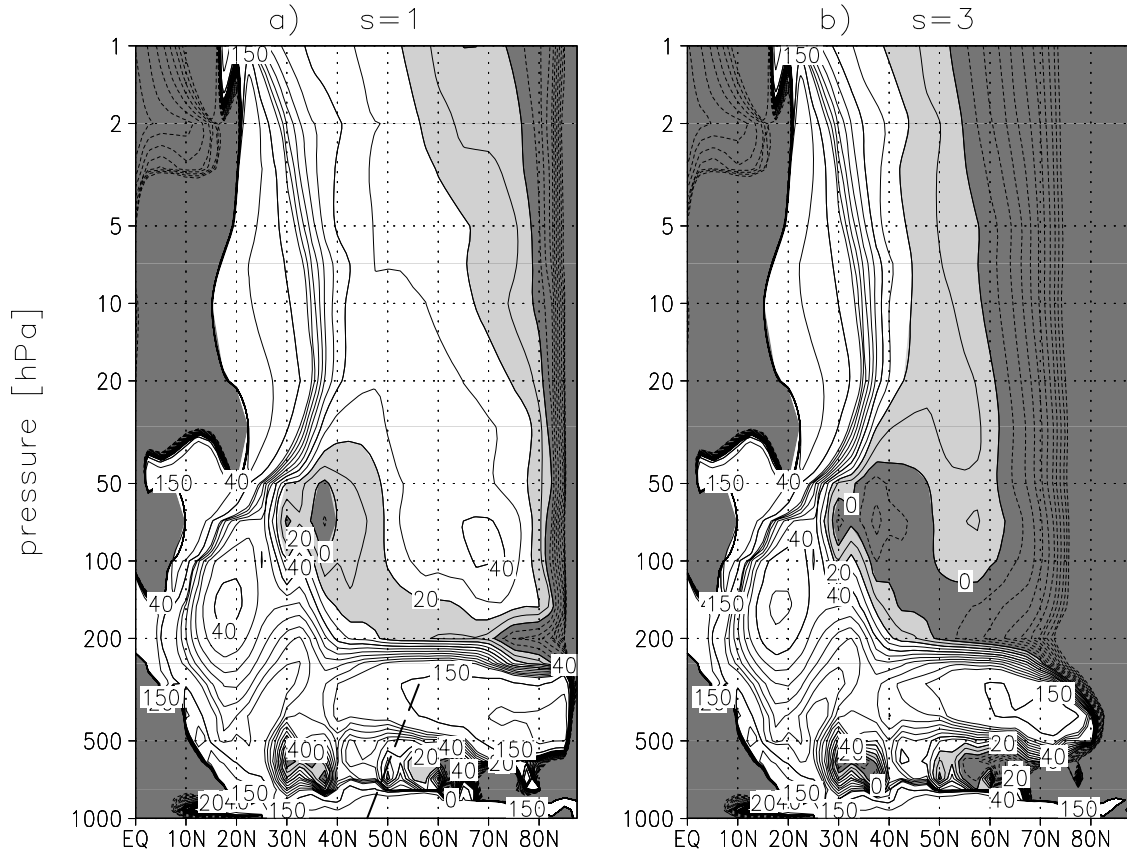


Figure 3.5: Refractive index square $a^2 n_s^2$ in m^2 , based on the 1979-2002 average of the zonal-mean zonal wind during January-February, for a) $s = 1$, and b) $s = 3$. Except for the 150 and 300 m^2 contours, contours are from -100 to 100 m^2 , with an interval of 10 m^2 . Negative values are indicated by dark shading, positive values below 20 m^2 by light shading. The 0, 20, 40, and 150 m^2 contours have been labeled, and the location of the $s = 1$ correlation coefficient maximum is roughly denoted by the dashed line in a).

To interpret the negative correlation coefficients in Figure 3.4e around 32.5°N at 400 hPa, we computed the correlation coefficient at 400 hPa for the stationary wave-1 fluxes at 32.5°N and 57.5°N , where the positive correlation maximum was observed. A strong anti-correlation was found ($r = -0.52$, 99% confidence level). Thus, the tropospheric meridional dipole structure in the stationary wave-1 correlation coefficient map likely implies that the stationary wave-1 component of H_{100} is sensitive to the latitude of the tropospheric wave-1 source. If the source is located too far south, less wave activity is

able to enter the mid-latitude waveguide and contribute to H_{100} . Such a dipole structure is not found in Figure 3.4f for $s = 2$.

3.3.5 An alternative analysis of the interannual variability of H_{100}

In section 3.2.3, we mentioned an alternative way of decomposing H_{100} , by noting that $[v^*T^*]$ equals the product of $r_{v,T}$ with σ_v and σ_T (Equation (3.4a)). Subsequently, we assumed in Equation (4b) that H_{100} can be approximated by \tilde{H}_{100} . To examine the accuracy of this approximation, we first compare the 24-year averages of both \tilde{H}_{100} and H_{100} . This yields $14.1 \pm 0.4 \text{ K m s}^{-1}$ and $15.1 \pm 0.5 \text{ K m s}^{-1}$, respectively, with a mean ratio of 0.94 ± 0.2 . To see if \tilde{H}_{100} and H_{100} also have comparable interannual variability, we performed a linear regression of H_{100} with \tilde{H}_{100} . The regression yields a high correlation coefficient ($r = 0.85$) and a regression coefficient $b = 0.71 \pm 0.09$. We conclude that \tilde{H}_{100} is indeed a useful approximation of H_{100} . We next linearize the deviation of \tilde{H}_{100} from its 1979-2002 mean as $\Delta\hat{H}_{100}$ (Equation (3.4c)). The error $\Delta\hat{E}_{100}$ that arises from the linearization in Equation (3.4c) is remarkably small: a linear regression of $\Delta\tilde{H}_{100}$ with $\Delta\hat{H}_{100}$ yields $b = 0.98 \pm 0.03$ and $r = 0.99$. The difference between ΔH_{100} and $\Delta\hat{H}_{100}$ in Equation (3.4d) thus primarily results from $\Delta\tilde{E}_{100}$. We can use Equation (3.4d) to analyze the sensitivity of H_{100} to the year-to-year variations in the effective phase difference $\langle \overline{r_{v,T}} \rangle$, as well as to the interannual variability of the effective amplitudes $\langle \overline{\sigma_v} \rangle$ and $\langle \overline{\sigma_T} \rangle$. The regression and correlation coefficients of the linear regression analysis of H_{100} with the first three terms on the r.h.s. of Equation (3.4c) at 100 hPa are given in Table 3.2. The results show that the interannual variability of H_{100} is more sensitive to the $\langle \overline{r_{v,T}} \rangle$ than to $\langle \overline{\sigma_v} \rangle$ and $\langle \overline{\sigma_T} \rangle$. Therefore, a significant part of the year-to-year variability in H_{100} is not determined by variability in the amplitude of the waves but by variability in the efficiency of the poleward heat

Table 3.2: Linear regression of H_{100} with $\sigma_v^m \sigma_T^m \Delta r_{v,T}$, $\sigma_T^m r_{v,T}^m \Delta \sigma_v$, and $\sigma_v^m r_{v,T}^m \Delta \sigma_T$ at 100 hPa. The linear regression is performed over 1979-2002. The 1979-2002 averages and standard deviations are for $\langle \overline{r_{v,T}} \rangle$, $\langle \overline{\sigma_v} \rangle$, and $\langle \overline{\sigma_T} \rangle$, respectively.

	Regression coefficient	Corr. coefficient	1979-2002 average	1979-2002 stdev
$\sigma_v^m \sigma_T^m \Delta r_{v,T}$	0.40 ± 0.20	0.39	$r_{v,T}^m = 0.23$	0.04
$\sigma_T^m r_{v,T}^m \Delta \sigma_v$	0.07 ± 0.09	0.17	$\sigma_v^m = 10.4 \text{ m s}^{-1}$	0.8 m s^{-1}
$\sigma_v^m r_{v,T}^m \Delta \sigma_T$	0.23 ± 0.14	0.34	$\sigma_T^m = 5.9 \text{ K}$	0.7 K

transport, as represented by $\langle \overline{r_{v,T}} \rangle$. We also note that the variability in $\langle \overline{\sigma_T} \rangle$ affects H_{100} more strongly than the variability in $\langle \overline{\sigma_v} \rangle$.

3.4 Summary and discussion

We have studied the interannual variability of the stratospheric wave driving during NH winter, as quantified by H_{100} , being the January-February mean of the 40°-80°N average of the total poleward heat flux at 100 hPa. For our analysis, we used 24 years (1979-2002) of ERA-40 reanalysis data from ECMWF. The results can be summarized as follows. We have examined the sensitivity of H_{100} to several factors. The first factor is the strength of the total tropospheric wave source. It was found that H_{100} is not significantly correlated with the total upward wave activity flux below 200 hPa. However, both the individual zonal wave-1 and wave-2 components exhibit significant vertical coupling between 100 hPa and lower (as well as higher) levels. About 85% of the interannual variability of H_{100} can be attributed to its $s = 1, 2$ components. However, the interannual variability of H_{100} cannot be attributed to either of these individual wave components of the heat flux in the troposphere. Presumably, this is in part due to the statistically significant negative correlation coefficient that we found between the $s = 1$ and $s = 2$ components of H_{100} . This negative correlation coefficient is also observed on

an intraseasonal timescale, in association with the leading mode of variability in the NH winter geopotential field, the Northern Annular Mode (NAM) (Hartmann et al. 2000). During high NAM index periods, with a stronger stratospheric polar vortex, the anomalous $s = 1$ component of the heat flux at 100 hPa was negative, and the anomalous $s = 2$ component was positive. During low NAM index periods, both anomalies were of opposite sign. Thus, the negative correlation coefficient we found on the interannual timescale is also observed on the shorter timescales. The wave-1 contribution to H_{100} was found to depend on the latitude of the wave-1 source. Particularly, if the tropospheric stationary wave-1 source is located near 30°N instead of near 50°N , significantly less wave activity is able to enter the mid-latitude waveguide and contribute to H_{100} .

Finally, another approach was followed, where the wave driving anomalies were separated into three parts: one part due to anomalies in the zonal correlation coefficient between the eddy temperature and eddy meridional wind, another part due to anomalies in the zonal eddy temperature amplitude, and a third part due to anomalies in the zonal eddy meridional wind amplitude. It was found that year-to-year variability in the zonal correlation coefficient between the eddy temperature and the eddy meridional wind is the most dominant of the three factors.

In the interpretation of our results, the assumption has been that wave activity always propagates upward, so that the source of the wave activity at 100 hPa is situated below 100 hPa. For stationary waves, this is a reasonable assumption. However, transient waves can develop in the stratosphere as a result of purely stationary waves of sufficient amplitude emanating from the troposphere, as demonstrated by Christiansen (1999). Downward propagation of these stratospheric transients might affect H_{100} . However, we expect this to be only a minor influence, since the interannual variability of H_{100} is dominated by stationary waves (Table 3.1), and transient wave activity is abundantly generated in the troposphere.

In the present study, the 1958-1978 period was omitted from the analysis. However, we have also analyzed the entire 1958-2002 period. The results were very similar, although the statistical significance was generally larger due to the longer period. As a result, Figure 3.3a exhibited a significant correlation coefficient for $s = 1$ in the

entire free troposphere. A remarkable difference with the 1979-2002 analysis was found for Figure 3.3b, in which the level of maximum and significant correlation coefficient with H_{100} was found to increase with increasing wavenumber $s = 1-5$. The $s = 1$ correlation coefficient decreased to statistically insignificant values of less than 0.3 in the upper stratosphere. In Figure 3.4a, a clear equatorward displacement of a statistically significant correlation coefficient maximum was observed above 100 hPa, and in Figure 3.4e, the tropospheric dipole structure for $s = 1$ in Figure 3.4e was more pronounced. Finally, for the 1958-2002 period, a significantly higher refractive index was observed in the mid-latitude stratosphere for a composite with positive H_{100} anomalies exceeding one standard deviation than for a composite of negative H_{100} anomalies exceeding one standard deviation. Such a significant signal could not be obtained for the 1979-2002 period, likely due to the smaller sample size.

One could argue that the results depend on the 40°-80°N latitude window that is applied. However, replacing H_{100} with the NH average of $[\overline{v^*T^*}]$ at 100 hPa yields almost identical results. The present study has focused on the interannual variability of the stratospheric wave driving. We note that the factors that dominate the interannual variability may be different from the factors that dominate the trend. These issues will be subject of our further investigation.

Acknowledgements

The authors gratefully acknowledge the constructive suggestions that were made by the editor and three anonymous referees.

4

How does the northern-winter wave driving of the Brewer-Dobson circulation increase in an enhanced-CO₂ climate simulation? §

Abstract

Recent climate studies show that the northern-winter wave driving of the Brewer-Dobson circulation is enhanced if greenhouse gas concentrations increase. An explanation for this enhancement does not yet exist. In this study, the enhanced wave driving, as simulated in a doubled-CO₂ experiment with the MA-ECHAM4 climate model, is analyzed in detail. The extratropical poleward eddy heat flux increases (decreases) in the stratosphere (troposphere) mainly due to the stationary (transient) heat-flux component. The heat flux at 100 hPa is a measure of the stratospheric wave driving, and is found to increase by 12% in the doubled-CO₂ climate. This increase is dominated by the stationary-wave 1 heat flux, which is also enhanced in the midlatitude troposphere. The heat flux increase at 100 hPa is almost entirely due to an increase in the longitudinal temperature variability. The latter increase is mainly due to the well-understood sharpening of the lower-stratospheric meridional temperature gradient.

§ This Chapter is a slightly revised version of: Haklander, A. J., P. C. Siegmund, M. Sigmund, and H. M. Kelder: How does the northern-winter wave driving of the Brewer-Dobson circulation increase in an enhanced-CO₂ climate simulation?, *Geophys. Res. Lett.*, doi:10.1029/2007GL033054, 2008.

4.1 Introduction

Global-mean CO₂ concentrations have risen by about 10% in the 1979-2002 period, but a structural trend in the planetary-wave driving of the Brewer-Dobson circulation (BDC) is not yet observed during northern winter, likely due to a low signal-to-noise ratio over this relatively short period (e.g., Haklander et al. 2007). However, Butchart et al. (2006) recently found that a more substantial increase of greenhouse gas (GHG) concentrations yields an overall strengthening of the BDC and the associated upward propagation of planetary-wave activity, with the strongest trend during northern winter. They found this result by comparing the response of the BDC to increasing GHG concentrations in an ensemble of general circulation models (GCM), with some models including interactive chemistry. The causes and nature of the strengthening are not yet clear. Shindell et al. (1999) suggested that increased GHG concentrations enhance the subtropical jet, so that more tropospheric planetary-wave activity at midlatitudes propagates into the stratosphere, thereby strengthening the BDC. The physical explanation of this was, that near 200 hPa, the meridional temperature gradient increases due to lower-stratospheric cooling on the poleward side and upper-tropospheric warming on the equatorward side of the subtropical jet. The associated increase of the thermal wind would enhance the subtropical jet, causing a decrease in the equatorward refraction of tropospheric wave activity at midlatitudes. Eichelberger and Hartmann (2005) studied the qualitative effect of increasing GHG concentrations on the BDC by imposing a tropical tropospheric heat source in their GCM. This dry hydrostatic GCM had a flat lower boundary, and therefore did not simulate stationary waves at all. It was found that the BDC strengthens in response to the imposed tropospheric tropical heating, with an increase in upward propagation of transient wave-2 and wave-5 activity in the troposphere. However, only the transient wave-2 increase extended upward into the stratosphere.

Sigmond et al. (2004) compared the BDC in a control climate and a doubled-CO₂ climate simulation. The BDC was found to be significantly stronger in the doubled-CO₂ run. Although the vertical component of the Eliassen-Palm (EP) flux increased in the midlatitude lower stratosphere, a decrease was found in the midlatitude troposphere.

Sigmond et al. (2004) concluded that this might be caused either by a higher transparency of the NH midlatitude tropopause for tropospheric wave activity, or by more generation of wave activity near the tropopause. In addition to a change in the generation and refraction of planetary waves, a modification of the gravity-wave spectrum could also alter the wave driving of the BDC during northern winter. However, such a modification is difficult to predict, since all GCMs rely at least partly on gravity-wave parameterizations, for which the degree of accuracy is still uncertain. In the present study, the processes via which the resolved wave driving of the BDC could increase in an enhanced-CO₂ climate are examined in greater detail, using the same climate simulations as used by Sigmond et al. (2004).

4.2 Climate simulations and methods

This study compares two climate simulations which have been performed by Sigmond et al. (2004), using the middle-atmosphere (MA) version of the ECHAM4 model (Manzini et al. 1997; Roeckner et al. 1996). The model has a T42 horizontal spectral resolution (about $2.8^\circ \times 2.8^\circ$), with 39 vertical levels between the surface and 0.01 hPa (about 80 km). Momentum deposition by sub-grid scale waves is parameterized for both orographic gravity waves (McFarlane 1987) and for a transient gravity-wave spectrum (Hines 1997a,b).

One simulation is a 30-yr control run (run C in Sigmond et al. (2004)), in which CO₂ concentrations were fixed at 353 ppmv, which was the atmospheric CO₂ content in 1990. In the perturbation run (run A in Sigmond et al. (2004)), CO₂ concentrations were doubled. The prescribed sea-surface temperatures were obtained from a control run and a doubled-CO₂ run with the ECHAM4 model coupled to a slab layer ocean model.

We use the zonal-mean poleward eddy heat flux $[\nu * T^*]$ as a measure of the net zonal-mean upward flux of planetary-wave activity, since $[\nu * T^*]$ is proportional to the vertical component of the EP flux for quasigeostrophic waves. We define H_{100} as the average of $[\nu * T^*]$ at 100 hPa over January-February and 40° - 80° N. This (or a similar) diagnostic has been used in several studies, e.g., Austin et al. (2003), and Haklander et al. (2007). By partitioning the response of H_{100} to the CO₂ doubling into its stationary and transient

components for different zonal wavenumbers, we examine the causes and nature of the increase in the northern midwinter wave driving in greater detail. Here, the zonal wavenumber- k component of $[\nu^*T^*]$ is defined as the zonal-mean product of the wave- k components of ν and T .

Additionally, the poleward eddy heat flux is decomposed by noting that it equals the zonal covariance between ν and T , i.e.,

$$[\nu^*T^*] = r_{\nu,T} \sigma_\nu \sigma_T, \quad (4.1)$$

where $r_{\nu,T}$ is the zonal correlation coefficient of ν and T , and σ_ν and σ_T are the zonal standard deviations of ν and T . Both σ_ν and σ_T are indicators of wave amplitude, while $r_{\nu,T}$ is a measure of how effectively waves transport the sensible heat poleward. For monochromatic waves, $r_{\nu,T}$ is directly proportional to the cosine of the zonal phase difference between the ν and T fields. CO₂ doubling could modify both the amplitude of the waves and the efficacy of the poleward eddy heat transport.

By definition, H_{100} is obtained by evaluating the l.h.s. of Equation (4.1) at 100 hPa and averaging over January-February and 40°-80°N. Obviously, exactly the same result is obtained by evaluating the r.h.s. of Equation (4.1) at 100 hPa and averaging it as a single variable over January-February and 40°-80°N. However, if the three r.h.s. terms are averaged separately, the product of those three separate averages might be different from the average of the single-variable product. For instance, the average of $r_{\nu,T}$ over January-February and 40°-80°N could be zero, while the same average of the r.h.s. as a single-variable product could be non-zero due to intraseasonal and meridional cross-correlations between $r_{\nu,T}$, σ_ν , and σ_T . Averaging the three, separate factors on the r.h.s. of Equation (4.1) over January-February and 40°-80°N at 100 hPa, and multiplying them, thus yields an approximation of H_{100} which can be compared to H_{100} itself. For both runs, the 30-year timeseries of this approximation of H_{100} follows that of H_{100} itself very closely: correlation coefficients are 0.96 and 0.89 for the control and doubled-CO₂ runs,

respectively. Henceforth, to keep the notation simple, $r_{v,T}$, σ_v , and σ_T will denote the corresponding averages over January-February and 40°-80°N at 100 hPa. Since $r_{v,T}\sigma_v\sigma_T$ provides a good estimate for H_{100} , we examine if the difference in H_{100} between the control and doubled-CO₂ runs can be understood in terms of the differences in $r_{v,T}$, σ_v , and σ_T . The aforementioned decompositions of the poleward eddy heat flux have been discussed in more detail by Haklander et al. (2007, section 2.3).

In the present paper, the uncertainties provided along with the estimates represent the 95% confidence intervals. Differences between the control run and the doubled-CO₂ run are considered statistically significant if the confidence level exceeds 95%.

4.3 Results

We first examine the effect of CO₂ doubling on H_{100} by comparing the 30-year averages of the control and doubled-CO₂ runs. The result is shown in Table 4.1, along with the same comparison for several wave components of H_{100} . The total H_{100} control-run average of 15.0 ± 0.9 K m/s agrees remarkably well with the observed 1979-2002 average of 15.1 ± 1.1 K m/s in the ERA-40 dataset (Haklander et al. 2007). In our model, doubling the CO₂ concentrations yields a significant and substantial increase in H_{100} of 1.8 ± 1.2 K m/s, or $12\% \pm 8\%$ of the control average.

In both the control and the perturbation run, the stationary waves dominate the influx of planetary wave activity into the lower stratosphere. Doubling the CO₂ concentration in the model yields a significant stationary-wave flux increase of $23\% \pm 16\%$, which determines almost entirely the total H_{100} increase. The stationary-wave flux increase occurs mainly in its stationary wave-1 component. Of the longest five stationary zonal wave components, only wavenumber 1 exhibits a noticeable change. This suggests that the total wave response to the CO₂ doubling can mainly be attributed to stationary wave 1.

When considering the transient waves, we find a significant and substantial reduction in the transient wave-1 flux. However, this reduction is neutralized by small increases in the transient wave 2-5 components. Although the change in the transient

Table 4.1: The 30-year averages for run C and run A, and differences between the A- and C-runs for H_{100} and its total, stationary and transient $k = 1-5$ components (K m/s). Also provided are the 95% confidence intervals. Components for which the differences are >95% significant have been given in bold.

Component	C-run mean	A-run mean	Diff.	Relative diff. (%)
Total	15.0 ± 0.9	16.8 ± 0.8	$+1.8 \pm 1.2$	$+12\% \pm 8\%$
Stationary	8.6 ± 1.0	10.6 ± 0.9	$+2.0 \pm 1.3$	$+23\% \pm 16\%$
Transient	6.4 ± 0.6	6.2 ± 0.5	-0.1 ± 0.8	$-2\% \pm 12\%$
Total 1	8.6 ± 1.0	9.2 ± 0.7	$+0.6 \pm 1.2$	$+7\% \pm 14\%$
Total 2	3.2 ± 0.7	3.4 ± 0.5	$+0.3 \pm 0.8$	$+8\% \pm 26\%$
Total 3	1.7 ± 0.4	2.1 ± 0.3	$+0.4 \pm 0.5$	$+24\% \pm 27\%$
Total 4	0.5 ± 0.2	0.5 ± 0.2	$+0.1 \pm 0.3$	$+12\% \pm 56\%$
Total 5	0.5 ± 0.1	0.9 ± 0.1	$+0.4 \pm 0.2$	$+86\% \pm 40\%$
Stationary 1	6.5 ± 1.0	8.2 ± 0.7	$+1.7 \pm 1.3$	$+27\% \pm 20\%$
Stationary 2	1.7 ± 0.6	1.8 ± 0.5	$+0.1 \pm 0.8$	$+5\% \pm 46\%$
Stationary 3	0.5 ± 0.3	0.6 ± 0.2	$+0.1 \pm 0.4$	$+26\% \pm 80\%$
Stationary 4	-0.2 ± 0.1	-0.2 ± 0.1	$+0.0 \pm 0.1$	$+1\% \pm 60\%$
Stationary 5	0.1 ± 0.1	0.2 ± 0.0	$+0.1 \pm 0.1$	$+49\% \pm 59\%$
Transient 1	2.2 ± 0.4	1.1 ± 0.3	-1.1 ± 0.5	$-51\% \pm 25\%$
Transient 2	1.5 ± 0.4	1.6 ± 0.3	$+0.2 \pm 0.5$	$+12\% \pm 35\%$
Transient 3	1.2 ± 0.3	1.5 ± 0.2	$+0.3 \pm 0.3$	$+23\% \pm 28\%$
Transient 4	0.7 ± 0.1	0.8 ± 0.2	$+0.1 \pm 0.2$	$+8\% \pm 30\%$
Transient 5	0.4 ± 0.1	0.7 ± 0.1	$+0.4 \pm 0.1$	$+99\% \pm 45\%$

wave 2-4 components is not significant, the statistical significance of the increase in the transient wave-5 flux is extremely high. This issue will be further assessed in the next section. Although we limit this study to the 100-hPa level, the vertical coherence in Figures 4.1 and 4.2 shows that 100 hPa can be regarded as representative for the lower stratosphere. At the adjacent model levels (70 and 150 hPa), the increases in ' H_{70} ' and ' H_{150} ' are 1.3 ± 1.5 K m/s ($8\% \pm 9\%$), and 0.6 ± 1.2 K m/s ($4\% \pm 7\%$), respectively. Significant changes in the stationary wave-1, and transient wave-1 and wave-5 fluxes are also found at 70 and 150 hPa, with the dominant change being an increase in the stationary wave-1 flux.

So far, we have only discussed 40°-80°N averages at 100 hPa, and not yet considered the pattern of the difference in $[\nu^*T^*]$ in the meridional plane. It was mentioned in the previous section, that for quasigeostrophic waves $[\nu^*T^*]$ is proportional to the vertical component of the EP flux. The meridional pattern of the EP-flux vector differences can elucidate the effect of CO₂ doubling on the propagation of planetary-wave activity. Figure 4.1 shows these difference patterns for the total, stationary and transient components of the EP flux. At midlatitudes between 400 and 10 hPa, the total upward EP flux increases significantly (light shading). A significant decrease (dark shading) is found in the troposphere north of about 25°N. In the stratosphere the total wave response (Figure 4.1a) is similar to the stationary-wave response (Figure 4.1b), whereas in the troposphere it is more similar to the transient-wave response (Figure 4.1c). In the subtropical troposphere, the doubled-CO₂ run exhibits significantly less equatorward propagation of (transient) wave activity, indicated by the poleward orientation of the EP flux difference vectors in Figures 4.1a and 4.1c. If we start in the subtropical troposphere and follow the difference vectors according to ray-tracing theory, we see that the subtropical reduction of equatorward wave propagation is likely associated with less transient upward wave propagation in the midlatitude (lower) troposphere to begin with. The latter is expected to be due to a decrease in baroclinicity, since the tropospheric pole-to-equator temperature gradient is reduced in the perturbation run (Sigmond et al. 2004, Figure 2a).

Since a significant difference between the control and perturbation runs was found for the stationary wave-1 and transient wave-1 and wave-5 components of H_{100} , we also show the meridional cross sections of the EP flux difference for those three wave components in Figure 4.2. For stationary wave-1 (Figure 4.2a), a marked increase in the upward EP flux is observed particularly at midlatitudes, although the increase is not statistically significant in the lower troposphere. Nevertheless, the contour pattern in Figure 4.2a indicates that the increase in stationary wave-1 activity flux at 100 hPa is associated with an increase in upward stationary wave-1 flux in the entire troposphere. The results in Table 4.1 suggest that the total wave response to the CO₂ doubling can mainly be attributed to stationary wave 1. This is confirmed by the strong similarity in the lower stratosphere between the total difference pattern in Figure 4.1a and the stationary

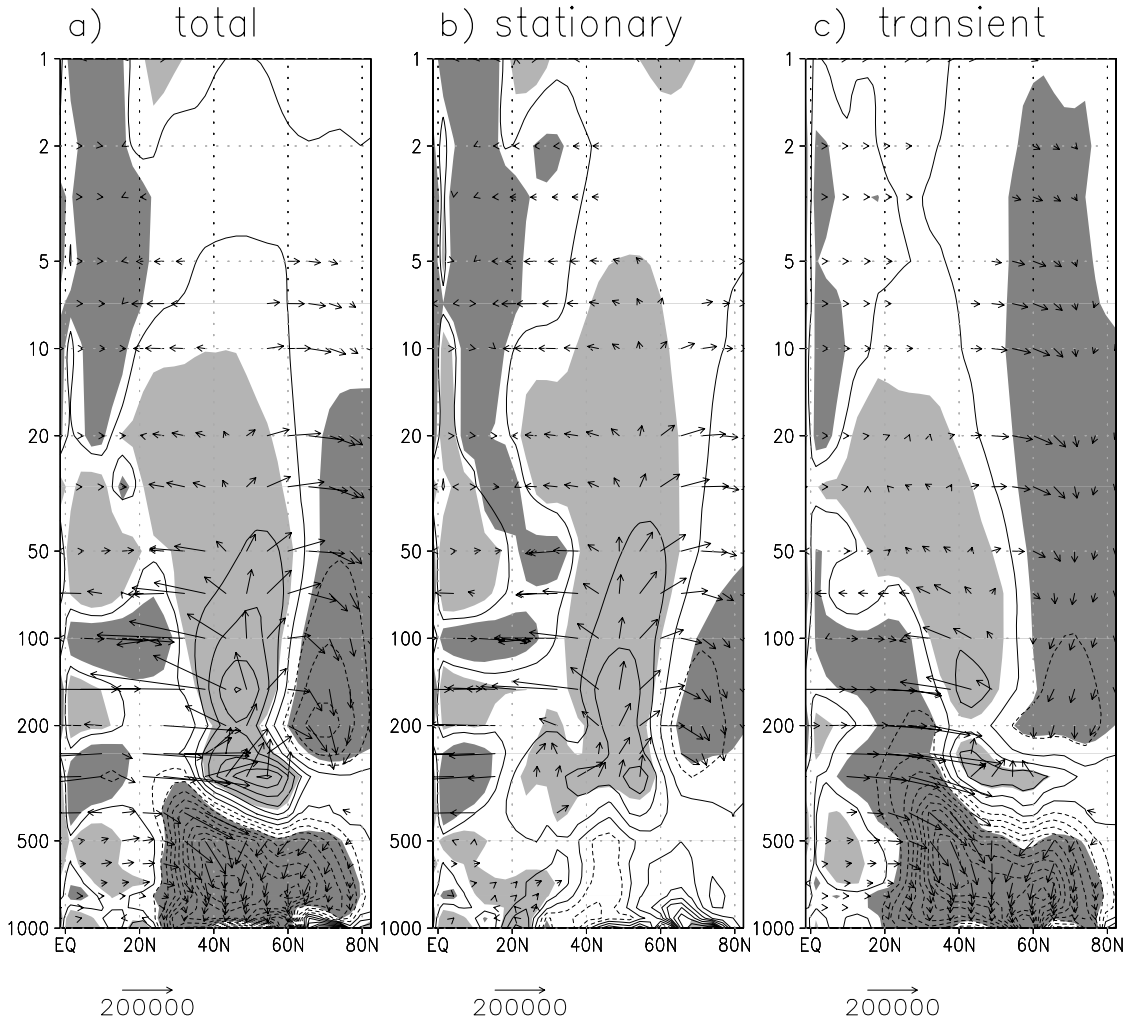


Figure 4.1: Meridional cross sections of the mean difference in EP flux vectors (doubled- CO_2 – control run) for the *a*) total, *b*) stationary, and *c*) transient waves. Difference vectors are drawn only if the difference in at least one of the two EP flux components is statistically significant at the 95% confidence level. The vectors have been scaled by multiplying with $e^{-z/H}$ (where the scale height $H = 7$ km) and the meridional components have been divided by 70 to account for the aspect ratio of the plots. Contours indicate the difference in the (unscaled) vertical EP flux. Negative contour lines are dashed, and the contour interval is $2 \times 10^4 \text{ m}^3 \text{ s}^{-2}$. Significantly (95%) positive and negative values are shaded light and dark, respectively.

wave-1 difference pattern in Figure 4.2a. Figure 4.2b shows that the substantial decrease in the transient wave-1 component of H_{100} is due to a flux decrease north of about 52°N .

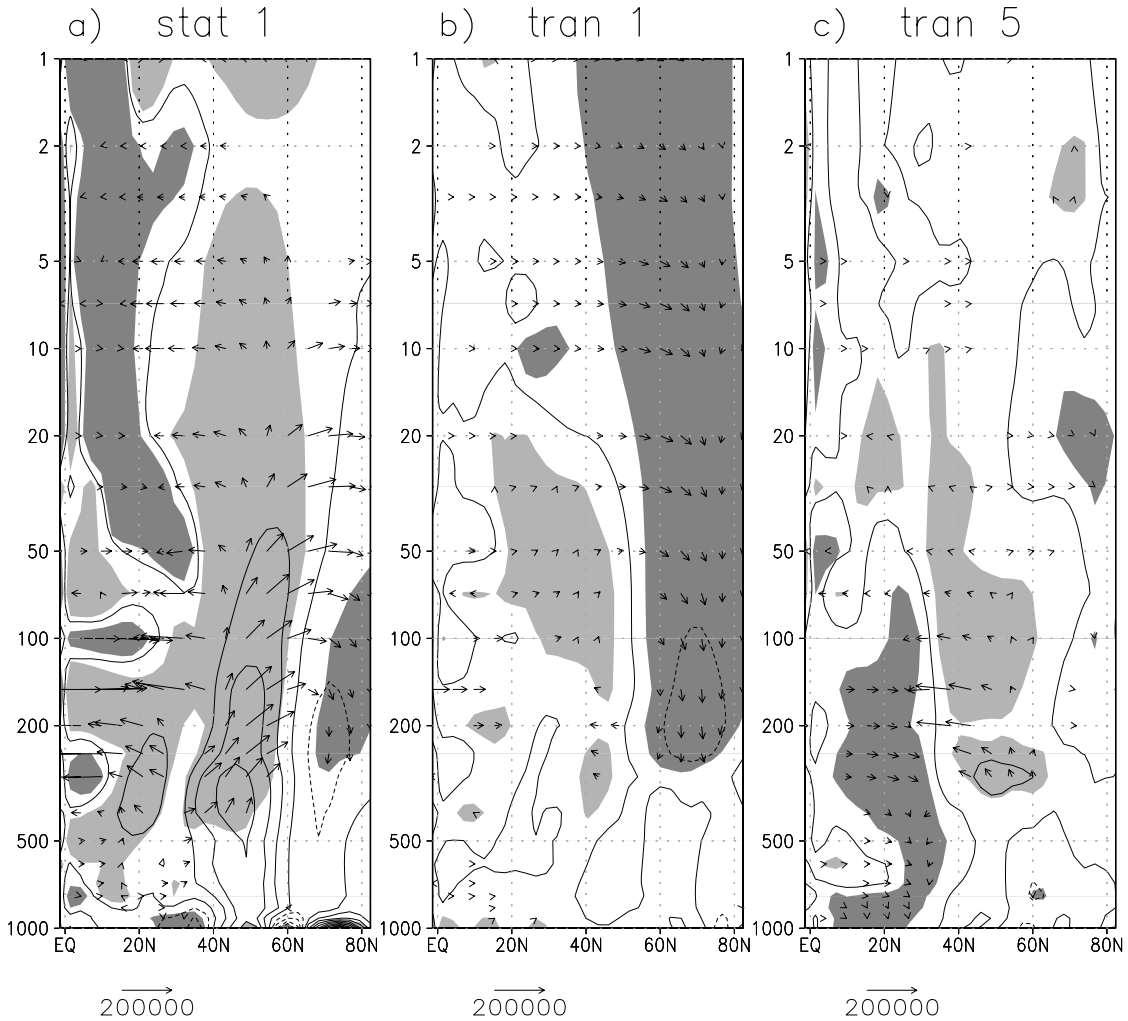


Figure 4.2: Meridional cross sections of the mean difference in EP flux vectors (doubled-CO₂ – control run) for the *a*) stationary-1, *b*) transient-1, and *c*) transient-5 wave components. Scaling, contours, and shading as in Figure 4.1.

The EP-flux difference for the transient wave-5 component at 100 hPa (Figure 4.2c) exhibits a significant increase at midlatitudes.

We next examine the effect of CO₂ doubling on the amplitude of the waves, and their correlation, as described in the previous section. Table 4.2 shows the 30-year averages and differences for H_{100} , its approximate value $r_{v,T}\sigma_v\sigma_T$, and $r_{v,T}$, σ_v , and σ_T . The increase in $r_{v,T}\sigma_v\sigma_T$ in the doubled-CO₂ climate is statistically significant and quantitatively comparable to the increase in H_{100} . The changes in $r_{v,T}$ are very small and not significant. However, the zonal standard deviations of both v and T do show a

Table 4.2: The 30-year averages for the control and doubled-CO₂ runs, and differences between the two runs in H_{100} and $r_{v,T}\sigma_v\sigma_T$ (K m/s), and the separate factors $r_{v,T}$, σ_v (m/s), and σ_T (K). Also provided are the 95% confidence intervals. Components for which the differences are 95% significant have been printed in bold.

Component	Control	2×CO ₂	Diff.	Relative diff. (%)
H_{100}	15.0 ± 0.9	16.8 ± 0.8	+1.8 ± 1.2	+12% ± 8%
$r_{v,T}\sigma_v\sigma_T$	14.1 ± 0.9	16.4 ± 0.8	+2.3 ± 1.2	+16% ± 8%
$r_{v,T}$	0.213 ± 0.007	0.216 ± 0.013	+0.002 ± 0.015	+1% ± 7%
σ_v	10.1 ± 0.2	10.5 ± 0.3	+0.4 ± 0.4	+4% ± 3%
σ_T	6.5 ± 0.2	7.3 ± 0.2	+0.8 ± 0.3	+12% ± 5%

significant increase. Whereas σ_v exhibits only a marginal increase, the increase in σ_T is found to be the dominant cause of the increased wave driving. Not only is the change in σ_T significant, the relative change is substantial (+12% ± 5%) and comparable to the change in H_{100} (+12% ± 8%). A significant increase in σ_T is also found at the model

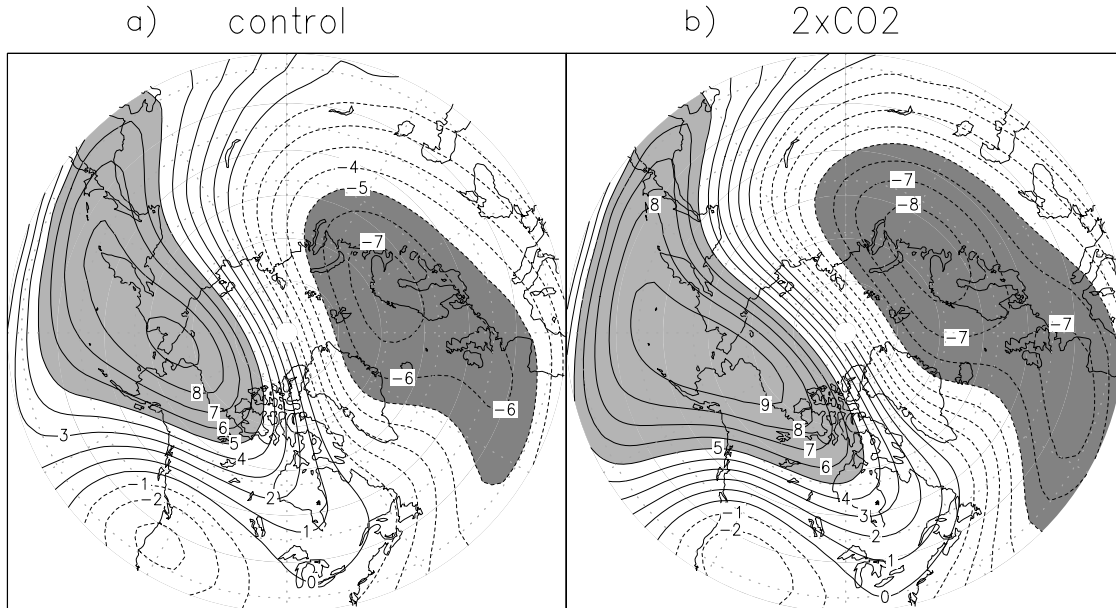


Figure 4.3: January-February mean eddy temperature field T^* at 100 hPa, for *a*) the control run, and *b*) the doubled-CO₂ run. Light and dark shading indicate eddy temperatures above +5K and below -5K, respectively. The contour interval is 1K.

levels adjacent to 100 hPa (70 and 150 hPa), and the percent increase in σ_T is comparable with the percent increase in the total heat flux at both levels (not shown). In Figure 4.3, the January-February mean total eddy temperature field at 100 hPa is shown for the control and the perturbation runs. The stationary wave-1 signature is well visible for both experiments, and the figure clearly demonstrates the increase in longitudinal temperature variability in the doubled-CO₂ run. The increase in σ_T may be due to an increase in the meridional temperature gradient between 40°-80°N at 100 hPa, as meridional air displacements will produce larger zonal temperature asymmetries if the zonal-mean meridional temperature gradient increases. Indeed, the 30-year average January-February temperature difference between 40°N and 80°N at 100 hPa increases by about 10% in the perturbation run (not shown). Below 400 hPa, the temperature difference between 40°N and 80°N decreases in the doubled-CO₂ run, with the largest reduction in the lower troposphere. This result agrees with the significant reduction in midlatitude upward EP flux at those levels that was discussed above.

4.4 Conclusions

In this paper, the effect of CO₂ doubling on the northern-winter upward wave activity flux at midlatitudes has been analyzed, using the MA-ECHAM4 climate model. The upward wave flux is quantified by H_{100} , defined as the average of $[v^*T^*]$ at 100 hPa over January-February and 40°-80°N. Doubling the CO₂ concentration leads to a substantial and significant increase in H_{100} of 1.8 ± 1.2 K m/s, or $12\% \pm 8\%$. This is, at least qualitatively, in agreement with the studies by, e.g., Butchart and Scaife (2001), Rind et al. (1998, 2002), and Butchart et al. (2006). Table 4.1 and the strong lower-stratospheric similarity between Figures 4.1a and 4.2a indicate that stationary-wave 1 likely accounts for almost all of the total increase in H_{100} . This, in combination with the results in Figure 4.2a, suggests that at least part of the increase is due to more stationary wave-1 generation at midlatitudes in the (lower) troposphere. The results indicate that doubling the CO₂ yields significant changes in transient wave-1 and transient wave-5 as well. The latter change is in agreement with the result of Eichelberger and Hartmann

(2005), but their model setup (no topography) was quite different from that in the present study. Transient wave-5 may not seem very relevant, since it only amounts to $2.4 \pm 0.5\%$ and $4.2 \pm 0.7\%$ percent of H_{100} in the control and perturbation runs, respectively. Nevertheless, the transient wave-5 increase amounts to $19 \pm 15\%$ of the total H_{100} increase.

Using an alternative decomposition of the poleward eddy heat flux, we found that the increased wave driving can be attributed mainly to a larger longitudinal temperature variability, that is mainly due to the increased meridional temperature gradient at 100 hPa in the doubled-CO₂ climate simulation. With only one climate model at our disposal, we were not able to test the robustness of our results. However, both the increase in the northern-winter wave driving of the BDC and the increase in the 100-hPa meridional temperature gradient are robust features in enhanced-CO₂ climate simulations. We would welcome studies in which our analysis method is applied to data from other enhanced-CO₂ simulations.

Acknowledgements

The authors gratefully acknowledge the constructive suggestions that were made by two anonymous referees.

5

Discussion and Outlook

In this concluding chapter the main results of the study presented in this thesis will be summarized. In addition, an outlook is given with suggestions for future research.

5.1 Discussion

In this thesis, the following questions have been addressed:

1. How do observations compare to a quasigeostrophic model for the frequency-dependent response of the zonal-mean flow to extratropical wave forcing?
2. To what extent is the interannual variability of the total poleward eddy heat flux at 100 hPa determined by the flux at lower levels?
3. To which type of waves can most of the interannual variability of the lower-stratospheric wave forcing be attributed?
4. Is the interannual variability of the wave driving primarily controlled by the waves' amplitude or by the structure of the waves which determines the efficiency of the poleward eddy heat transport?
5. What causes the strengthening of the northern-winter wave driving of the BDC in an enhanced-CO₂ climate simulation?

The aim of this thesis has been to answer these questions, at least partly. These (partial) answers have been summarized below.

1. How do observations compare to a quasigeostrophic model for the frequency-dependent response of the zonal-mean flow to extratropical wave forcing?

This question has been addressed in Chapter 2. Operational 4D-Var ECMWF analysis data on a $1^\circ \times 1^\circ$ horizontal resolution and 35 levels between 1000 and 0.1 hPa were used to analyze the three main balancing terms in the TEM version of the zonal-mean zonal momentum equation. The data were applied to a simplified model for the frequency-dependent response of the zonal-mean zonal wind to the divergence of the EP flux. According to this quasigeostrophic model, the ratio between the zonal-mean zonal wind amplitude and the forcing amplitude can be predicted, once the frequency, the thermal damping time, and the aspect ratio of the meridional to the vertical length scale of the wave-driven meridional circulation are known. For six November-April seasons, the observed wave forcing and zonal-mean zonal wind response at 60°N were regressed onto the theoretical response function, yielding estimates for both the thermal damping time and the aspect ratio. The thermal-damping time estimates in the lower mesosphere and the stratosphere lay within the range of existing radiative damping time estimates. The estimates for the troposphere were found to be significantly smaller than the tropospheric radiative damping timescales in the literature. However, in the troposphere, baroclinic and thermally dissipative processes other than radiative damping are also important, which likely explains why our results lie on the very short end of the broad range of tropospheric radiative damping times found in the literature.

2. To what extent is the interannual variability of the total poleward eddy heat flux at 100 hPa determined by the flux at lower levels?

This question has been addressed in Chapter 3. Hereto, 24 years of ERA-40 reanalysis data have been analyzed. The correlation between year-to-year variations in the total eddy heat flux in January-February at 100 hPa and the flux at lower levels was found to be non-significant below 200 hPa. However, the individual zonal wave-1 and wave-2 contributions to the eddy heat flux at 100 hPa were found to be significantly coupled with the entire depth of the troposphere, mainly due to their stationary components. The

stationary wave-1 contribution to the heat flux was found to depend significantly on the latitude of the stationary wave-1 source in the troposphere. For stationary wave-1, the results suggest that tropospheric wave activity near 30°N is significantly less able to enter the mid-latitude waveguide than the wave activity near 50°N.

3. To which type of waves can most of the interannual variability of the lower-stratospheric wave forcing be attributed?

This question has also been addressed in Chapter 3, using the same ERA-40 reanalysis data. About 85% of the interannual variability of the heat flux at 100 hPa could be attributed to the ultralong waves, with zonal wavenumbers 1 and 2. Although these ultralong waves are known to account for most of the mean heat flux, it is no trivial result that the interannual variability is also dominated by zonal wavenumbers 1 and 2. Stationary wave activity was found to dominate the interannual variability, rather than the transient waves.

4. Is the interannual variability of the wave driving primarily controlled by the waves' amplitude or by the structure of the waves which determines the efficiency of the poleward eddy heat transport?

Also in Chapter 3, this question has been addressed by describing the heat flux as the product of wave amplitude and the heat-flux 'efficiency'. In a mathematical sense, the heat flux anomalies were separated into three parts: one part due to anomalies in the zonal correlation coefficient between the eddy temperature and eddy meridional wind ('the efficiency'), another part due to anomalies in the zonal eddy temperature amplitude, and a third part due to anomalies in the zonal eddy meridional wind amplitude. It was found that a significant part of the year-to-year variability in the wave driving as described by the heat flux is not determined by variability in the amplitude of the waves but by variability in the efficiency of the poleward heat transport. We also note that the variability in the temperature amplitude affects the heat flux more strongly than the variability in the meridional wind amplitude.

5. What causes the strengthening of the northern-winter wave driving of the BDC in an enhanced-CO₂ climate simulation?

This question has been addressed in Chapter 4. Using the middle-atmosphere General Circulation Model ECHAM4, the results of two 30-year climate runs were compared. In the control run, CO₂ concentrations were fixed at the 1990 level, in the perturbation run CO₂ concentrations were fixed at the doubled value. Recent studies have shown that CO₂ doubling yields an increase in the wave driving of the BDC, a feature that is also observed in our simulations. At 100 hPa, the midwinter heat flux was found to increase by 12% in the doubled-CO₂ climate. Significant changes in the stationary wave-1, transient wave-1 and wave-5 contributions to the heat flux at 100 hPa were found. Despite the increased upward wave flux at 100 hPa, a significant decrease was found in the troposphere, which was associated mostly with the transient waves. The increase in upward wave propagation in the lower stratosphere could be linked to the stationary waves, wave-1 in particular. This increase could be due to changes in the refraction and/or absorption of stationary wave-1 activity from the troposphere. However, interestingly, the stationary wave-1 component of the upward wave flux also increased significantly in the troposphere, whereas the total flux exhibited a sharp decrease. This suggests that the stationary wave-1 increase at 100 hPa can be associated, at least in part, with more generation of stationary wave-1 at midlatitudes in the (lower) troposphere. Finally, it was found that the increased wave driving can be attributed mainly to a larger longitudinal temperature variability. The latter increase may be understood in terms of the increase in the 100-hPa meridional temperature gradient, which is a robust and well-understood feature in doubled-CO₂ climate simulations.

5.2 Outlook

Several questions have arisen during the present study and require further research.

The quasigeostrophic model, used to obtain the results presented in Chapter 2, is a major simplification of the real, non-local response of the zonal-mean flow to a given wave forcing. Even if there is no local forcing, zonal-mean zonal wind accelerations will still occur (see Andrews et al. 1987, Equation 3.5.7). Therefore, a more precise extension of this work would be to take account of the non-local dependence of the zonal-mean zonal wind acceleration on the forcing. Also, the analysis in Chapter 2 was confined to 60°N, where the wave driving reaches a maximum. However, it would also be interesting to include other extratropical latitudes with weaker forcing, where a quasigeostrophic description of the flow should also be a good approximation. This would give a better idea of the uncertainties in the estimated values of the thermal damping times and the aspect ratio of the response.

The interannual variability of the resolved wave driving of the BDC has been studied in Chapter 3. However, it is important to realize that a significant part of the wave driving is not resolved, but is parameterized. In the Southern Hemisphere, where less planetary-wave activity is generated in the troposphere than in the NH, most of the downwelling in the Antarctic winter stratosphere is believed to be due to small-scale internal gravity waves (Shepherd 2000). Although planetary waves are dominant on average in the NH winter stratosphere, little is known about the interannual variability of the non-resolved wave forcing. Therefore, improving our observational knowledge of gravity-wave sources is still a major challenge. Also, the effect of enhanced CO₂ concentrations on gravity waves is poorly known.

The results shown in Chapter 4 are not necessarily robust, and we would welcome studies in which our analysis method is applied to data from other enhanced-CO₂ simulations.

References

Andrews, D. G., Holton, J.R., and Leovy, C.B.: Middle atmosphere dynamics, Academic Press, 489 pp., 1987.

Austin, J., D. Shindell, S.R. Beagley, C. Brühl, M. Dameris, E. Manzini, T. Nagashima, P. Newman, S. Pawson, G. Pitari, E. Rozanov, C. Schnadt, and T.G. Shepherd: Uncertainties and assessments of chemistry-climate models of the stratosphere, *Atmos. Chem. Phys.*, 3, 1–27, 2003.

Barry, L., G. C. Craig, and J. Thuburn: A GCM investigation into the nature of baroclinic adjustment, *J. Atmos. Sci.*, 57, 1141–1155, 2000.

Burde, G. I.: Semigeostrophic Eady wave frontogenesis in the presence of Newtonian cooling, *J. Atmos. Sci.*, 56, 3774–3788, 1999.

Butchart, N., and A. A. Scaife: Removal of CFCs through increased mass exchange between the stratosphere and troposphere in a changing climate, *Nature*, 410, 799–801, 2001.

Butchart, N., A. A. Scaife, M. Bourqui, J. de Grandpre, S. H. E. Hare, J. Kettleborough, U. Langematz, E. Manzini, F. Sassi, K. Shibata, D. Shindell, and M. Sigmond: Simulations of anthropogenic change in the strength of the Brewer-Dobson circulation, *Climate Dynamics*, 27, 727–741, doi: 10.1007/s00382-006-0162-4, 2006.

Charney, J. G., and Drazin, P. G.: Propagation of planetary-scale disturbances from the lower to the upper atmosphere, *J. Atmos. Sci.*, 18, 83–109, 1961.

Christiansen, B.: Stratospheric vacillations in a General Circulation Model, *J. Atmos. Sci.*, 56, 1858–1872, 1999.

Christiansen, B.: Downward propagation of zonal mean zonal wind anomalies from the stratosphere to the troposphere, Model and reanalysis, *J. Geophys. Res.*, 106(D21), 27307–27322, 2001.

Eichelberger, S. J. Hartmann, D. L.: Changes in the strength of the Brewer-Dobson circulation in a simple AGCM, *Geophys. Res. Lett.*, 32, L15807, doi: 10.1029/2005GL022924, 2005.

Eyring, V., N. R. P. Harris, M. Rex, T. G. Shepherd, D. W. Fahey, G. T. Amanatidis, J. Austin, M. P. Chipperfield, M. Dameris, P. M. De F. Forster, A. Gettelman, H. F. Graf, T. Nagashima, P. A. Newman, S. Pawson, M. J. Prather, J. A. Pyle, R. J. Salawitch, B. D. Santer, and D. W. Waugh: A strategy for process-oriented validation of coupled chemistry-climate models, *Bull. Am. Meteorol. Soc.*, 86, 1117–1133, 2005.

Fusco, A. C., and M. L. Salby: Interannual variations of total ozone and their relationship to variations of planetary wave activity, *J. Climate*, 12, 1619–1629, 1999.

Garcia, R. R.: On the mean meridional circulation in the middle atmosphere, *J. Atmos. Sci.*, 44, 3599–3609, 1987.

Haklander, A. J., and A. van Delden: Thunderstorm predictors and their forecast skill for the Netherlands. *Atmos. Res.*, 67–68, 273–299, 2003.

Haklander, A. J., P. C. Siegmund, and H. M. Kelder: Analysis of the frequency-dependent response to wave forcing in the extratropics, *Atmos. Chem. Phys.*, 6, 4477–4481, 2006.

Haklander, A. J., P. C. Siegmund, and H. M. Kelder: Interannual variability of the stratospheric wave driving during northern winter, *Atmos. Chem. Phys.*, 7, 2575–2584, 2007.

Haklander, A. J., P. C. Siegmund, M. Sigmond, and H. M. Kelder: How does the northern-winter wave driving of the Brewer-Dobson circulation increase in an enhanced-CO₂ climate simulation?, *Geophys. Res. Lett.*, 35, L07702, doi:10.1029/2007GL033054, 2008.

Hartmann, D. J., J. M. Wallace, V. Limpasuvan, D. W. J. Thompson, and J. R. Holton: Can ozone depletion and global warming interact to produce rapid climate change?, *PNAS*, 97, 1412–1417, 2000.

Haynes, P. H., C. J. Marks, M. E. McIntyre, T. G. Shepherd and K. P. Shine: On the "downward control" of extratropical diabatic circulations by eddy-induced mean zonal forces, *J. Atmos. Sci.*, 48, 651–678, 1991.

Haynes, P.H.: Stratospheric dynamics, *Ann. Rev. Fluid Mech.*, 37, 263–293, 2005.

Held, I. M., and Suarez, M. J.: A proposal for the intercomparison of the dynamical cores of atmospheric general circulation models, *Bull. Am. Meteorol. Soc.*, 73, 1825–1830, 1994.

Hines, C. O.: Doppler-spread parameterization of gravity-wave momentum deposition in the middle atmosphere. Part 1: Basic formulation. *J. Atmos. Solar-Terr. Phys.*, 59, 371–386, 1997a.

Hines, C. O.: Doppler-spread parameterization of gravity-wave momentum deposition in the middle atmosphere. Part 2: Broad and quasi monochromatic spectra, and implementation. *J. Atmos. Solar-Terr. Phys.*, 59, 387–400, 1997b.

Holton, J. R., Haynes, P. H., McIntyre, M. E., Douglass, A. R., Rood, R. B., and Pfister, L.: Stratosphere-troposphere exchange, *Rev. Geophys.*, 33, 403–439, 1995.

References

Hu, Y., and K. K. Tung: Possible ozone-induced long-term changes in planetary wave activity in late winter, *J. Climate*, 16, 3027–3038, 2003.

Karoly, D., and B. J. Hoskins: Three-dimensional propagation of planetary waves, *J. Meteor. Soc. Japan*, 60, 109–123, 1982.

Limpasuvan, V., D. Thompson, W. J., and Hartmann, D. L.: The life cycle of the Northern Hemisphere sudden stratospheric warmings, *J. Climate*, 17, 2584–2596, 2004.

Manzini, E., N. A. McFarlane, and C. McLandress: Impact of the Doppler spread parameterization on the simulation of the middle atmosphere circulation using the MA/ECHAM4 general circulation model, *J. Geophys. Res.*, 102(D22), 25751–25762, 1997.

McIntyre M. E. and T. N. Palmer: Breaking planetary waves in the stratosphere, *Nature*, 305, 593–600, 1983.

McIntyre M. E. and T. N. Palmer: The "surf zone" in the stratosphere. *J. Atmos. Terr. Phys.*, 46, 825–849, 1984.

McFarlane, N.A.: The effect of orographically excited gravity-wave drag on the general circulation of the lower stratosphere and troposphere. *J. Atmos. Sci.*, 44, 1775–1800, 1987.

Newman, P. A., and Rosenfield, J. E.: Stratospheric thermal damping times, *Geophys. Res. Lett.*, 24, 433–436, 1997.

Newman, P. A., and E. R. Nash: Quantifying wave driving of the stratosphere, *J. Geophys. Res.*, 105, 12485–12497, 2000.

- Newman, P. A., E. R. Nash, and J. E. Rosenfield: What controls the temperature of the Arctic stratosphere during the spring?, *J. Geophys. Res.*, 106(D17), 19999–20010, 2001.
- Peixoto, J. P., and Oort, A. H.: *Physics of climate*, American Institute of Physics, New York, 520pp, 1992.
- Polvani, L. M., and D. W. Waugh: Upward wave activity flux as precursor to extreme stratospheric events and subsequent anomalous surface weather regimes, *J. Climate*, 17, 3548–3554, 2004.
- Prinn, R. G.: On the radiative damping of atmospheric waves, *J. Atmos. Sci.*, 34, 1386–1401, 1977.
- Randel, W. J., Garcia, R. R., and Wu, F.: Time-dependent upwelling in the tropical lower stratosphere estimated from the zonal-mean momentum budget, *J. Atmos. Sci.*, 59, 2141–2152, 2002.
- Randel, W.J., F. Wu and R. Stolarski: Changes in column ozone correlated with the stratospheric EP flux, *J. Meteorol. Soc. Japan*, 80, 849–862, 2002.
- Rind, D., D. Shindell, P. Lonergan, and N. K. Balachandran: Climate change and the middle atmosphere. Part III: The doubled CO₂ climate revisited, *J. Climate*, 11, 876–894, doi:10.1175/1520-0442, 1998.
- Rind, D., P. Lonergan, N. K. Balachandran, and D. Shindell: 2×CO₂ and solar variability influences on the troposphere through wave-mean flow interaction, *J. Meteorol. Soc. Japan*, 80, 863–876, 2002.
- Roeckner, E., K. Arpe, L. Bengtsson, M. Christoph, M. Claussen, L. Dümenil, M. Esch, M. Giorgetta, U. Schlese, and U. Schulzweida: *The atmospheric general circulation model ECHAM-4: model description and simulation of present-day climate*, Max-Planck Institute for Meteorology, Report No.218, Hamburg, Germany, 90 pp, 1996.

References

Rosenlof, K. H.: Seasonal cycle of the residual mean meridional circulation in the stratosphere, *J. Geophys. Res.*, 100(D3), 5173–5191, 1995.

Scheele, M.P., Siegmund, P. C., and Van Velthoven, P. F. J.: Stratospheric age of air computed with trajectories based on various 3D-Var and 4D-Var data sets, *Atmos. Chem. Phys.*, 5, 1–7, 2005.

Shepherd, T. G., and Shaw, T. A.: The angular momentum constraint on climate sensitivity and downward influence in the middle atmosphere, *J. Atmos. Sci.*, 61, 2899–2908, 2004.

Shepherd, T. G.: The middle atmosphere, *J. Atmos. Sol.-Terr. Phys.*, 62, 1587–1601, 2000.

Shindell, D. T., R. L. Miller, G. A. Schmidt, and L. Pandolfo: Simulation of recent northern winter climate trends by greenhouse-gas forcing, *Nature*, 399, 452–455, doi:10.1038/20905, 1999.

Siegmund P. C.: The generation of available potential energy: a comparison of results from a general circulation model with observations, *Clim. Dyn.*, 11, 129–140, 1995.

Sigmond, M., P. C. Siegmund, E. Manzini, and H. Kelder: A simulation of the separate climate effects of middle atmospheric and tropospheric CO₂ doubling, *J. Climate*, 17, 2352–2367, 2004.

Simmons, A. J., and J. K. Gibson: The ERA-40 project plan, ERA-40 Proj. Rep. Ser. 1, European Centre for Medium-Range Weather Forecasts, Reading, U. K., 63 pp., 2000.

Uppala, S. M., P. W. Kållberg, A. J. Simmons, U. Andrae, V. Da Costa Bechtold, M. Fiorino, J. K. Gibson, J. Haseler, A. Hernandez, G. A. Kelly, X. Li, K. Onogi, S. Saarinen, N. Sokka, R. P. Allan, E. Andersson, K. Arpe, M. A. Balmaseda, A. C. M.

Beljaars, L. Van De Berg, J. Bidlot, N. Bormann, S. Caires, F. Chevallier, A. Dethof, M. Dragosavac, M. Fisher, M. Fuentes, S. Hagemann, E. Hólm, B. J. Hoskins, L. Isaksen, P. A. E. M. Janssen, R. Jenne, A. P. McNally, J. -F. Mahfouf, J. -J Morcrette, N. A. Rayner, R. W. Saunders, P. Simon, A. Sterl, K. E. Trenberth, A. Untch, D. Vasiljevic, P. Viterbo, and J. Woollen: The ERA-40 re-analysis, *Quart. J. R. Meteorol. Soc.*, 131, 2961–3012, DOI: 10.1256/qj.04.176, 2005.

Wu, Z., Battisti, D. S., and Sarachik, E. S.: Rayleigh friction, Newtonian cooling, and the linear response to steady tropical heating, *J. Atmos. Sci.*, 57, 1937–1957, 2000.

Nawoord

Viereneenhalf jaar geleden is het alweer dat ik aan mijn promotieonderzoek op het KNMI begon. In de vacaturebeschrijving werd het onderwerp samengevat als “Effect of stratospheric ozone depletion on tropospheric climate”. Zoals vaker gebeurt met promovendi ben ik, of liever, zijn we, enigszins van dit onderwerp afgeweken. Het was een leerzame en boeiende tijd, waarin ik tijdens dienstreizen ook wat meer van de wereld heb mogen gezien. De Canadese Rocky Mountains, Toronto en de naburige Niagara watervallen, Wenen, het vulkanische Griekse eiland Santorini, ik ben er allemaal dankzij de TU/e en het KNMI geweest. Deze jaren zullen mij echter ook, en vooral, bijblijven als de tijd waarin we ons dochtertje Rhodé moesten verliezen. Om met zo’n verlies te leren leven en om daarna ‘gewoon’ weer door te gaan met je onderzoek is veel tijd en begrip nodig. Ik ben de mensen om mij heen, op de werkvloer en in onze vrienden- en familiekring, erg dankbaar dat ze mij de ruimte hebben gegeven om weer een soort balans te vinden. Gelukkig heb ik met diezelfde mensen ook de blijdschap kunnen delen over het feit dat onze zoon Raoul — op wie ik trotser ben dan een pauw — afgelopen mei gezond en wel is geboren. Het onderzoekswerk zelf heb ik interessant gevonden, maar niet zelden ook frustrerend of niet zo maatschappelijk relevant. Ik heb er zelfs even over gedacht om Prediker 2:11 in plaats van Prediker 1:6 als begincitaat op te nemen. De link met de samenleving heb ik inmiddels in de werkkamer gevonden, als operationeel meteoroloog. Het lijkt me zeker niet ondenkbaar dat ik uiteindelijk wel weer in het onderzoek beland, maar dan zal dat wat directer op het weer van toepassing zijn.

Uiteraard wil ik een aantal mensen van harte persoonlijk bedanken. Allereerst Maria, de liefde van mijn leven. Je liefde, je geduld, je zorgzaamheid, je aanmoedigen, je relativiseringsvermogen; ik kan je niet vertellen hoeveel energie en levensvreugde je mij iedere dag weer geeft. Met jou voel ik mij gezegend en overleef ik de zwaarste storm.

Ook wil ik mijn geliefde ouders ontzettend bedanken. Jullie hebben mij altijd gestimuleerd om van mijn weerhobby mijn werk te maken. Een bezoek aan weerman Jan Pelleboer in Paterswolde, een ontsierende weerhut middenin jullie gazon — hij moest zo

vrij mogelijk staan natuurlijk — een windmeter op het dak, alwéér zappen naar het weerbericht; ik kan mij niet herinneren dat zulke dingen ooit een probleem waren.

Hoewel dit proefschrift in mindere mate aan hen te danken is en ik dit nawoord enigszins wil beperken, wil ik mijn VIF's (Very Important Friends) bedanken voor hun vriendschap en voor de nodige oppervlakkigheid en diepgang. De bijbelstudies, maatschappelijke discussies, maar ook de potjes Weerwolven en de weekendjes naar Sinderen (of misschien volgende keer een ander gat) houden we erin! Daarnaast wil ik Peter en Jessica, en mijn andere vrienden, bedanken voor hun vriendschap en hun interesse in wat ik beleef en doe.

Dan kom ik bij het werk, want daar gaat dit boekje uiteindelijk om. Veel dank ben ik verschuldigd aan mijn begeleider Peter Siegmund. In mijn ogen ben je een uitstekende en zeer sympathieke begeleider, bij wie de deur voortdurend openstaat. Ik sluit me dus geheel bij je vorige promovendus, Michael Sigmond, aan! Je goede ideeën om schijnbaar doodlopende wegen om te buigen hebben, naast je enthousiasme, een sterk motiverende werking op mij gehad. Hennie Kelder, mijn eerste promotor, van harte bedankt voor het bieden van deze leerzame baan, voor de interessante discussies en je altijd goede humeur. Ook GertJan van Heijst, mijn tweede promotor, wil ik bedanken voor de getoonde interesse en de nuttige commentaren. Peter van Velthoven, ook jou wil ik bedanken voor de boeiende discussies. Hoewel ik op onze afdeling toch een wat dynamische eend in de chemische bijt was, heb ik me o.a. door mensen als jij geen vreemde eend gevoeld.

Tijdens de jaren dat ik bij KS-AS, en later KS-CK, werkte, heb ik veel (vooral jonge) mensen zien komen en gaan. En soms weer terugkomen. Mijn collega's wil ik bedanken voor de lunch- en vooral eerst ook de koffiepauzes, die een gezellige onderbreking van de werkdag vormden. De secretaresses noem ik nog even apart; Marion, Melinda, Miranda: ik heb jullie opgewektheid maar vooral ook de persoonlijke gesprekken bijzonder gewaardeerd. Ook mijn kamergenoten bedankt: Wim Hovius (je was een ontzettend fijn mens), Peter Siegmund, Eric van der Swaluw en Margrietha Bor. Ik heb genoten van de gezellige en ontspannende momenten met jullie, tussen de bedrijven door. Waarom ik met Eric en later met Margrietha een zeer gewilde 5-sterrenkamer (incl. balkon) mocht delen is mij nog altijd een raadsel, maar: bedankt KNMI. Tot slot: God zij dank voor al het bovenstaande!

Curriculum Vitae

Alwin Johannes Haklander is geboren op woensdagmiddag 18 april 1979 in Oldebroek. Als kleuter raakte hij al gefascineerd door het weer. Aan het Lambert Franckens College te Elburg behaalde hij in 1996 zijn VWO-diploma. Gedreven door zijn passie voor de meteorologie, begon hij aan de Universiteit Utrecht met de studie Meteorologie en Fysische Oceanografie. Met name de dynamische meteorologie had zijn interesse. Zijn afstudeeronderzoek betref de bruikbaarheid van verschillende onweersindices boven Nederlands grondgebied (Haklander en Van Delden 2003). Op 27 januari 2003 sloot hij zijn universitaire studie met succes af. Na ruim een half jaar uitzendwerk begon hij op 15 december 2003 op het KNMI aan zijn promotieonderzoek aan de Technische Universiteit Eindhoven, waaruit dit proefschrift is voortgekomen. Sinds 14 april 2008 is hij als operationeel meteoroloog werkzaam in de weerkamer van het KNMI.